University of Patras

Panagiotis A. Vitsas

Numerical Investigation of Air Vehicle Noise Propagation Effects

Department of Mechanical Engineering and Aeronautics

PhD Thesis

University of Patras

Department of Mechanical Engineering and Aeronautics

PhD Thesis

2012

Panagiotis A. Vitsas

Numerical Investigation of Air Vehicle Noise Propagation Effects

Supervisor: Dr. Penelope Menounou

Academic Year 2011 to 2012

This thesis is submitted in partial fulfilment of the requirements for the degree of Doctor of Philosophy

ABSTRACT

The growth that aviation has seen in the last decades has drawn the attention on the environmental impact of aircraft. An important part of this environmental impact is the noise emitted by air vehicles, which is considered rather significant for community annoyance. The generation and propagation of air vehicle noise are two different areas of interest, which require accurate prediction in order to control the emitted noise levels.

The present thesis employs numerical methods in order to investigate various air vehicle noise propagation effects. It is divided in two parts: the far field and the near field study. Each of these studies is concentrated on the sound propagation mechanisms that are dominant for each case and uses a numerical method that is best suited for it in terms of mechanisms incorporated and cost effectiveness.

The far-field study of this thesis focuses on the nonlinear propagation of helicopter rotor noise using the Burgers equation, a well known one direction propagation method. The Burgers equation incorporates geometrical spreading, atmospheric absorption and nonlinear distortion effects. Towards this study, the HELISHAPE descent case experimental database is used. Blade Vortex Interaction (BVI) noise, the dominant noise contributor during descent, is mainly examined. It is shown that advancing side BVI noise is affected by nonlinear distortion, while retreating side BVI noise is not. For some frequency bands the difference between linear and nonlinear calculations can be as high as 7 dB. Based on signal characteristics at source, two quantities are derived. The first quantity (termed polarity) is based on the pressure gradient of the source signal and can be used to determine whether a BVI signal will evolve as an advancing or a retreating side signal. The second quantity (termed weighted rise time) is a measure of the impulsiveness of the BVI signal and can be used to determine at which frequency nonlinear effects start to appear. Finally, polarity and weighted rise time are shown to be applicable in cases of BVI noise generated from different blade tips, as well as, in cases of non-BVI noise.

However, employment of the Burgers equation can be time consuming to be included in routine calculations. It also requires knowledge of the initial pressure time signal. The power spectrum alone, which is usually known, is not sufficient. In order to

overcome these difficulties, three prediction methods are presented that are based on the Burgers equation. These are: i) a numerically generated database, ii) correlation equations and iii) the phase assignment method.

Near field propagation of air vehicle noise requires different treatment than far field. The effects which are mainly affecting the propagation are geometrical spreading, convection and refraction effects due to the flow field, as well as reflections and diffraction on the air vehicle surfaces. Towards these objectives, a new low-order flow/acoustics interaction method for the prediction of sound propagation and diffraction in unsteady compressible flow using adaptive 3-D hybrid grids is investigated. The total field is decomposed into the flow field described by the Euler equations, and the acoustics field described by the Nonlinear Perturbation equations. The method is shown capable of predicting monopole sound propagation, while employment of acoustics-guided adapted grid refinement improves the accuracy of capturing the acoustic field. Interaction of sound with solid boundaries is also examined in terms of reflection and diffraction. Sound propagation through an unsteady flow field is examined using static and dynamic flow/acoustics coupling demonstrating the importance of the latter. Proof of concept for the new method is provided by its application to the case of a conventional jet transport airplane, examining the effect of flow field and wing shielding on the near field noise levels.

During the aforementioned noise investigation and analysis, results on Blade Wake Interaction (BWI) noise were also reached. Presently, the mechanism of BWI noise generation, as well as the corresponding prediction model, are still under consideration. Helicopter rotor BWI noise is known to be significant during take-off and level flight, while less attention has been given to descent flight conditions, where BVI noise is dominant. Through signal analysis of the HELISHAPE descent case acoustic database, the rotor azimuthal region responsible for BWI noise is localized and the dominance of BVI noise in the BWI frequency region is shown. Coherence analysis of the blade pressure data indicate significant chordwise coherence in the 3 to 4 Struhal number range and absence of acoustic dipoles in the BWI frequency range. The findings of this study support BWI prediction models based on Amiet's theory and suggest that BWI noise can be ignored for predictions of rotor noise in descent flight conditions.

ACKNOWLEDGEMENTS

I would like to thank my supervisor Dr Penelope Menounou for her guidance and our excellent cooperation throughout my PhD studies. She has always been more than willing to hear and discuss any research issues and provide constructive advice, while in the same time let me find my own way through scie*n*tific research in a non-stressful way. I believe that she provided me with a perfectly balanced supervision and I consider myself fortunate to have been supervised by such a pleasant and positive person.

Moreover, I would like to acknowledge the invaluable help I received all those years from Professor Yannis Kallinderis. Through our conversations on the scientific part of my work, as well as on various subjects concerning the laboratory, he has successfully sculp*t*ed my professionalism and work manners.

My work would definitely have been a lot harder without the support of my fellow students Diamantis Karkantilidis, Evangelos Papaefthymiou and Kostas Kontzialis. Our meetings were always pleasant breaks from the demanding research env*i*ronment, sharing our common worries and providing each other with courage to continue. I will always look back on those memorable moments with joy.

Finally, I am nothing less but grateful to my family for their support and understanding throughout all the years of my studies. They have always provided a peaceful envir*o*n*m*ent for me, sharing my problems, my worries and successes and fuelling my scientific effort in a unique way.

This thesis is dedicated from my he*a*rt to Father Christoforos Mytilinis.

TABLE OF CONTENTS

TABLE OF FIGURES

TABLE OF TABLES

1 Introduction

The first chapter of the present thesis introduces the problem of air vehicle noise and describes the new elements of the present work.

1.1 The problem of air vehicle noise

The constant growth of aircraft operations in the last decades has brought to surface various environmental concerns. The gases and noise emitted by aircraft engines are the most important of them. Airplane noise, which is the subject of the present thesis, is one of those sounds which are undesirable to most of the observers and is of particular annoyance, especially on the people living in the vicinity of civilian and military airfields. As a result, since 1960s, when aviation noise became a public issue, governments have established regulations in order to reduce the aircraft noise levels.

In order to efficiently minimize air vehicle noise there is a need for accurate prediction and control methods. Aircraft designers and manufacturers have developed quieter aircraft trying to face the problem at its source. New turbofan engines have been built and new quiet technologies have been adapted in fuselage and aircraft system design. In terms of noise prediction, significant research has been conducted in the area of aerodynamic noise generation, allowing new technologies and optimization methods to be applied successfully, managing a significant reduction at the noise source. An example can be seen in Figure 1-1, where exhaust mixer technology has been adopted in low by-pass turbofan engine.

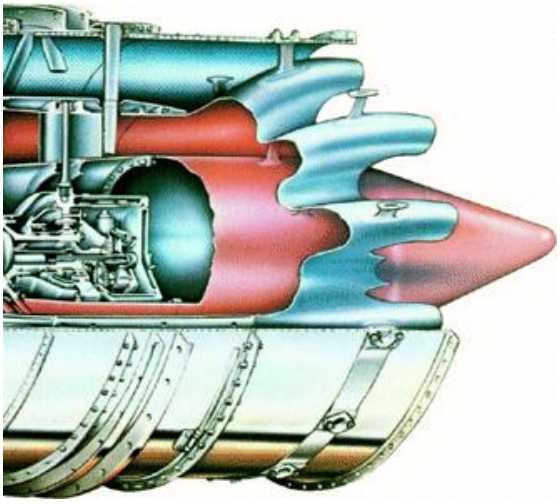

Figure 1-1: Exhaust mixer in low-bypass turbofan for noise suppression and improved propulsive efficiency. (Courtesy of Pratt & Whitney)

Besides the generation of air vehicle noise, the propagation from the source through the atmosphere and to the surrounding community sets another important parameter of the problem. The multiple effects that affect sound propagation in the atmosphere are now understood and efficient computation methods are available. Geometrical spreading, atmospheric absorption, refraction and nonlinear effects alter the initial noise level and characteristics and should be all taken into account in order to get an accurate prediction of the acoustic signatures reaching the areas of interest. These effects are either computed using tabulated values or empirical formulas, which are cheaper and less accurate methods, or using numerical techniques, which are more expensive but also more accurate methods. Figure 1-2 shows results of a modern computational tool regarding noise contours around a heavily used airport. These plots are used to evaluate noise levels and optimize the air vehicle operations at airports. Finally, besides noise generation and propagation, the noise problem can also be addressed at the receiver by application of insulation or other “passive” methods.

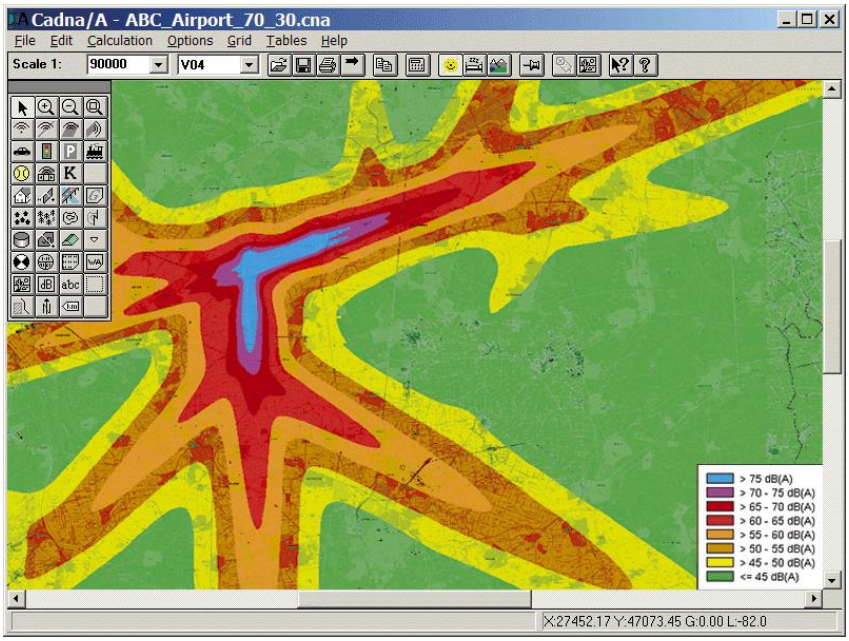

Figure 1-2: Noise contours around a heavily used airport produced by modern prediction software.

1.2 The present work

The present thesis focuses on the study of propagation of air vehicle noise employing numerical methods. Both cases of far field and near field propagation are examined, focusing on different effects and employing the appropriate numerical techniques. One dimension as well as multiple dimension propagation methods are used accordingly for each case.

Far field propagation of air vehicle noise in the atmosphere is mainly affected by geometrical spreading, atmospheric absorption, turbulent scattering, refraction and nonlinear effects. State of the art in nonlinear propagation shows that for the case of aircraft jet noise ignoring nonlinear propagation distortion effects leads to underestimation of the high frequency end of the spectrum. Extensive description of the effect as well as the relevant studies can be found in section 2.5.1. On the contrary, literature on nonlinear propagation of helicopter noise is not as extensive. Nonlinear distortion has been considered insignificant for helicopter noise, as the noise field produced by a helicopter rotor is, in general, of relatively low intensity (compared to the noise field produced by a jet aircraft). However, the increased operation of rotorcraft,

especially near inhabited areas, as well as the well known annoyance of helicopter BVI noise motivated the thorough investigation of nonlinear effects and BVI noise. Towards this investigation the experimental database of the HELISHAPE test is used together with a well known propagation method, the Burgers equation, to show that the effect can be important in certain cases. The frequency regions affected by nonlinear distortion, as well as the magnitude of the effect are determined and practical prediction methods are proposed.

Near field propagation of air vehicle noise requires different treatment than far field. The effects which are mainly affecting it are geometrical spreading, convection and refraction effects due to the flow field, as well as reflections and diffraction on the air vehicle surfaces. For the case of jet airplane in flight, the shielding of the engine noise by the fuselage and the wing significantly affects the aircraft's transmitted noise levels and has been the research subject of many recent studies. State of the art in the numerical methods used for near field propagation, as well as some recent applications are found in section 2.4.2 and the introductory section of Chapter 4. Taking into account that noise regulations are currently affecting the design of new aircraft, a cost effective way to determine the engine noise levels in the near field of complex geometry aircraft is needed. Towards this investigation, a new low order flow/acoustics interaction method applicable to hybrid grids is developed and applied to a conventional airplane geometry examining the effect of flow field and wing shielding on the emitted engine noise levels.

During the aforementioned noise investigation and analysis, results on Blade Wake Interaction (BWI) noise were also reached. Presently, the mechanism of BWI noise generation, as well as the corresponding prediction model, are still under consideration. State of the art in helicopter rotor BWI noise shows that it is significant during take-off and level flight, while less attention has been given to descent flight conditions, where BVI noise is dominant. Analytical description of the proposed mechanisms and research studies can be found in section 5.1. Investigation of the available descent database provides supporting evidence for suggested prediction models and conclusions on the importance of this noise source for descent flight conditions.

2 Air Vehicle Noise Sources and Sound Propagation

Air vehicle noise is the noise produced by any vehicle or its components during any phase of flight. Different air vehicle types have different noise levels and frequencies. The origins of air vehicle noise are three: (i) air flow, (ii) engine, and (iii) other aircraft systems. However the noise sources differ between different types of air vehicles and especially between helicopters and airplanes, as their flight operation is based on different concepts.

In the present thesis, helicopter noise and airplane noise are studied separately, as different propagation mechanisms are investigated for each case. In the following paragraphs helicopter and aircraft noise sources are briefly discussed noting the most important aspects for each case. Moreover the mechanisms that affect the propagation of air vehicle noise in the atmosphere are presented. Emphasis is given on nonlinear effects and interaction of sound with flow and solid boundaries, which are the effects that are mainly investigated in the following chapters.

2.1 Helicopter noise sources

Helicopter rotors produce a very complicated directional noise field through several distinct noise generation mechanisms. Their acoustic spectrum consists of deterministic discrete-frequency noise components, as well as, of non-deterministic broadband noise components. The various noise types are attributed to different generation mechanisms some of which are analogous to the blade tip velocity or blade tip Mach number, where Mach number (M) is defined the ratio of the velocity to the local speed of sound. Other flight parameters that are important for helicopter noise sources are the advance ratio (μ), which is the ratio of forward flight speed to the speed of the rotor tip of a helicopter, and rotor tip path plane angle (a_{tpp}), which is the angle between the rotor blade tip and the helicopter's path plane. The reader is referred to review papers, such as those of Brentner and Farassat [1,2] or Schmitz [3], for a detailed description of helicopter noise. A brief outline is given next.

- **Thickness and High-Speed Impulsive noise**

Thickness noise is caused by the displacement of the air by the rotor blades. It is dependent only on the shape and motion of the blade and is primarily directed in the plane of the rotor. The pressure time history of thickness noise is characterized by a large negative pulse. As the Mach number of the blade tip is raised towards 0.9, the radiation effectiveness of the noise produced by the blades' motion, increases dramatically in amplitude. The negative pulse becomes quite narrow and impulsive in character, radiating large amounts of in-plane high-frequency acoustic energy. This extreme of thickness noise is called High Speed Impulsive noise (HSI) and is the dominant source of rotor harmonic noise when it exists. At around Mach 0.9 a shock forms on the rotor blade which can eventually radiate to the acoustic far field. The process is known as "delocalization".

- **Blade-Vortex Interaction noise**

Blade-Vortex Interaction (BVI) noise is another source of high-frequency periodic noise and one of the most important sources of rotor radiated noise. This noise occurs as a result of the interaction of the blade with vortices from preceding blades. It has been a source of major concern for many years and as a result of recent research, some of the details of the interaction are now becoming better understood. Figure 2-1 shows typical interaction patterns on a rotor disk in a descending fight of a rotorcraft, in which several interactions on both the advancing and retreating sides occurred.

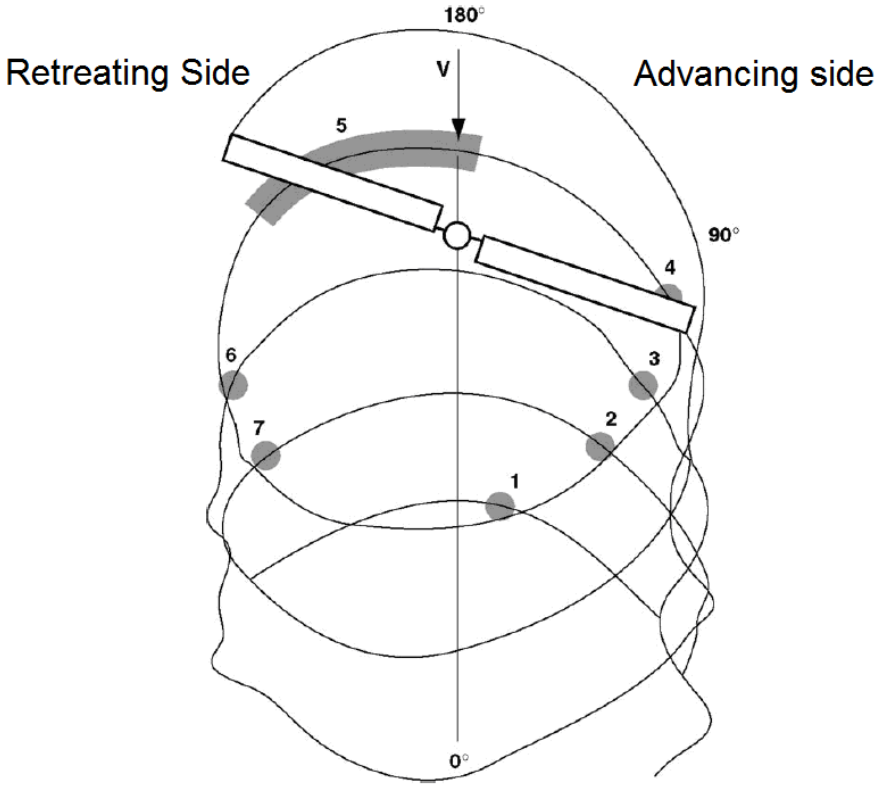

Figure 2-1: Blade-vortex interactions during descending flight (number 1-7 indicates blade-vortex interactions) [4]

However, these interactions do not equally contribute to far-field noise. Pressure fluctuations on the retreating side are, for example, more intense than those on the advancing side, but contribute much less to far-field noise. Among several interactions on the advancing side, only parallel or near-parallel interactions turned out to be major contributors to noise.

Typical time signatures and frequency spectra of blade-vortex interaction noise at far field are shown in Figure 2-2, in which distinctive pulse shapes are shown. The noise signatures show several interactions and each consists of positive and negative amplitudes, with positive amplitudes dominant on the advancing side and negative amplitudes on the retreating side. This sign change of noise signatures is due to the fact that rotational directions of vortices on the advancing and retreating sides are opposite during blade-vortex interactions. The noise pulses are rich in high harmonics of the rotor fundamental frequency and contain many distinctive harmonics in a high-frequency range. Recently, several wind tunnel tests with model-scale rotors were

carried out to measure noise footprints in a horizontal plane under the rotor for examining residential noise exposures.

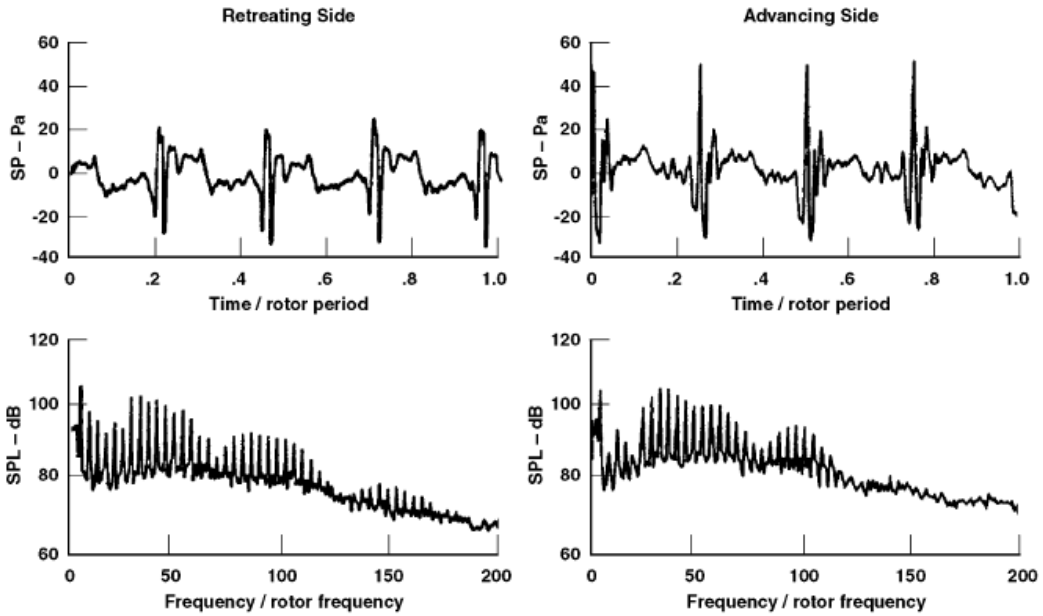

Figure 2-2: Typical BVI noise characteristics in the time domain (upper line) and frequency domain (lower line) [5]

- **Blade-Wake Interaction noise**

Broadband noise can be one of the important contributors to the subjective assessment of rotor annoyance in situations where impulsive noise is notably absent. The mechanisms that produce broadband noise are more than one and their common characteristic is that they generate continuous acoustic spectra. This noise occurs when blades interact with either the turbulence of the rotor wake generated by other blades, or the blade boundary layer, or atmospheric turbulence in which the rotor operates.

The broadband noise that is generated due to the interaction of the blade with the rotor wake turbulence is termed Blade-Wake Interaction (BWI) noise and its frequency range is found to be about four times that of dominant BVI noise frequencies. Moreover there is strong dependence of this mechanism to advance ratio and rotor tip-path plane angle [6] with its greater significance being during takeoff flight conditions. A further analysis of BWI mechanism and proposed prediction methods is given in Chapter 5.

- **Self noise**

Self-noise is another broadband noise mechanism and it is mostly noticeable on helicopters during start-up or shut down in the acoustic near-field and it is often characterized as a whooshing sound. It is found at the higher frequency part of the broadband noise spectrum and it is attributed to the noise generated by the blade interacting with its boundary layer. This sound is thought to be important only when all other sources of noise are mitigated, or at very low tip Mach numbers that are not encountered in normal helicopter flight.

Figure 2-3 shows an interaction of a blade with the flow field resulting from previous blade passages and points out the different parts that are responsible for the various broadband noise mechanisms.

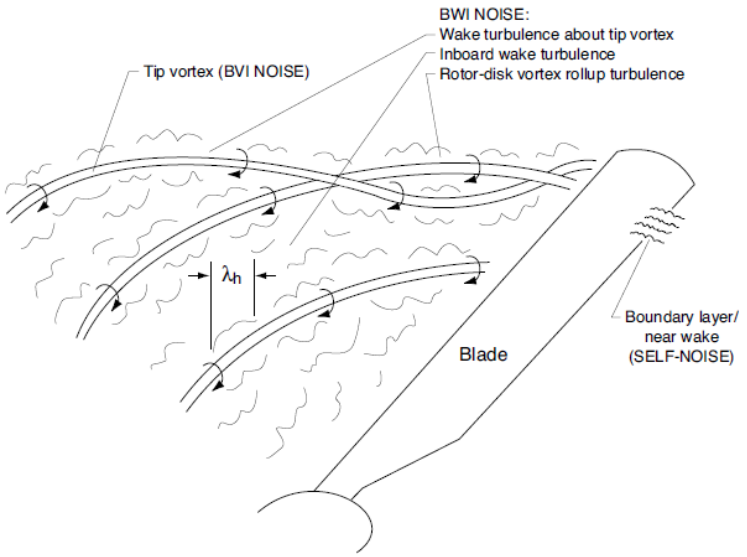

Figure 2-3: Illustration of blade encountering a turbulent field generated by the other blades of the rotor [6]

- **Tail rotor noise**

While most noise from a helicopter is generated by the main rotor, the tail rotor is a significant source of noise for observers relatively close to the helicopter. The tail rotor noise is generally of high frequency noise content, which can be acoustically significant when the helicopter is operating close to the ground as it has not been

attenuated yet by the atmosphere. The basic mechanisms of tail rotor noise radiation are essentially the same as on the main rotor, with the addition of the interaction of the tail rotor with the wake coming from the rear fuselage and fin.

- **Other helicopter noise sources**

Other principal noise sources on helicopters are the engine and gearbox. On several helicopters the gearbox noise can be detected during overflight. However, normally it is not of critical importance since it is of higher frequency and it tends to attenuate fast during propagation to a distant observer. On the other hand, engine noise has a broadband character and is often not immediately observed either subjectively, or in the spectral analysis [7].

2.2 Airplane noise sources

As it has already been stated in the beginning of the chapter, airplane noise sources are completely different from the helicopter ones. Airplane noise is generally divided into two sources: that due to the engines and that associated with the airframe itself. As quieter higher bypass ratio engines have become more common and aircraft have become larger, interest in airframe-related noise has grown, however engine noise still accounts for most of the external noise. [8]

2.2.1 Propulsion Related Noise

A modern jet aircraft engine gives rise to many different noise sources, where each of them has different characteristics in terms of acoustic levels, frequency content and directivity. Moreover, depending on the flight conditions, the importance of each source changes dramatically. Figure 2-4 displays an engine cut, as well as the location of its most important noise sources.

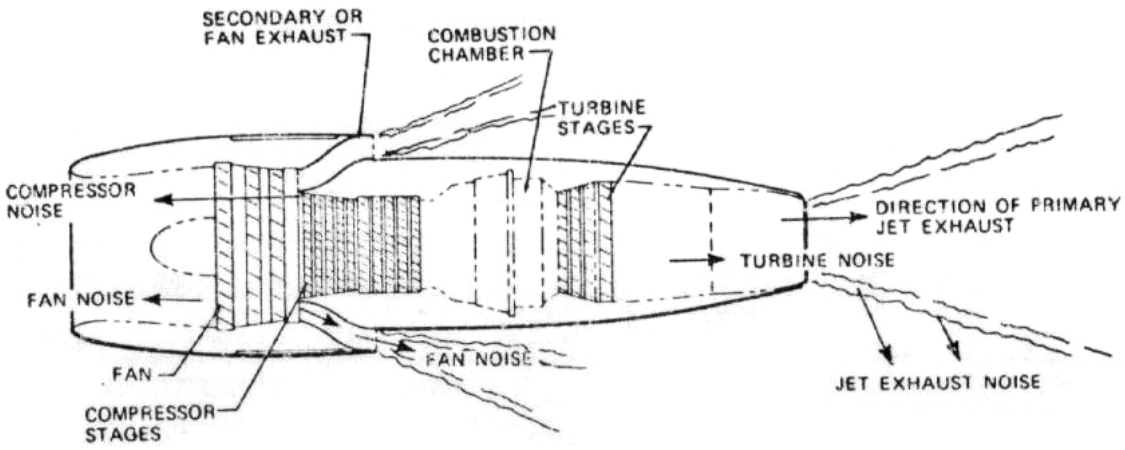

Figure 2-4: Jet engine cut and various sources of propulsion noise [9]

These sources can be subdivided into two main categories which are described next: jet noise and turbomachinary noise.

- **Jet noise**

It was during the Second World War that the use of jet engines in military aircraft started to raise concerns regarding jet noise. Since then jet noise started to receive attention and at the early 1950s' it has become a separate branch of aeroacoustics. However, our understanding of jet noise as a study in aerodynamic noise had its foundations in the work of Lighthill [10-11] on "sound generated aerodynamically". That work was complemented by several experimental studies which validated Lighthill's theory. Since then many studies have contributed to jet noise understanding and prediction by applying modifications to Lighthill's acoustic analogy.

In simple words, jet noise is linked to the intense exhaustion of the burnt gases at high temperature. Downstream of the airoplane wings, the jet generates strong turbulence as it enters a still area. Jet noise generally increases with the engine thrust and is of primary importance during the take-off phase, where engines are working close to their maximum power.

The main characteristics of this noise source are the following:

i) Generation area is located rear of the engines, at a distance equivalent to a few nozzle diameters

ii) Noise directivity is strong, heading for the back of the aircraft

iii) Noise generated does not contain distinct tones, and its frequency band is quite wide.

- **Fan and other turbomachinary noise**

Air vehicles commonly use propulsion turbomachinary, which use rotating and stationary blades to provide thrust. Fans, compressors and turbines each can generate significant tonal and broadband noise.

The most prominent component, the fan, is the primary turbomachinary noise source. Compressor and turbine noise can be important at low power settings, particularly for the blade rows nearest the core inlet or exhaust. Other propulsion systems, such as the turbojet and turboprop, have similar components to that of turbofan and acoustic characteristics are also similar. Regarding the flight phases that turbomachinary noise is of primary concern, these are takeoff and approach phases.

The main characteristics of fan noise source are the following:

i) Noise produced by the fan results of the superimposition of a wide-band noise (as for the jet) and noise with harmonics.

ii) Wide band noise is due to the boundary layer developing on the fan blades, and more generally to the airflow around them.

iii) Harmonics are originating in the intrinsic cycling character of the fan motion (spinning motion). The most remarkable frequency is the fundamental, the value of which is the number of blades times the fan rotation speed. The harmonics are multiples of this fundamental.

Compressor noise is of the same type as the fan noise, but the harmonics are less prominent due to the interaction phenomena that take place at that part of the engine.

The graph shown in Figure 2-5 is representative of the noise distribution components for typical aircraft. The importance of engine noise, in particular the fan and jet exhaust noises is clearly depicted.

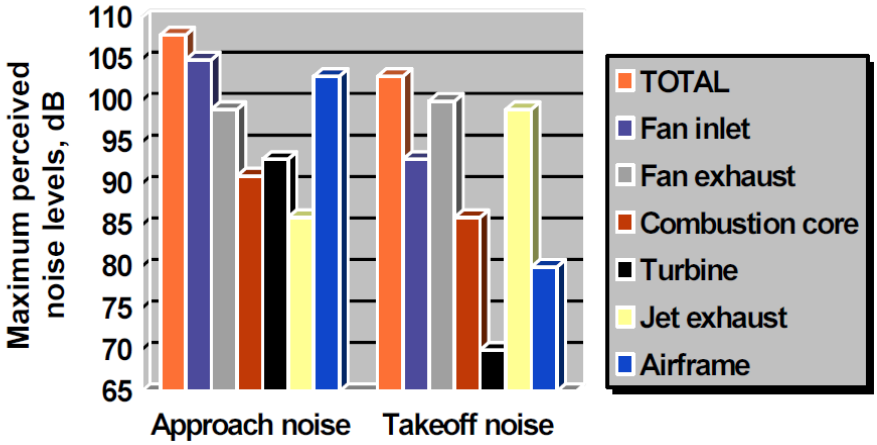

Figure 2-5: The relative importance of different sound sources to the total perceived level [9]

2.2.2 Airframe Noise

Airframe noise is the non-propulsive noise emitted by an aircraft in flight and became a topic of research interest in the 1970's, following initial studies that were made on the construction of a quiet military air vehicle. This type of aerodynamic noise is attributed to the flow around the various airframe parts and is of dominant importance during the approach phase, where the engine power is the lowest. Airframe noise sources of a conventional airplane are shown in Figure 2-6.

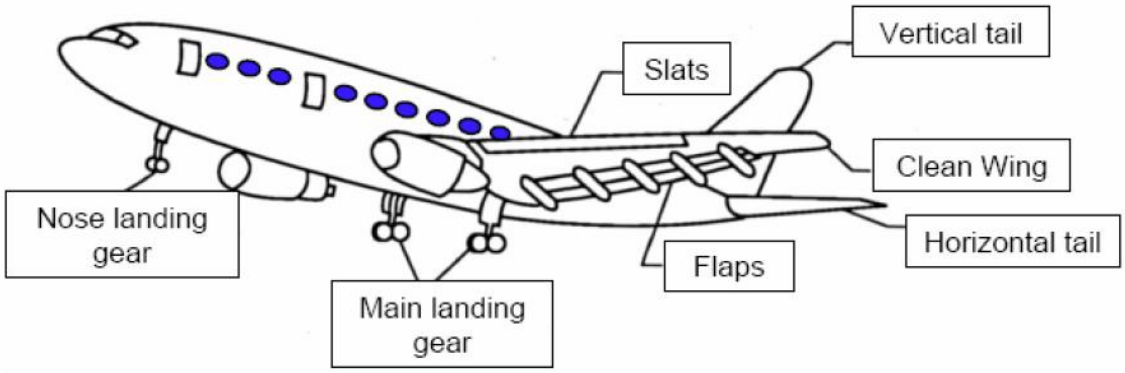

Figure 2-6: Airframe noise sources [12].

Some of the most important airframe-noise generating mechanisms are the following [8]:

- **Trailing edge noise**

  When turbulent boundary layer eddies are convected past the trailing edge of a large (relative to acoustic wavelength) body, their aeroacoustic source characteristics are modified by the edge, and a more efficient source results. This scattering mechanism produces strong, broadband radiation to the far-field. If there is coherent vortex shedding, typically associated with blunt trailing edges and/or high angles of attack, tonal or narrowband noise is also present.

- **Flap side-edge noise**

  The flap side-edge noise constitutes a significant portion of the overall airframe noise during descent and landing of an aircraft. The acoustically relevant flow features at typical flap side edges consist of free shear layers, the roll-up of these layers to form multiple vortices, merging of vortices, and, at high flap deflections, breakdown of these vortices. Because of their unsteadiness and their proximity to flap side-edge surface, these features can contribute to the noise radiated from the flap side edges.

- **Undercarriage gear noise**

  The components of an undercarriage are mostly bluff bodies of a wide range of shapes and aspect ratios: wheels, axles, struts, shafts. Unsteady separated flow past them (vortex shedding) and wake interactions between them give rise to broadband sound over a wide frequency range. Low-frequency tones may also be produced, even in a generally turbulent flow, by the interaction of flow with the cavities forming the wheel wells.

- **Cavity noise**

  Cavity noise is one of the most important airframe noises. When flow passes over a cavity or opening, due to vortex shedding at the upstream edge of the cavity, intensive tone noises may be generated. Strong tonal oscillations occur in a feedback loop between the two edges of the cavity opening.

2.3 Sound propagation effects

The propagation of sound and its interference with solid surfaces is a rather complicated problem. Many different wave propagation mechanisms in the free field, as well as effects due to the presence of the ground or other solid obstacles, are involved. In the following paragraphs these mechanisms are briefly discussed [13].

- **Geometrical spreading**

As the distance from the sound source increases, the energy carried by the acoustic waves spreads out. At distances that are comparable to the size of the sound source, the acoustic fronts spread spherically in three dimensions provided that the atmosphere is isotropic. Assuming that the point source approximation is applicable, the sound level decreases at 6dB per doubling of distance. The effect of geometrical spreading is the same for all acoustic amplitudes and frequencies and can be characterised as the dominant effect for the case of noise propagation in the atmosphere.

- **Atmospheric absorption**

The effect of atmospheric absorption describes the absorption of sound energy by the atmosphere and is a significant function of frequency, temperature, pressure, and humidity. Two basic physical mechanisms are responsible for this effect. The first of them translates to the direct conversion of acoustic energy to heat energy through processes involving heat transfer and heat conduction. These two processes are known

today as classical absorption. Classical absorption is a function of temperature, pressure and frequency and is the dominant absorption mechanism at high frequencies.

The second mechanism of atmospheric absorption is molecular relaxation. The energy of the acoustic wave, as it propagates through the atmosphere, is converted to rotational and vibration energy of oxygen and nitrogen molecules through collisions. The oxygen relaxation provides maximum absorption at frequencies above about 2 kHz, while nitrogen relaxation below 2 kHz [see Figure 2-7]. The concentration of water vapour also plays a role in this mechanism as collisions with water vapour molecules speed the energy transfer process.

These mechanisms have been extensively studied, empirically quantified, and codified into an international standard for calculation: ANSI Standard S1-26:1995, or ISO 9613-1:1996.

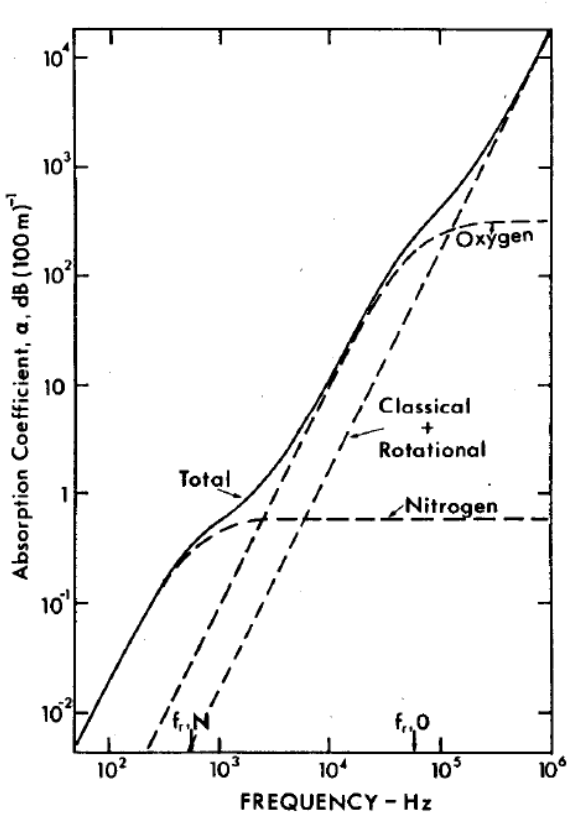

Figure 2-7: Predicted atmospheric absorption in dB/100m for a pressure of 1 Atm, temperature of 20C and relative humidity of 70% [ref. ANSI standard S1.26].

- **Turbulent scattering**

An acoustic wave propagating through the atmosphere can be significantly altered by non-homogeneities in atmospheric density, temperature and wind velocity. These fluctuations are loosely called turbulence. One of the major effects of turbulence in the atmosphere is to cause amplitude and phase fluctuations in the sound waves passing through the air. These fluctuations can cause substantial fluctuations in the time-averaged root-mean-square (rms) sound pressure level for certain conditions. A second major effect of atmospheric turbulence is to scatter the sound away from the observer, which changes the directivity pattern and causes a net attenuation at the observer's position. It should be also noted that the size of eddies in the atmosphere affect the frequency range of the acoustic spectrum that is attenuated. For the prediction of this effect, among others Daigle [14] created a model that accounts for the variance of sound amplitude due to turbulence to predict the statistical mean value of sound pressure and achieved good agreement with experimental data.

- **Nonlinear effects**

High amplitude sound wave experience nonlinear distortion due to the difference in travelling speeds of the different parts of the sound wave. Through this distortion the energy of the wave is transferred to higher frequencies, while in extreme cases a shock can form. Nonlinear effects are more significant at propagation of high amplitude jet noise whereas their effect on helicopter rotor noise has not been extensively studied. A thorough description of this mechanism is given in paragraph 2.3.1.

- **Refraction**

The differences in temperature and wind which occur near the ground cause the effect of refraction. The velocity of sound relative to the ground is a function of temperature and wind velocity, and hence it also varies with height, causing the sound waves to propagate along curved paths [Figure 2-8 and Figure 2-9]. Depending on the gradient of the atmospheric properties, the refraction effect can propagate the acoustic

waves in greater distances (downward refraction) or cause acoustic shadow regions (upward refraction). Except from meteorological conditions near the ground, refraction effects can also be seen in acoustic waves propagating near the surface of an aircraft, as the flow field changes considerably around it.

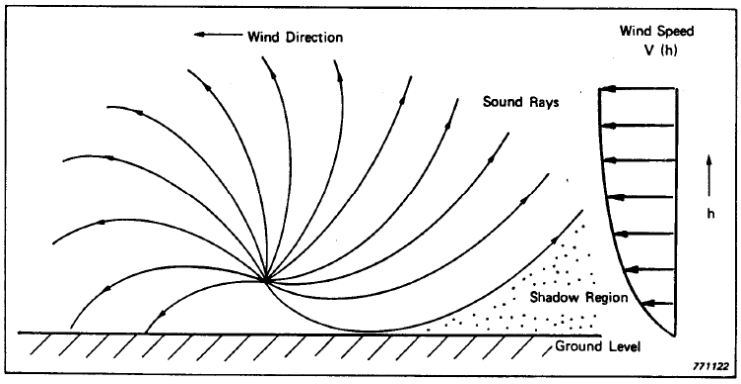

Figure 2-8: Refractive effects caused by wind. [15]

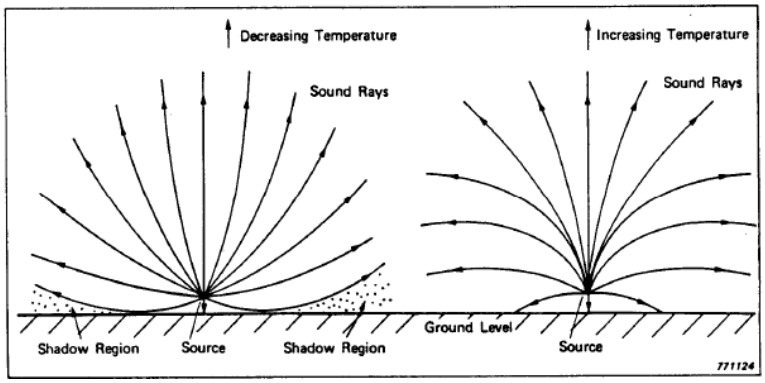

Figure 2-9: Refractive effects caused by temperature gradients: upward refracting (left) and downward refracting (right) [15]

Determining excess attenuation due to refractive effects is not an easy task. Complex models that allow the user to specify the sound speed as a function of altitude are needed, such as ray tracing. Refractive effects can cause both increases and decreases in sound levels compared to a uniform medium. One common approach is to calculate the sound level assuming no refraction, on the assumption that this probably represents a good prediction of the equivalent, or time averaged sound level that would

be observed [15]. Beside this approach, CAA methods which couple the flow and acoustic fields, can take into account refraction effects computationally.

- **Interaction with solid boundaries**

Except from the atmospheric propagation mechanisms, there are also other phenomena which occur only due to the presence of the ground or any other solid boundaries and are usually most significant near those surfaces. The reflection which takes place at a solid surface results in the interference of the reflected with the direct field. The height of the receiver and the type of the surface are important parameters for this mechanism. Another significant phenomenon that is observed when the propagated sound encounters a solid obstacle is diffraction. Diffraction is the result of interaction of the incident sound wave with the edges of the solid object. These two mechanisms are described extensively in paragraph 2.3.2.

From all the aforementioned propagation effects, those which are investigated numerically in the present thesis are nonlinear effects and interaction with flow and solid boundaries. Those effects play a significant role in air vehicle noise propagation and are further elaborated in the following paragraphs.

2.3.1 Nonlinear effects

All parts of a noise signal with relatively low amplitude (small signal or linear case) propagate with the same velocity, namely the speed of sound. As a result, all points of the signal maintain their position with one-another and the shape of the signal remains the same throughout the propagation. In the finite-amplitude or nonlinear case, (in other words, when the noise signal is of high intensity), each part of the signal travels with its own velocity, namely the speed of sound plus the local velocity of the signal. Parts of the signal travel faster than the speed of sound, while others move slower. As a result, the original shape of the signal distorts. Consider, for example, an initially sinusoidal signal. The points of the waveform at zero crossings travel with the speed of sound, the positive peaks travel faster, while the negative peaks slower. As

seen in Figure 2-10, the positive peak "catches up" with the zero crossing ahead and the part of the waveform connecting it with the zero crossing steepens, until eventually a shock is formed. In the frequency domain, the steepening corresponds to generation of higher frequencies and energy transfer to the high frequency end of the spectrum. The larger the pressure amplitude of a noise signal, the greater the differences in the velocity between its points and, thus, the sooner the signal distorts. The effect is counter-acted by any mechanism that decreases the pressure amplitude, most notably, by geometrical spreading and absorption. The final shape of the noise signal (and the corresponding frequency re-distribution) depends on the combined effect of these competing mechanisms.

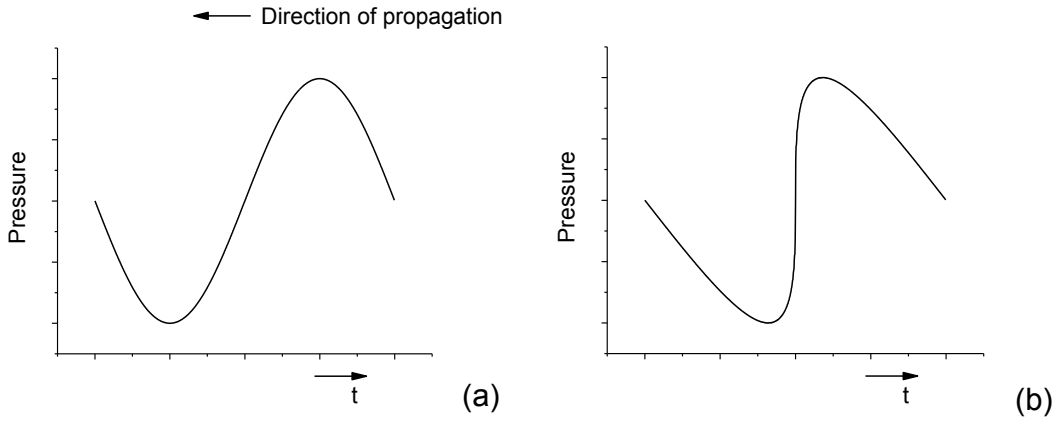

Figure 2-10: Progressive distortion of a finite amplitude wave. Initial sinusoidal waveform (a) and distorted waveform forming a discontinuity in pressure (b).

Nonlinear propagation distortion has been studied extensively, with the first equation for plane waves in non-dissipative fluids dating back to Poisson. Since then, a vast body of published work has enabled the prediction of the nonlinear evolution of a signal under the combined effect of several propagation mechanisms. Analytical solutions exist for simple source conditions and propagation environments. For more complex noise sources and/or propagation environments the solutions are obtained numerically, where algorithms have been developed for implementation either in the time, or in the frequency domain, or switching between time and frequency domain. A short informative illustration of nonlinear effects in the context of airvehicle noise propagation in atmosphere is given by Embleton and Daigle [16]. For a detailed

presentation of governing equations, available solutions, and numerical algorithms the reader is referred to Hamilton and Blackstock [17].

2.3.2 Reflection and diffraction effects

Propagation effects caused by the ground (or any other solid surface) are most significant within a few wavelengths, that is, only a few meters above the ground surface. Furthermore, the ground has a greater effect on waves travelling almost horizontally near the ground, than those that are coming from nearly vertical directions. The dominant effects of a solid surface to acoustic waves are reflection and diffraction.

- **Reflection**

The sound that is emitted from a source above a solid surface, reaches the receiver via two paths: (i) directly from the source to the receiver, the direct field, and (ii) after being reflected from the surface between the source and the receiver, the reflected field (Figure 2-11).

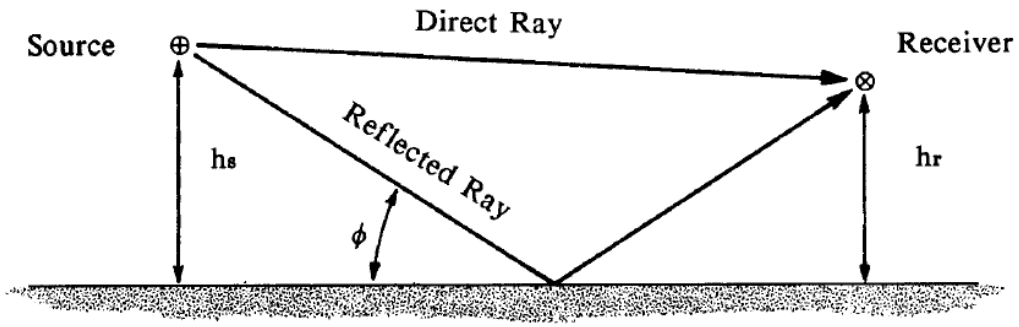

Figure 2-11: Geometry for reflection of sound from level ground [15]

Reflection depends strongly on the type of the surface and in cases that it is porous, like the ground, its acoustic impendence is complex. This phenomenon is associated with a complex reflection coefficient which is rarely as large as unity and is a function of the angle of incidence. The sound reflected from a surface experiences both

changes in amplitude as well as phase changes between zero and π radians. Another significant effect of reflection is when the incident wave is of some other shape except plane (e.g., spherical). Then the different parts of the wave front meet the plane surface with different angles of incidence and are subjected to reflection coefficients that differ in amplitude and phase. Thus the reflected wave has a different shape than the incident.

- **Diffraction**

As defined in earlier the processes of diffraction arise from of interaction of the incident sound wave with the edges of the solid object. Far from any boundaries a sound field propagates in a relatively simple way, and one can exploit this simplicity by describing the propagation in terms of ray paths. However, if a large solid body blocks the sound field, the ray theory of sound propagation predicts a shadow region behind the body with sharply defined boundaries, so in principle, on the one side of the boundary there is a sound field with well defined amplitude and phase and on the other side of the boundary there is essentially silence. This does not happen in practice; as the waves propagate, sound “leaks” across this sharp boundary in ways governed by the laws of wave motion and the boundary becomes less sharp. Diffraction effects are most clearly evident in the vicinity of solid boundaries, along geometrical ray boundaries such as the limiting ray shown in Figure 2-12.

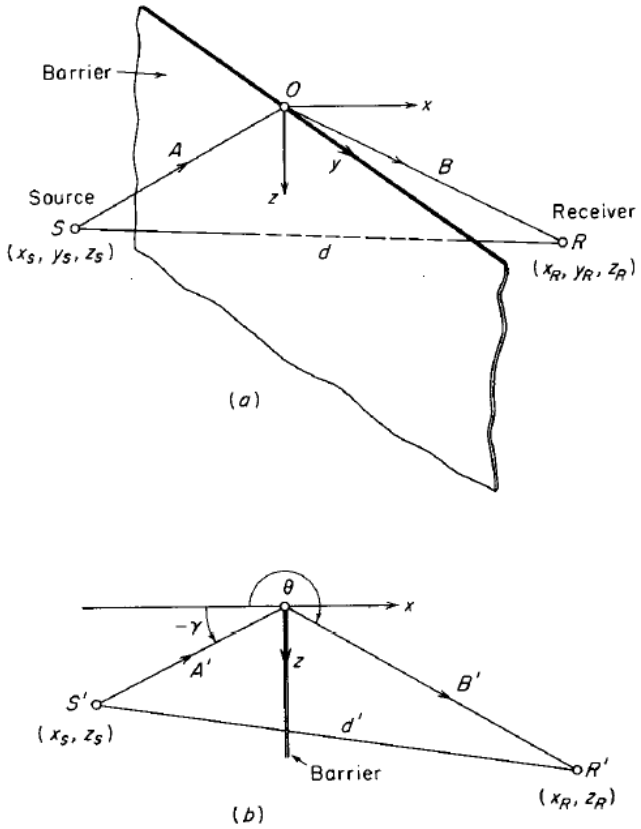

Figure 2-12: Geometry for sound propagation path over a barrier wall: (a) perspective view and (b) projection plane perpendicular to the barrier [15]

Acoustic diffraction occurs in conjunction with a wide range of solid bodies: some such as thin solid barriers are erected alongside highways or are carefully located to shield residential communities from aircraft noise, while others such as buildings are often built for other purposes, but fortuitously provide some beneficial shielding.

2.4 Numerical methods used in sound propagation

There are many different numerical approaches that can be applied for the solution of sound propagation problems. The appropriate method for each propagation case depends on the various parameters of the aeroacoustic problem, the effects involved, the propagation range and the requested accuracy. These numerical methods can generally be split into two great categories whether they propagate sound in one or multiple spatial directions.

2.4.1 One direction wave propagation methods

The first category of methods, often characterized as traditional methods, considers the sound source as initial or boundary condition and is widely used for the propagation of sound in the far field over great distances. The computational cost for solving the relevant equations is particularly small. These methods can allow for nonlinear effects in sound propagation, for example [18], and are easy to apply. However, their greatest disadvantage is that they are restricted to one direction of propagation and include simplifying assumptions in their formulation regarding the source [17].

The second-order wave propagation equation is a standard equation of this category and is derived from the basic equations of mass conservation, momentum conservation, entropy balance and thermodynamic state. It is used to describe dissipative and nonlinear effects. Based on this equation, others are derived, for example the Westervelt equation which is an approximation of the second order wave equation when cumulative nonlinear effects dominate local nonlinear effects.

Burgers equation (BE) is another form which is derived from the one dimensional Westervelt equation. It is the simplest equation that describes the combined effect of nonlinearity and thermo-viscous attenuation in the propagation of a sound wave. In its augmented form, the Burgers equation includes the effect of geometrical spreading, which in the case of air vehicle noise propagation translates to spherical spreading. It also includes the absorption and dispersion attributed to the molecular relaxation of O_2 and N_2 in the atmosphere. It can, therefore, be employed for the prediction of finite-amplitude sound emanating from a point source and propagating through the atmosphere. The atmosphere is considered homogeneous and at rest. It is being described by its temperature and relative humidity, which in turn determine the absorption due to molecular relaxation. A form of the augmented Burgers equation [17,19] is the following:

$$\frac{\partial p}{\partial r} = -\frac{1}{r}p + \frac{\beta}{\rho_o c_o^3} p\frac{\partial p}{\partial \tau} + \frac{\delta}{2c_o^3}\frac{\partial^2 p}{\partial \tau^2} + \sum_v \frac{c_v'}{c_o^2}\int_{-\infty}^{\tau} \frac{\partial^2 p}{\partial \tau'^2} e^{-(\tau-\tau')/t_v} d\tau' \qquad (2.1)$$

where p is the sound pressure, r the propagation distance, $\tau = t-(r-r_o)/c_0$ the retarded time with r_0 being the radius of the point source, ρ_0 is the ambient density, c_0 the small signal sound speed, β the coefficient of nonlinearity, δ the diffusivity of sound for viscosity and heat conduction, and $\nu = 1, 2$ is the index of the two relaxation processes, each characterized by a relaxation time t_v and the corresponding net increase in phase speed (c'_v), as frequency varies from zero to infinity. The first term in the right-hand-side of Eq. (2.1) represents the spherical spreading, the second the nonlinear distortion, the third describes the thermo-viscous attenuation, while the fourth term combines the two relaxation effects, corresponding to O_2 and N_2. The third and fourth term together describe mathematically the atmospheric absorption.

An augmentation of the Burgers equation is the KZK equation and is the most widely used model equation for describing the combined effects of diffraction, nonlinearity, and absorption in directional sound beams.

The one direction propagation method that is used in the present thesis for the study of nonlinear effects, is the augmented Burgers equation as described by Eq. (2.1).

2.4.2 Multiple direction wave propagation methods

The second category of numerical propagation methods, named multiple direction wave propagation methods, solve the acoustic equations over the whole 2D or 3D domain, similar to Computational Fluid Dynamics (CFD) methods that are used in flow field studies. They can capture complex phenomena, however they are computationally expensive and their use is generally limited to near-field problems in order to predict aerodynamic generated sound or the interaction of the acoustic field with complex flow fields and complex solid boundaries.

However, the nature of aeroacoustics problems is essentially different from that of standard aerodynamic problems and presents some challenges to Computational Aeroacoustics (CAA) that are not encountered in CFD. Primary issues include:

(i) A large portion of CFD applications concerns steady state problems. On the other hand one of the main characteristics of the acoustics problems is that they are highly time dependent.

(ii) There is a huge difference between the magnitudes of the flow and the acoustics quantities. In order to give accurate results, a CAA scheme should have very low dispersion and dissipation errors.

(iii) It is important that the acoustics computational solution is uniformly valid throughout the computational domain, both close to the source region and in the far field.

(iv) Acoustics fields are frequently multi-scale problems, in both time and space.

For these reasons, the "blind" application of traditional CFD techniques to aeroacoustics problems has proven to be ineffective.

The main CAA approaches can be divided into several broad categories: (i) Acoustic Analogies, (ii) Kirchhoff's and Boundary Element Methods, (iii) High Order CFD Methods, and (iv) Combined CFD/CAA Formulations. For more details on the computational challenges of CAA see [20]. A short review of the main approaches to numerical prediction of sound propagation follows.

The methods based on the classical acoustic analogy introduced by Lighthill [10] fall into the first category. A rearrangement of the compressible continuity and momentum equations of motion leads to a double divergence source-like term known as "the Lighthill stress tensor". The terms not appearing in the linear wave operator are grouped into the stress tensor, and all non linear effects are accounted for by this tensor, as well. This method was further extended by Curle [21] to include the effects of solid boundaries, and by Ffowcs Williams and Hawkings [22] to account for the arbitrary movement of aerodynamic surfaces.

Kirchhoff's surface-integral method assumes that the sound transmission is governed by the simple wave equation. Initially a surface which encloses all nonlinear flow effects and noise sources is selected. The pressure, its normal derivative and time gradient over the surface are used as an input to predict the sound field. The pressure

values over the surface are obtained from a near field CFD or CAA simulation. For more details see [23]. Boundary Element methods can fall into the same category. They were originally developed for solid mechanics and stationary fluid problems, but they have found use in Aeroacoustics applications. More details about boundary element methods can be found in [24].

Due to the large difference between the values of the flow and acoustic pressure (sometimes larger than three orders of magnitude) a low order scheme would not be able to resolve the acoustic variations, as they would be comparable to the numerical error. High order schemes including the spectral methods offer a way to deal with resolution of the weak sound disturbances. According to studies [25,26], high order CAA Finite Difference schemes can yield the necessary accuracy and wave propagation properties to calculate linear waves with minimal grid resolution. For example, Sparrow et al. [27] used a Finite Difference scheme for finite amplitude wave propagation in two dimensions, including classical absorption effects and nonlinear effects. However, high order techniques are computationally demanding and primarily applicable to simple geometries and structured computational meshes. They are also not directly applicable to flows with discontinuities, such as shock waves. Further, application of high order schemes with hybrid 3-D grids is a challenge. These methods include the Dispersion-Relation-Preserving (DRP) scheme [25], the optimized explicit scheme [26], the optimized compact methods [28], the wave number extended upwind methods [29], and Leapfrog-type schemes [30]. Spectral methods [31] involve approximations of the solution by Fourier series or orthogonal polynomials. A more detailed review of modern CAA methods and especially high order finite difference schemes can be found in [32].

Another category of CFD /CAA methods focus on achieving simulation of the sound propagation, via the *separate* computation of the sound and flow fields. In these combined CFD/CAA methods, the acoustic quantities are considered as a perturbation to an aerodynamic field. The acoustic solution is obtained at a second step, after the mean fluid flow is computed. The main advantage of this approach is that one can apply the most suitable computational scheme and mesh for each field. Hardin and Pope [33], who suggested a decomposition of the total flow variables into incompressible mean flow quantities and acoustic perturbations, were one of the first to propose such an approach for the prediction of sound generation and propagation. According to this

method, mean time-dependent values of flow velocity and flow pressure are obtained by solving the incompressible Navier-Stokes equations. Next, the sound field is computed from the compressible inviscid equations for the acoustic perturbations, with the incompressible terms acting as forcing functions. This method was developed further by Ekaterinaris [34], Slimon et al. [35], Shen and Shorensen [36,37] and Farshchi et al. [38]. A similar technique is that of the Nonlinear Disturbance Equations (NDE) [39] which is based on the assumption of a statistically stationary flow to decompose the flow field into its mean value and an acoustic perturbation. The technique has been further developed by Hansen et al. [40] and Kozubskaya and Abalakin [41]. Other similar techniques include that of Bechara et al. [42], Viswanathan and Sankar [43], the Perturbed Nonconservative Nonlinear Euler Equations (PENNE) [44], the Linearized Euler Equations with Sources (LEE+S) [45], the Acoustic Perturbation Equations (APE) [46], and the method of Gabard et al. [47]. The majority of aforementioned methods employ structured meshes.

In the present thesis a new low order multiple dimension wave propagation method is developed, applicable to complex geometries for the study of sound interaction with solid boundaries.

2.5 Far field and near field studies

The air vehicle noise propagation study made in this thesis is divided in two parts, the far field and the near field. Each of these studies is concentrated on the sound propagation mechanisms that are dominant for the specific case and uses a numerical method that is best suited for it. Cost effectiveness is a significant parameter for the method that will be chosen for each case, as all parts of this analysis are made on a single desktop computer.

2.5.1 Far field study concept and motivation

Far field propagation of air vehicle noise in the atmosphere is mainly affected by geometrical spreading, atmospheric absorption, turbulent scattering, refraction and

nonlinear effects. In the present study, the atmosphere is considered homogenous, which allows refraction and turbulent scattering to be ignored. As geometrical spreading and atmospheric relaxation effects have been studied extensively in the past, nonlinear propagation effects are going to be the subject of interest for this far field study. The method that best applies for this case in terms of mechanism analysis and cost effectiveness is a one direction propagation method and specifically the Burgers equation.

Nonlinear propagation of aircraft jet noise has been considerably studied, showing that ignoring nonlinear propagation distortion effects leads to underestimation of the high frequency end of the spectrum [48-52]. On the contrary, literature on nonlinear propagation of helicopter noise is not as extensive. Nonlinear distortion has been considered insignificant for helicopter noise, as the noise field produced by a helicopter rotor is, in general, of relatively low intensity (compared to the noise field produced by a jet aircraft). Existing literature focuses in the special cases of transonic/supersonic flows around the blade tip, where shock waves of large pressure amplitudes are formed and, after dislocating from the blade surface, propagate in the surrounding medium [53,54]. Cases of Blade Vortex Interaction (BVI) noise have not been considered. The premise was that the pressure amplitude of a BVI noise signal is small enough that shape distortion can be ignored. However, the increased operation of rotorcraft, especially near inhabited areas, as well as the well known annoyance of helicopter BVI noise motivated the thorough investigation of nonlinear effects and BVI noise.

To sum up, the far-field part of this thesis is studying the nonlinear propagation of helicopter rotor noise using a well known one direction wave propagation numerical method. Most types of rotor noise are examined with regards to nonlinear effects and the mechanism's significance is investigated. Moreover, new practical methods are proposed for the prediction of the magnitude of BVI noise nonlinear distortion.

2.5.2 Near field study concept and motivation

Near field propagation of air vehicle noise requires different treatment than far field. The effects which are mainly affecting it are geometrical spreading, convection and refraction effects due to the flow field, as well as reflections and diffraction on the air vehicle surfaces. A multiple direction wave propagation method is best suited for this case which can incorporate all of the aforementioned effects and can be applied to complex geometries. The mechanisms of interest for this thesis are mainly the effect of flow field (convection and refraction) and the interaction of sound with solid boundaries (reflection and diffraction) on the near field noise signatures.

For the case of jet airplane in flight, the shielding of the engine noise by the fuselage and the wing significantly affects the aircraft's transmitted noise levels and has been the research subject of many recent studies (e.g. [55]). Moreover, the engine placing on the aircraft has a direct impact on the cabin and cockpit noise levels. Taking into account that noise regulations are currently affecting the design of new aircraft, a cost effective way to determine the engine noise levels in the near field of complex geometry aircraft is needed.

Towards this objective, a new low order flow sound interaction method for adaptive hybrid grids is developed and validated. The new method is then applied to the case of a conventional airplane examining the effect of flow field and wing shielding on the near field noise levels.

2.5.3 Other studies

During the aforementioned noise investigations and analysis, some other secondary air vehicle noise results were also reached. Specifically, proof on the generation mechanism of Blade-Wake Interaction noise is provided, based on the analysis of available experimental data. A separate chapter is included at the end of this thesis describing the BWI study and its results.

3 Far Field Study: Nonlinear Propagation of Rotor Noise

In the present chapter far field propagation of helicopter noise is investigated with regards to nonlinear effects. As it has already been noted in the previous paragraphs, although helicopter rotor noise is an important part of air vehicle noise yielding notable community annoyance, it has not received significant research on its nonlinear propagation.

The purpose of this chapter is to investigate and explain the effect of nonlinear propagation on subsonic rotor noise, which has not been considered before. The aim is to show which frequency bands of the noise spectrum are affected and by how much, as well as to propose efficient prediction methods.

A research difficulty that had to be faced was that, in contrary to jet noise, there are no experimental data for rotor noise which can be used to investigate nonlinear distortion. This obstacle was overcome by using available rotor noise data from other studies and propagating them numerically using the Burgers equation. The Burgers equation was chosen due to its ability to incorporate all propagation mechanisms including nonlinear effects and be cost effective at the same time.

The present chapter is divided in three main sections. In the first section the HELISHAPE experiment and the available data which are used in this thesis are described. The second section investigates nonlinear distortion of rotor noise applying the Burgers equation to available experimental data. The effect of nonlinear distortion on the acoustic pressure waveforms and spectra is analyzed and two new nonlinear characteristics of acoustic pressure waveforms are derived. Finally, in the third section three practical prediction methods are suggested for nonlinear propagation of blade-vortex interaction noise.

3.1 The HELISHAPE experiment

Within the framework of a major European cooperative research program on rotorcraft aerodynamics and acoustics (HELISHAPE) a parametric model rotor test was conducted in 1995. The main objectives of this experimental research were to evaluate noise reduction techniques (conceptually by variation of rotor speed, dedicated tip shapes and advanced airfoils) and to validate the partners' individual aerodynamic and aeroacoustic codes.

3.1.1 Experimental setup and selected test cases

The HELISHAPE test is described in detail in [56]. The experiment was conducted in the open test section of the German-Dutch Wind Tunnel (DNW) using the MWM test rig of DLR and a highly instrumented model of a fully articulated ECF four bladed 2.1m radius rotor equipped with blades of advanced design and two exchangeable blade tips [Figure 3-1].

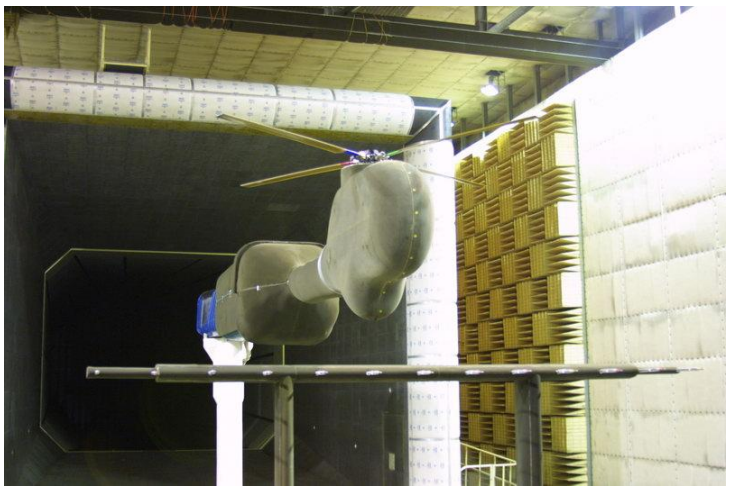

Figure 3-1: DNW setup for the HELISHAPE experiment.

The one set of blade tips (7A) was of rectangular shape, the other one (7AD) of swept-back parabolic/anhedral shape. The tests covered hover, descent, climb, low speed and intermediate speed level flight. The flight condition selected for the present

study was low speed descent flight, at 6^o descent angle for both blade tips. These test cases were performed with a rotational tip Mach number of 0.62, an advance ratio μ=0.166 (corresponding to a wind tunnel flow velocity of U_{inf}=33 m/sec) and a rotor operating speed of 970 rpm. The rotor thrust coefficient (C_T) was close to 0.069.

3.1.2 Acoustic, aerodynamic and LLS measurements

The acoustic instrumentation consisted of a linear inflow array of eleven microphones (B&K 4134) mounted on a traversing system. The microphone array's vertical position was 2.3m below the rotor hub and it moved slowly in the flow direction acquiring signals every 0.5m from 4m upstream to 2m downstream of the rotor hub. Acoustic results were thus provided on an array of 143 (13 x 11) microphone locations underneath the rotor [Figure 3-2 (a) and (b)].

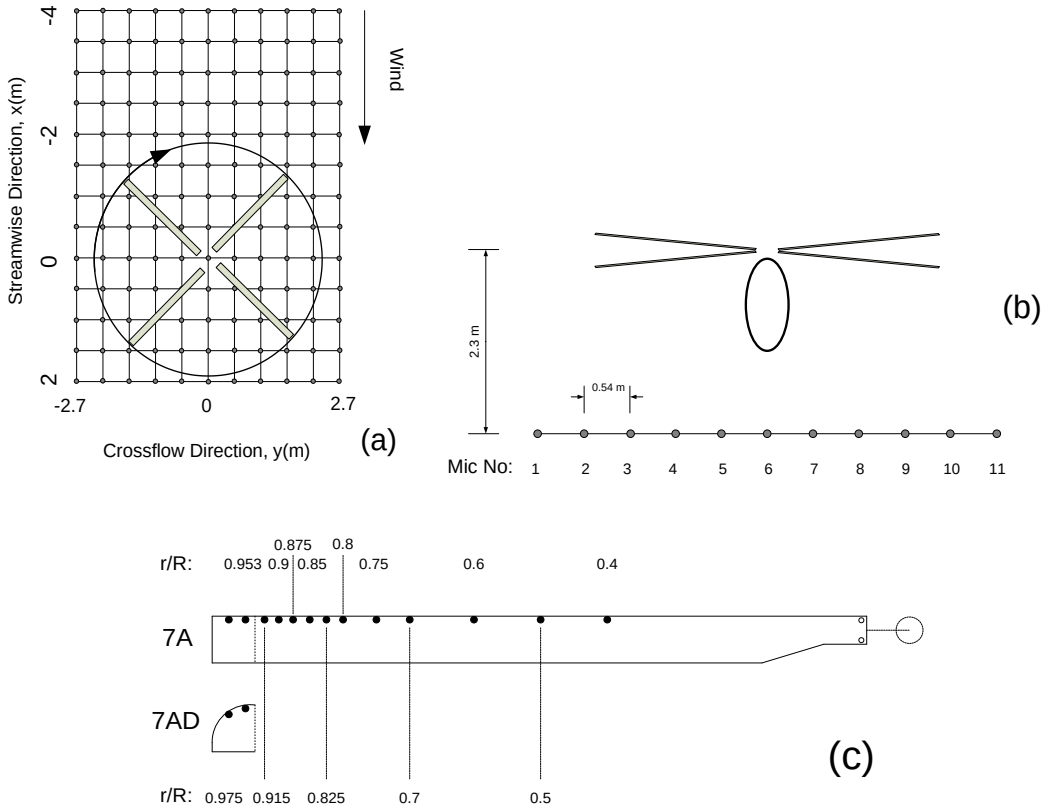

Figure 3-2: Experiment setup: top view (a), view from the back (b), and positions of pressure transducers on the rotor blades (c).

The recording of the signals was in synchronization with the rotation of the rotor shaft and the microphone signals were conditionally sampled at a rate of 2048 per revolution over a period of 30 rotor revolutions, giving a useful frequency range of about 18 kHz. For each acoustic measurement point the ensemble averaged sound pressure time histories and averaged power spectra were calculated.

For the blade pressure measurements 118 absolute pressure transducers of the piezoresistive (Kulite XCD) type were distributed on all four blades to measure the chordwise pressure distribution and the radial distribution near the leading edge [Figure 3-2 (c)]. The blade pressure signals were acquired over 60 rotor revolutions at the same rate as microphone signals and were processed similarly.

LLS flow visualisation was used to take video recorded images of cross sections at various vortex positions. These cross sections were properly seeded with oil smoke and illuminated by the laser light sheet. The vortex core centres were measured in space at several discrete sections along the vortex of interest.

3.2 Numerical Investigation of nonlinear distortion of rotor noise

In the present paragraph the Burgers equation is employed to numerically predict the evolution of noise signals, measured close to the helicopter rotor, at distances far away from the rotor. The calculations are performed twice, with and without including nonlinear effects. The difference between the calculations is a measure of the effect of nonlinear distortion. The numerical results from the present work might stimulate experimental research on the topic.

The present study does not investigate the generation of helicopter noise. The noise signals at source are considered known from available measurements, and they are considered characteristic for the flight conditions for which they were measured. For example, HSI noise [57] occurs during forward flight and is characterized by pulses of large negative pressure amplitude, while BVI [58] noise occurs mainly during descent and is characterized by pulses that contain both positive and negative pressure amplitudes. The nonlinear propagation of these signals, irrespective of the mechanism that generated them, is the focus of the present study. More specifically, a set of

measured BVI noise source signals characteristic of low-speed descent noise are analyzed. BVI noise is particularly annoying, when it occurs, and very often sets the standards of acceptance for helicopter noise; however its nonlinear propagation has not been studied before. Analysis of the available database reveals the magnitude of nonlinear propagation effects on BVI noise. It also reveals certain characteristics of the noise source signals, which can be used to qualitatively predict the nonlinear behaviour of other BVI noises (coming, for example, from different blades shapes), as well as, the nonlinear behaviour of non-BVI noise.

3.2.1 Nonlinear Propagation employing Burgers Equation

As it has already been written in the previous chapter, the augmented Burgers equation as given by Eq. (2.1) includes the effect of nonlinearity, as well as thermo-viscous attenuation, spherical spreading and atmospheric absorption. For completeness the equation is repeated below:

$$\frac{\partial p}{\partial r} = -\frac{1}{r}p + \frac{\beta}{\rho_o c_o^3} p \frac{\partial p}{\partial \tau} + \frac{\delta}{2c_o^3}\frac{\partial^2 p}{\partial \tau^2} + \sum_\nu \frac{c'_\nu}{c_o^2} \int_{-\infty}^{\tau} \frac{\partial^2 p}{\partial \tau'^2} e^{-(\tau-\tau')/t_\nu} d\tau'$$

In order to investigate nonlinear effects, Burgers equation is solved numerically in the time domain using the "Texas algorithm" described in [59] and [60]. The nonlinear term of the equation (second on the right hand side of the equation) is solved analytically, while the last two terms describing thermoviscous absorption and atmospheric relaxation are solved with finite difference methods. More specifically, the Crank-Nicolson method with standard forward-space, centred-time finite differences is used. The algorithm marches in the propagation direction and for each marching step the aforementioned mechanisms are applied sequentially. This procedure is referred to as "operator-splitting" and for sufficiently small steps the solution approaches that obtained by applying all mechanisms simultaneously. The algorithm allows the calculations to be performed by including only the effects considered at the time (spherical spreading, atmospheric absorption and/or nonlinear propagation distortion).

In the following, linear calculations shall mean the solution of Eq. (2.1) in the absence of the nonlinear term.

3.2.1.1 Accuracy of the augmented Burgers equation

The augmented Burgers equation in all its forms has been used and tested extensively for the prediction of nonlinear noise propagation [59,61]. It has also been employed specifically for the prediction of jet aircraft noise [50] and sonic boom [62] propagation in the atmosphere. In the following results obtained by Eq. (2.1) are compared with the only available experimental data for helicopter noise. The data are from Schmitz et al. [57] and regard high speed impulsive noise. Measurements were taken at two microphones positioned in the rotor plane along an imaginary line from the rotor hub directly ahead of the model rotor, the second microphone being exactly twice the distance of the first [see Figure 3-3(a)]. The ratio of the peaks (P_2 / P_1) of the two measured signals was reported as a function of the advancing tip Mach number (M_{AT}) [see Figure 3-3(b)]. It was shown that the ratio was approximately 2 for all M_{AT}, thus verifying the spherical spreading/far field hypothesis, for which the experiments were performed. However, deviations from the nominal value of 2 were observed. The deviations at low M_{AT} can be attributed to flow unsteadiness and/or experimental uncertainties, while for higher M_{AT}, and particularly above delocalization ($M_{AT} \simeq 0.9$), the difference can be explained by nonlinear propagation distortion. Table 3-1 and Figure 3-3(b) show the comparison between experimental data, linear, and nonlinear calculations. The predictions have been performed for International Standard Atmosphere (ISA) standard day with 15^{o} C temperature and 0% relative humidity, according to the wind tunnel's conditions. It can be observed that nonlinear predictions agree very well with experimental data, while linear predictions deviate from them. The energy absorbed at the shock is, therefore, responsible for the extra decay observed at high M_{AT}, which is accurately predicted by the Burgers equation.

M_{AT}	P_2 (Pa)	$P_1^{(linear)}$ (Pa)	$P_1^{(nonlinear)}$ (Pa)	$\left(\frac{P_2}{P_1}\right)^{(linear)}$	$\left(\frac{P_2}{P_1}\right)^{(nonlinear)}$	$\left(\frac{P_2}{P_1}\right)^{(measured)}$
0.902	-412.34	-205.6	-199.0	2.005	2.072	2.064
0.931	-800.04	-398.8	-363.0	2.006	2.204	2.194

Table 3-1: Comparison of results obtained by linear and nonlinear calculations [Eq.(2.1)] with experimental data (see also Figure 3-3)

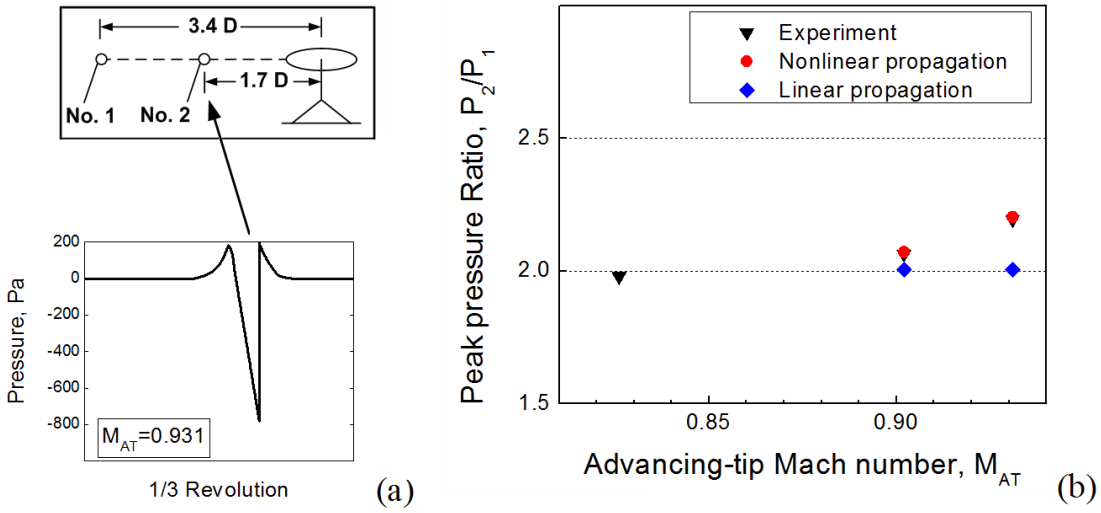

Figure 3-3: Nonlinear propagation distortion can explain differences between measurements and linear predictions; experimental data from Ref [57] for high speed impulsive noise; details of experimental setup (measurement positions and measured signal at Mic 2) [(a)]; comparisons between experimental data and numerical predictions employing Eq. (2.1) [(b)].

3.2.1.2 Application to subsonic BVI noise and related numerical issues

The application of the augmented Burgers equation to subsonic BVI noise is discussed next.

As noise source signals we considered sound pressure time signals measured during the HELISHAPE project for low-speed descent. This was one of the noisiest

flight conditions tested, where BVI noise is dominant. Measurements were conducted with a swept-back parabolic-anhedral blade tip shape.

For the purpose of the present study the following should be noted regarding the noise source signals:

i. The noise source signals stem from measurements conducted with a model rotor. Before being employed in the numerical study, they have been transformed into full scale rotor noise signals using the appropriate scaling procedure [3]. A scale factor of $\gamma = 0.34^{-1}$ has been used in the transformation. Accordingly, lengths and times have been scaled by γ. It should be noted that the low advance ratio in the experiments, $\mu = 0.165$, indicates an acceptable scalability [63,64] between model and full scale data for BVI noise, while the advancing tip Mach number, $M_{AT} = 0.724$, does not imply transonic blade effects [64].

ii. No time window has been applied to the measured noise signals. The ensemble averaged sound pressure time signal (with 30 averages) has been considered at each measurement location, not the instantaneous time signal. The signals considered do not contain high levels of broadband rotor noise, which is largely eliminated by the averaging procedure. However, propagation of instantaneous signals is also briefly examined in the present work.

iii. Throughout the study, both the measurement location and the set of calculations corresponding to that location are identified by the streamwise position of the array (x) and the microphone number. For example, Mic=6 / x=0, indicates the measurement point right underneath the rotor head center.

The noise source signals were propagated numerically by employing the augmented form of the Burgers Equation [Eq.(2.1)]. Predictions regard sound coming from a directive stationary point source located at the rotor head center and propagating distance R from the rotor head center through the microphone grid to receiver locations on the surface of a hemisphere, as shown in Figure 3-4.

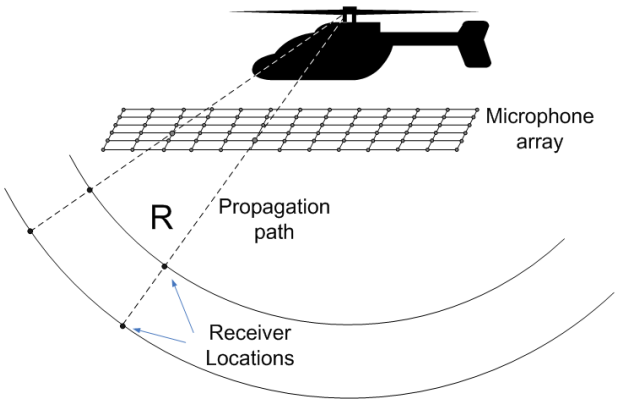

Figure 3-4: Propagation paths and receiver locations used in the present numerical investigation.

The calculations have been performed twice, once including only linear propagation effects (geometrical spreading and atmospheric absorption) and a second time adding nonlinear propagation distortion to the linear calculations. Nonlinear effects are manifested as the difference in the predicted Sound Pressure Level (SPL) values at each one-third-octave frequency band:

$$\mathrm{DSPL}(f_{1/3};R) = \mathrm{SPL}_{\mathrm{nonlinear}}(f_{1/3};R) - \mathrm{SPL}_{\mathrm{linear}}(f_{1/3};R) \qquad (3.1)$$

where R is the propagation distance and $f_{1/3}$ is the center frequency of the one-third-octave frequency bands. Positive values of DSPL indicate that nonlinear propagation distortion enhances the noise spectrum at the given frequency band.

The measured time signals had duration of one rotor revolution and were digitized with 2048 points. In the computations, however, time signals having duration of 3 rotor revolutions and 10240 points per rotor revolution were used instead, while results were obtained by analyzing the middle of the three rotor revolutions. This was done to ensure that numerical inaccuracies at the ends of the elongated time signal do not contaminate the middle part, which was actually analyzed. The time sampling increase was done by linearly interpolating additional points between the initial points of the measured signal in order to avoid excess numerical dissipation around the peak values of the signal.

3.2.2 Demonstration of the effect in BVI noise

In this section representative results obtained by the above described method for BVI noise are presented and commented. Consider the noise spectrum at source as measured at Mic 6 / x=-2.5 [see Figure 3-5(a)]. The spectrum can be subdivided into three frequency regions [5]: (i) the low frequency region, up to approximately 100 Hz (or, equivalently, up to the 5th blade passage frequency harmonic), which corresponds to thickness noise (ii) the mid frequency region, approximately from 100 Hz to 1000 Hz (or, equivalently, from the 5th to the 40th-50th blade passage frequency harmonic), which corresponds to BVI noise, and (iii) the high frequency region, from 1000 Hz to the end of the spectrum, corresponding to broadband noise. The Gol'dberg number [17] for the low and mid frequency region of the spectrum is $\Gamma \simeq 0.4 < 1$, while for the high frequency region $\Gamma \simeq 0.01 \ll 1$. It is recalled that the Gol'dberg number is a measure of the relative importance of nonlinear and absorption effects and is defined as the ratio $\Gamma = l_\alpha / \bar{x}$ between the absorption length l_α ($l_\alpha = a^{-1}$, where α is the attenuation coefficient) and the shock formation distance $\bar{x}$ of a plane sinusoidal wave in the absence of dissipation ($\bar{x} = 1/\beta\varepsilon k$, with $\varepsilon = p_0 / \rho_0 c_0^2$ being the acoustic Mach number at source and $k = \omega / c_0$ the corresponding wavenumber). The arithmetic values of the Gold'berg number have been obtained by considering characteristic values of pressure amplitude p_0, frequency f, and corresponding atmospheric coefficient α (the latter from ANSI [65]) for the different frequency regions of the spectrum.

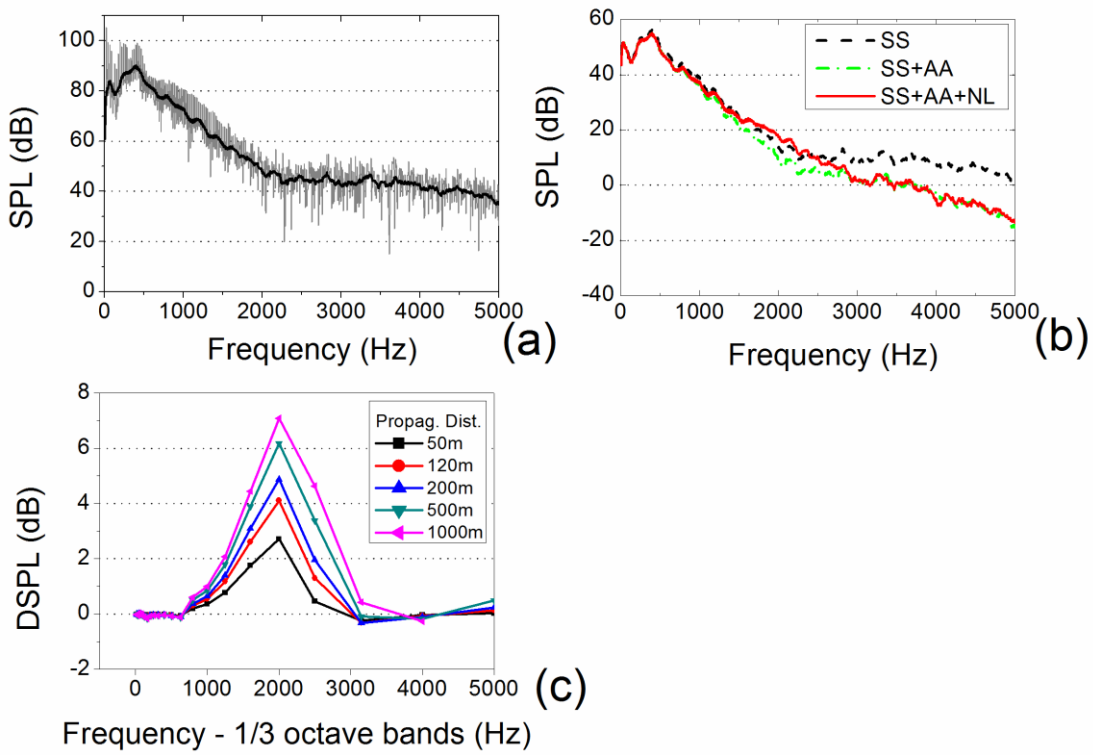

Figure 3-5: Nonlinear propagation distortion of helicopter rotor BVI noise, Mic 6 / x=-2.5; noise spectrum at source [(a)]; contribution of the various propagation mechanisms and comparison between linear and nonlinear calculations at propagation distance R=500m (SS: spherical spreading, AA: atmospheric absorption, NL: nonlinear distortion, SS+AA: linear calculations, SS+AA+NL:nonlinear calculations) [(b)]; DSPL for helicopter BVI noise at various propagation distances vs. 1/3 octave frequency bands [(c)].

Figure 3-5(b) shows the evolution of the noise spectrum for Mic 6 / x=-2.5 after $R = 500m$ of propagation. A difference between linear and nonlinear predictions can be observed in the region between 1000 Hz – 3000 Hz. The observed difference is the focus of the present study.

The behaviour depicted in Figure 3-5 (b) differs from nonlinear propagation of other noise sources, as for example, helicopter rotor in supersonic flows or jet noise, where the difference between linear and nonlinear predictions increases with increased frequency. For this case however, the nonlinearity does not contribute significantly to the amplitude of these high frequency components. This is attributed to the low amplitude mid frequency range of the source signal, which does not generate significant nonlinear harmonics to affect the high frequency end of the spectrum.

Figure 3-5 (b) also demonstrates the relative significance of the various propagation effects involved, namely spherical spreading, atmospheric absorption, and nonlinear propagation distortion. Spherical spreading is the mechanism that mainly determines the evolution of the noise spectrum. Nonlinear distortion is less important than spherical spreading, but equally important as atmospheric absorption. Atmospheric absorption [65] is routinely added to geometrical spreading to improve the accuracy of the predictions. It is the authors' opinion that nonlinear distortion should also be included.

Finally, Figure 3-5(c) shows the DSPL vs. one-third-octave frequency bands for Mic 6 / x=-2.5 at various propagation distances. It can be observed that DSPL increases with increased distance and that the magnitude of DSPL is sizeable and in some cases it can be as large as 7 dB.

3.2.3 Polarity as a nonlinear characteristic of BVI signals

In the following it is investigated how certain characteristics of BVI pulses at source relate to their nonlinear propagation distortion. For a detailed description of BVI noise signals the reader is referred to Schmitz [3] and Yu [58].

Figure 3-6 (a) shows two signals, one typical of advancing side BVI (Mic 3 / x=0) and one of retreating side (Mic 11 / x=2). The characteristic BVI pulses have predominantly positive pressure amplitudes in the advancing side and predominantly negative in the retreating side. This change of sign is attributed to the opposite rotational directions of the vortices during blade vortex interaction on the advancing and retreating side. In the advancing side, the small negative part of the pulse comes before the large positive part, while the opposite is true for the retreating side. Also, due to geometrical considerations, the non-BVI noise between the blade passages comes, in general, after the BVI pulse in the advancing side, while before the BVI pulse in the retreating side. Finally, in most cases multiple pulses at each blade passage in the advancing side are observed, as opposed to the single pulse at each blade passage in the retreating side.

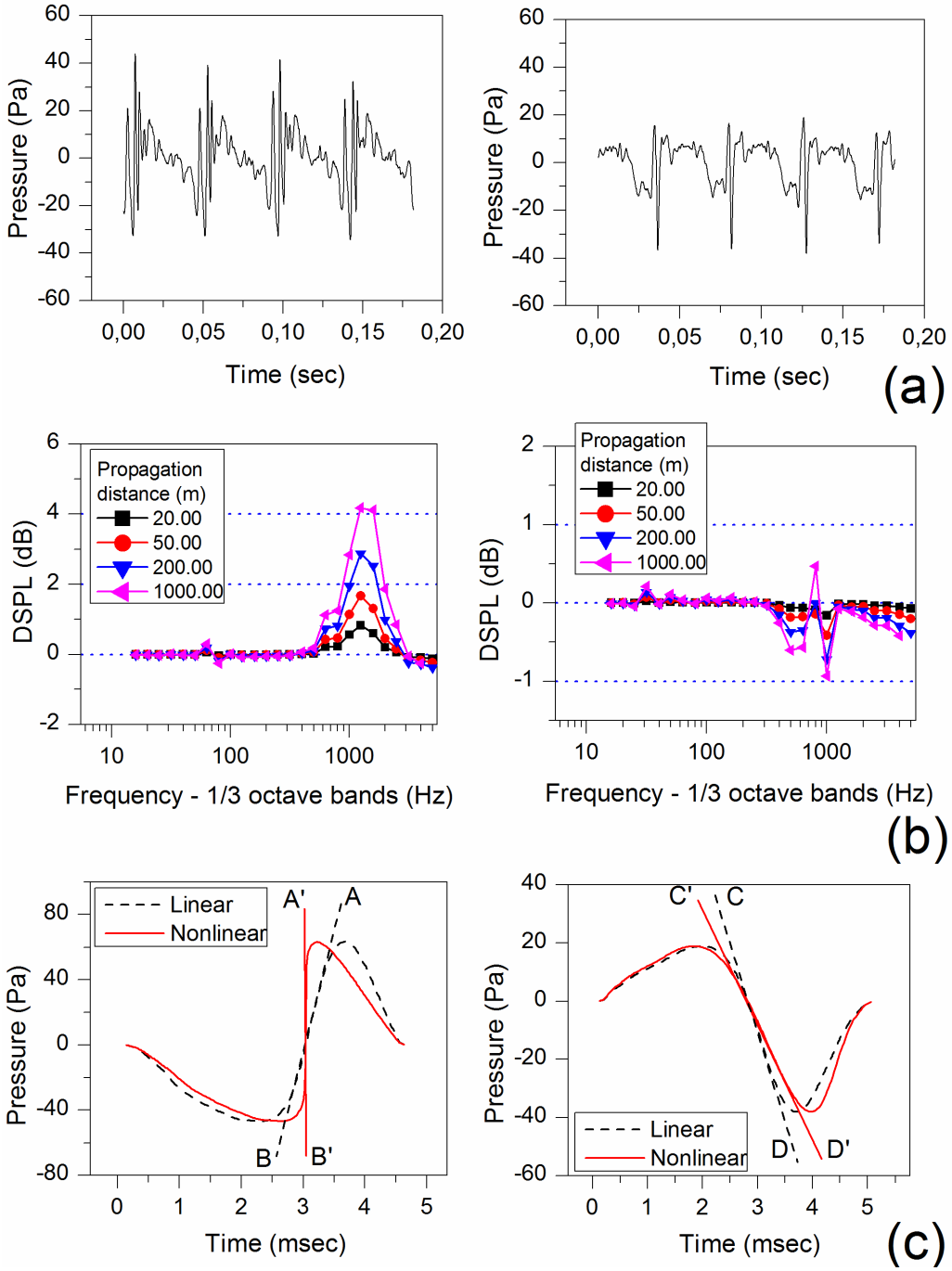

Figure 3-6: Advancing side BVI (left column) and retreating side BVI (right column): signals at source [(a)]; their DSPL at various propagation distances [(b)]; nonlinear evolution (geometrical spreading and atmospheric absorption ignored) of main BVI pulses isolated from the signals at source [(c)].

The evolution of two signals yields the DPSL shown in Figure 3-6 (b). All BVI source signals of the database evolve either as an advancing side type signal, yielding

the characteristic DSPL bell, or as a retreating side type signal. The following differences between the two types are common in all receiver locations:

(i) the magnitude of DSPL in the advancing side is substantially larger than in the retreating side;

(ii) DSPL values are predominantly positive in the advancing side, while predominantly negative in the retreating side;

(iii) the frequencies mainly affected in the advancing side are the frequencies in the octave bands of 1000 Hz and 2000 Hz, while the frequencies mainly affected in the retreating side are frequencies from 300 Hz to 1000 Hz; and

(iv) although very small in magnitude, DSPL in the lowest frequency bands, up to 300 Hz, are negative in the advancing side, while positive in the retreating side.

The magnitude of DSPL in the retreating side is so small that it can be considered zero for all practical purposes. However, as will be shown in this section, the negligible DSPL values on the retreating side should not be considered as a limiting case of advancing side type nonlinear evolution, but as a different type of evolution.

The difference in the nonlinear evolution between advancing and retreating side BVI signals can be explained by observing the evolution of their main pulses, which have been isolated from the two signals and shown in Figure 3-6 (c). In order to clearly show the effect, only nonlinear distortion was considered. It can be observed that the segment of the signal connecting the peak with the trough steepens due to nonlinear propagation in the advancing side, while it "un-steepens" in the retreating side. Since in the advancing side BVI pulse, the small negative part of the pulse comes before the large positive part, the segment of the pulse between peak and trough will always have a positive pressure gradient and will steepen during propagation. Correspondingly, in the retreating side it will have a negative pressure gradient and will "un-steepen".

Consider the straight lines passing through points AB ($p_{(adv)}(0,t) = m_a t,\ m_a > 0$) and CD ($p_{(ret)}(0,t) = -m_r t,\ m_r > 0$) in the advancing and retreating side source signals, respectively, as shown in Figure 3-6 (c). For plane wave propagation in a non-dissipative fluid the governing equation is

$p_t + c_0 p_x = \beta / \rho_0 c_0^2 \, p p_t$ and the general solution is $p(x,t) = f\left(t - \frac{x}{c_0} + \frac{\beta x p}{\rho_0 c_0^3}\right)$, where $f(t) = p(0,t)$ [17]. For the advancing side and retreating side, respectively, the solution becomes:

$$p_{(adv)} = \frac{m_a}{1 - \frac{\beta m_a x}{\rho_0 c_0^3}} \tau = \frac{m_a}{1 - \frac{x}{\bar{x}_a}} \tau = A_{(adv)} \tau, \quad \tau = t - \frac{x}{c_0}, \; \bar{x}_a = \frac{\rho_0 c_0^3}{\beta m_a} \qquad (3.2)$$

$$p_{(ret)} = \frac{-m_r}{1 + \frac{\beta m_r x}{\rho_0 c_0^3}} \tau = \frac{-m_r}{1 + \frac{x}{\bar{x}_r}} \tau = A_{(ret)} \tau, \quad \tau = t - \frac{x}{c_0}, \; \bar{x}_r = \frac{\rho_0 c_0^3}{\beta m_r} \qquad (3.3)$$

The above solutions indicate straight lines with inclinations angles $A_{(adv)}, A_{(ret)}$ that change with propagation distance. The tendency of $p_{(adv)}$ is to steepen until a shock is formed (at $x = \bar{x}_a$), while of $p_{(ret)}$ to un-steepen and no shock will ever be formed at that segment of the waveform. In the frequency domain, the former is associated with generation of higher frequencies and depletion of lower frequencies, while the latter with generation of lower frequencies and depletion of higher frequencies. It should be noted that $A_{(adv)} = \partial p_{(adv)} / \partial \tau > 0$ increases with increased propagation distance x ($x < \bar{x}_a$) until $A_{(adv)}$ becomes infinite at $x = \bar{x}_a$. Also $A_{(ret)} = \partial p_{(ret)} / \partial \tau < 0$ increases with propagation distance until it becomes zero for very long propagation distances. Pulses idealized as being made up from segments of straight lines of varying inclination angles $A \propto \partial p / \partial t$ tend to transfer energy to higher or lower frequencies depending on which tendency is overall prevailing in the entire time waveform. This tendency can be quantified by taking into account the value of the pressure gradient $A \propto \partial p / \partial t$ of each segment weighted by the local pressure amplitude.

A new quantity has been derived that provides an indicator of the tendency of the BVI signal to "steepen" and thus follow an advancing side type nonlinear evolution or "un-steepen" and thus follow a retreating side type nonlinear evolution. The quantity is termed polarity (Π) and is defined as follows:

$$\Pi^3 = \frac{\sum_{i=2}^{N}\left(P_i^+ \cdot \Delta P_i^+\right)^2}{N^+} - \frac{\sum_{i=2}^{N}\left(P_i^- \cdot \Delta P_i^-\right)^2}{N^-} \tag{3.4}$$

where N is the number of points in the digitized time signal, P_i is the value of the pressure at point i, $\Delta P_i = P_i - P_{i-1}$, P_i^+ is the pressure at point i, when $\Delta P_i > 0$ ($\Delta P_i = \Delta P_i^+$), P_i^- is the pressure at point i when $\Delta P_i < 0$ ($\Delta P_i = \Delta P_i^-$), N^+ is the number of points for which $\Delta P_i > 0$, and N^- is the number of points for which $\Delta P_i < 0$. According to Eq.(3.4), the main pulse of the advancing side BVI signal has positive polarity, while the main pulse of the retreating side BVI negative. Polarity can be used to characterize signals with mixed advancing and retreating side characteristics as either advancing or retreating. Figure 3-7 shows the polarity of all source signals. As far as nonlinear distortion is concerned, visual observation of all DSPL plots reveals that source signals with negative polarity exhibit a retreating side type DSPL, while source signals with positive polarity the characteristic advancing side DSPL bell. It should be further noted that the absolute value of polarity increases for signals with a strong content in advancing or retreating BVI noise. The polarity contours, therefore, resemble to traditional medium-frequency contours used to define advancing and retreating BVI regions of rotors in descending flight [5].

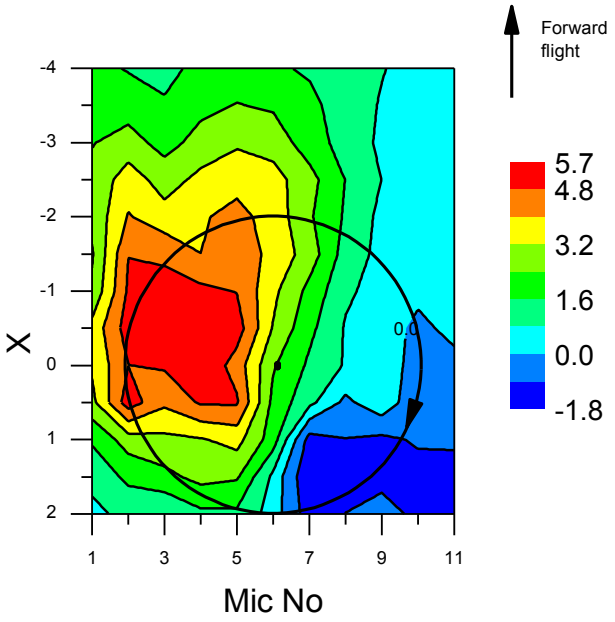

Figure 3-7: Contour plots of polarity of all noise source signals on a plane underneath the rotor. Negative polarity corresponds to retreating side type nonlinear evolution, positive polarity to advancing side type nonlinear evolution.

It should be noted that the polarity as defined in the present work is particularly helpful for BVI pulses, as it predicts both the nonlinear evolution type of the pulse and the strong advancing BVI regions. If it is to be used for other noise source types, a different weighing might be more appropriate depending on the characteristics of the given noise source type. In any case it should be applied in the pre-shock region and only the sign of Π should be considered. Its arithmetic value might not be significant for the problem at hand. It should be emphasized that, as discussed for $A_{(adv)}$ and $A_{(ret)}$, the value of polarity Π changes with propagation distance and may change sign. An initially positive Π shall continue to be positive, while an initially negative Π might become positive during propagation. Thus, although the sign of Π at any distance (before shock formation) is indicative of the nonlinear evolution in the immediately next propagation steps, its negative sign at source is indicative only for relatively weak waves (like the ones handled here), where no drastic changes in the waveform take place.

3.2.4 Weighted rise time as a nonlinear characteristic of BVI signals

Noise source signals on the advancing side vary considerably in shape. They range from signals with multiple, less impulsive peaks at each blade passage (see signal A in Figure 3-8) to signals containing a single, very impulsive peak at each blade passage (see signal B in Figure 3-8). The corresponding DSPL bell moves to higher frequencies, as the signal transitions from one category to the other (see Figure 3-8).

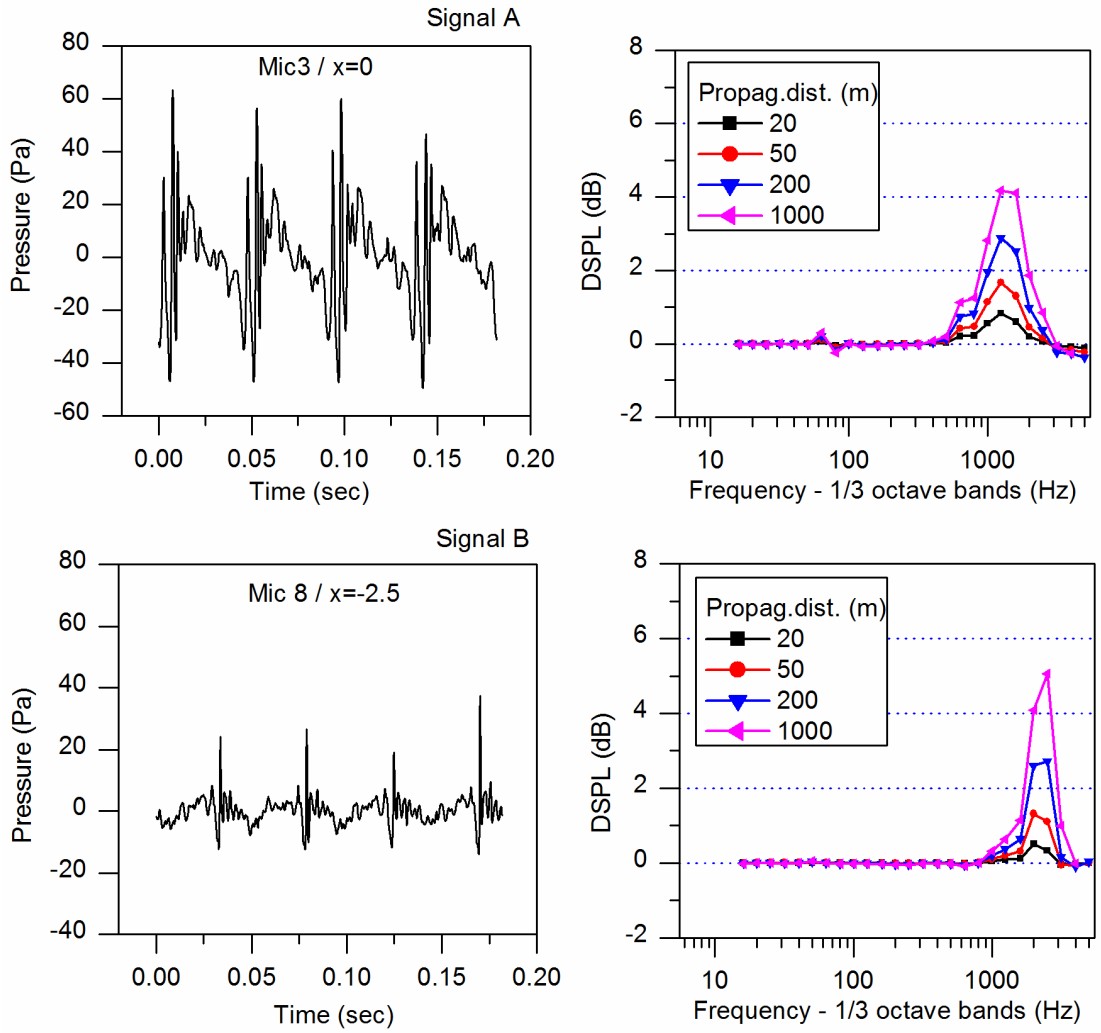

Figure 3-8: Pressure signals at source vary from containing multiple less impulsive BVI pulses to containing a single very impulsive BVI pulse (left column); corresponding DSPL plots- DSPL bells shift towards higher frequencies (right column).

Signals A and B differ not only in the number of intense BVI peaks within each blade passage but also in the non-BVI noise between blade passages. Numerical experimentation showed that the shift of the DSPL bell towards higher frequencies cannot be explained by either of these differences. Further numerical experimentation showed that the starting frequency of the DSPL bell (f_{start}) is related to the rise time of the main BVI pulse. Rise time (DT) is the time from the trough to the peak of the main BVI pulse [see Figure 3-9(a)]. The duration of the pulse, also called emission time (T), does not seem to directly affect f_{start} .

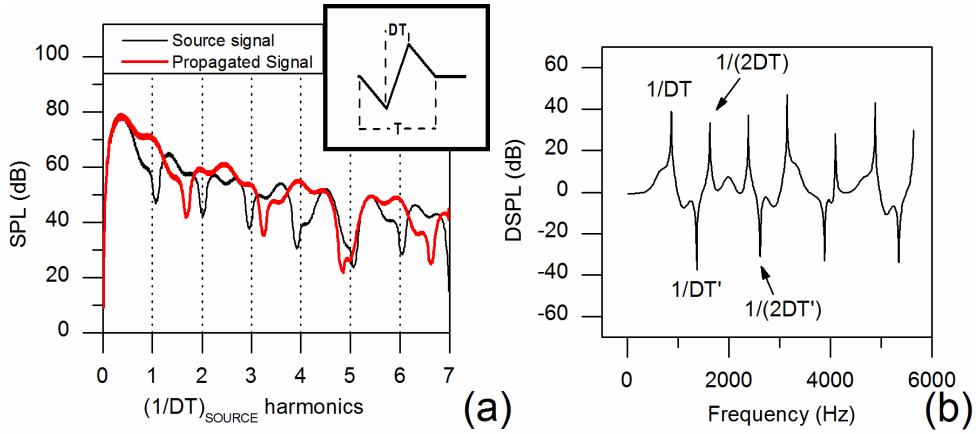

Figure 3-9: Spectrum of a BVI signal idealized as a train of N-shaped pulses, at source and after 150m of propagation (nonlinear effects only) [(a)]; corresponding DSPL plot [(b)].

In the past, the emission time has been employed to analyze the spectral characteristics of BVI signals [66]. For the purposes of the present study, the rise time seems to be a more appropriate parameter. Consider a BVI signal idealized as a train of N-shaped pulses with $DT < T/2$. Firstly, the local minima in the corresponding spectrum occur at the rise frequency harmonics $(1/DT, 1/2DT, ...)$, not the emission frequency harmonics $(1/T, 1/2T, ...)$ [see Figure 3-9(a)]. Furthermore, as the signal undergoes nonlinear distortion, the rise time of each pulse decreases ($DT' < DT$), while the emission time remains the same. As a result, the local minima in the spectrum occur again at the rise frequency harmonics of the propagated signal $(1/DT', 1/2DT'...)$, which have been displaced to higher frequencies compared to the

rise frequency harmonics of the source signal ($1/DT, 1/2DT, ...$) [see Figure 3-9(a)]. Finally, ignoring spherical spreading and absorption, DSPL is obtained as the difference between the spectra at source and after some propagation as shown in Figure 3-9(b). It can be observed that the frequency, where nonlinear effects start to appear f_{start}, is approximately $1/DT$.

For the actual rotor BVI signals the analysis is more complex, as multiple, different, non-ideal BVI pulses are contained in the pressure time signal. As a predictor of f_{start}, therefore, a weighted rise time is proposed that takes into account the rise time, of all pulses in the signal. The weighted rise time (DT_W) is defined as follows:

$$DT_W = \frac{\sum_{i=1}^{n} DT_i \times DP_i^4}{\sum_{i=1}^{n} DP_i^4} \tag{3.5}$$

where n is the number of pulses in the pressure time signal, DT_i is the rise time of the i-th pulse and $DP_i = P_{\max,i} + \left|P_{\min,i}\right|$ of the i-th pulse. Figure 3-10(a) and Figure 3-10 (b) show the weighted rise frequency ($1/DT_W$) of all source signals and the f_{start} of their corresponding DSPL bell. It can be observed that $1/DT_W$ can predict the areas, where f_{start} has large values, and also the approximate value of f_{start}. For example, in the region located upwind and on the retreating side of the rotor f_{start} has its largest value and, accordingly, nonlinear distortion affects only the high frequencies. On the opposite side, in the region downwind and on the advancing side, nonlinear effects kick in at lower frequencies. Finally, the correlation plot of $1/DT_W$ and f_{start} indicates that $f_{start} \simeq 1/DT_W$ [Figure 3-10(c)].

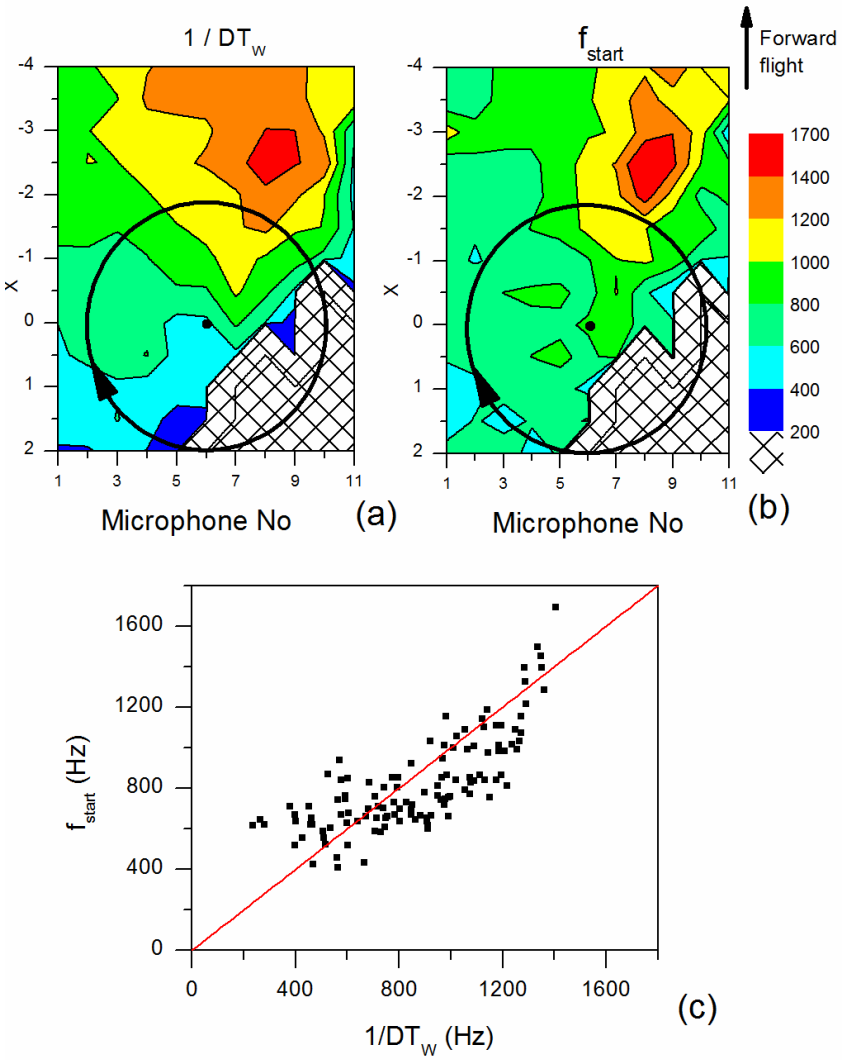

Figure 3-10: Contours of weighted rise frequency ($1/DT_w$) of all noise source signals on a plane underneath the rotor [(a)]; f_{start} of the corresponding DSPL bells after 120m of propagation [(b)]; correlation between $1/DT_W$ at source and f_{start} after 120m of propagation [(c)].

It should be noted that f_{start} relates only to nonlinear effects, while $1/DT_W$ is both a predictor for f_{start} and also of measure of impulsiveness of the source signal (where in the present context impulsiveness should be understood in terms of rise time). The contour plot of $1/DT_W$ indicates the areas of impulsive signals irrespective of their subsequent nonlinear evolution. The specific weighting used in the definition of $f_{start} \simeq 1/DT_W$ is specific to the signals at hand. A different weighting might be appropriate for signals of different type. Although the suitability of $1/DT_W$ to predict

the arithmetic value of f_{start} depends on the specific weighting, $1/DT_W$ can be used in any case to compare two signals with regards to their impulsiveness (keeping in mind that $1/DT_W$ has been derived for signals with positive polarity and in the pre-shock region).

3.2.5 Nonlinear propagation and testing of nonlinear characteristics for other rotor noise signals

The nonlinear characteristics derived for BVI signals are tested for other signals in the following paragraphs. More specifically they are applied to a second BVI database retrieved from a rectangular blade tip, instantaneous BVI signals containing significant levels of broadband noise, as well as thickness and high-speed impulsive noise signals.

3.2.5.1 BVI noise from a rectangular blade tip

The blade tip shape changes the shed vortex that interacts with the succeeding blade to generate the BVI pulse. This changes the BVI signal at source, and thus its nonlinear evolution. To investigate the effect, a second set of measurements, also taken during the HELISHAPE project, was analyzed. The flight conditions and the measurement points were the same, but a rotor with a rectangular blade tip was used instead of the swept blade tip. An extended numerical analysis, similar to that of the measurements below the swept tip blade, verified similar DSPL values and frequency bands affected. Furthermore, the polarity of the source signal as a predictor for the nonlinear evolution type (advancing vs. retreating), as well as, the relation between weighted rise frequency ($1/DT_W$) and f_{start} are shown to hold for the rectangular tip as well [Figure 3-11(a) and (b)]. Figure 3-11(a) shows an area on the retreating side with positive polarity. Indeed, signals measured in that area evolve following more the advancing side type than the retreating side type.

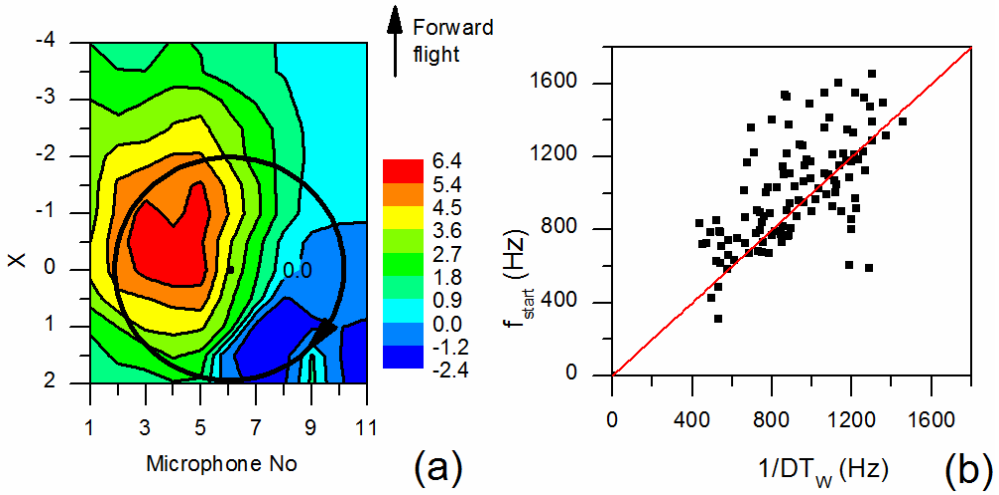

Figure 3-11: Rectangular tip blade: polarity contour of all noise source signals on a plane underneath the rotor[(a)]; correlation between f_{start} of all noise signals after 120m of propagation and weighted rise frequency ($1/DT_W$) of all signals at source [(b)].

3.2.5.2 Instantaneous BVI signals containing broadband noise

BVI noise is unsteady in nature and instantaneous BVI noise signals can be significantly different than averaged noise signals. The environment in the DNW tunnel, however, was very steady and averaged noise signals do not differ drastically from instantaneous. The main difference between them is the higher values at the broadband frequency region of the spectrum in the latter case. In general, the averaging procedure broadens the BVI pulse and lowers the peak to trough pressure amplitude [67]. It further eliminates the pressure fluctuations on the main BVI pulse and also the broadband noise, which in the time signal appears as small pulses immediately after the BVI pulses at each blade passage. As a result, the high frequency region of the power spectrum has higher values, by up to 10dB, in the case of instantaneous signals. In terms of the Gol'dberg number Γ the broadband frequency region is not as weak as in the case of the averaged signals. Consequently, the power spectrum of the instantaneous signal after propagation has a stronger high frequency component than the power spectrum of the averaged signal and DSPL extends to higher frequencies [Figure 3-12(a)]. The magnitude of DSPL, however, is more pronounced in the averaged signal. An extended

numerical investigation of the instantaneous source signals verified the above differences in DSPL, as well as, the suitability of polarity Π and weighted rise frequency $1/DT_W$ as predictors for the nonlinear evolution type and f_{start}, respectively. As expected, the polarity contours are the same for both averaged and instantaneous signals, as the blade vortex interaction mechanism remains the same, while the higher values of $1/DT_W$ and f_{start} in the instantaneous signals [compare Figure 3-11(b) and Figure 3-12(b)] are in line with the fact that averaged signals are less impulsive due to the averaging procedure outlined before.

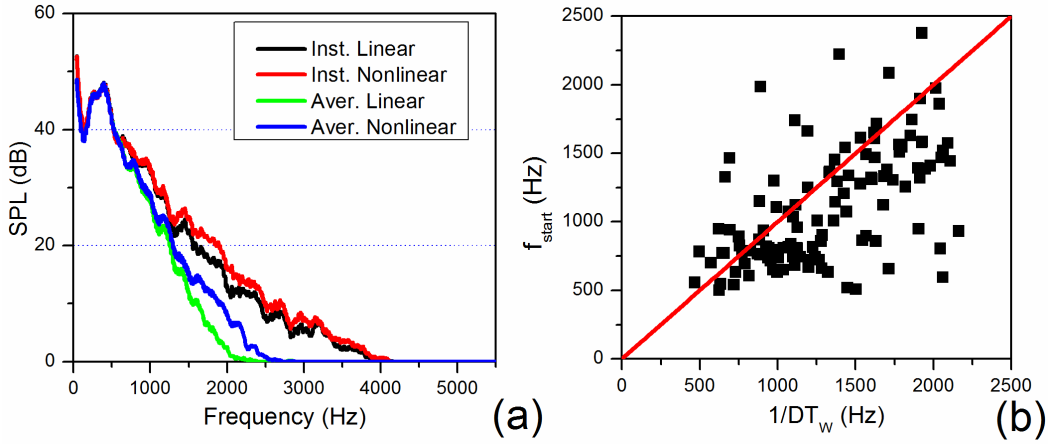

Figure 3-12: Instantaneous BVI noise signals: Comparison of spectra of averaged and instantaneous BVI noise signal after 1000m of propagation for Mic 6 /x=-2.5 [(a)]; correlation between f_{start} of all noise signals after 120m of propagation and weighted rise frequency ($1/DT_W$) of all signals at source [(b)].

3.2.5.3 Other non-BVI rotor noise

Cases of non-BVI noise are briefly examined next. Specifically, the cases of thickness noise and High Speed Impulsive (HSI) noise, with and without shocks, are considered.

Thickness noise is caused by the displacement of the air by the rotor blades and depends on the blade thickness distribution and the advancing tip Mach number (M_{AT}). Thickness noise is characterized by symmetrical negative pulses. As M_{AT} increases, the negative pulse grows dramatically in amplitude and dominates the time

signal but no shocks are formed. As M_{AT} increases further (above delocalization), a strong signal of very large amplitude is produced and shocks are formed. The left column of Figure 3-13 shows this transition for increasing M_{AT} (albeit measured for different blades and flight conditions). Thickness noise (combined with BVI noise) is depicted on the first row, HSI noise without shocks on the second, and HSI noise with shocks on the third row. The reader is referred to Ref. [57] for a detailed description of HSI noise.

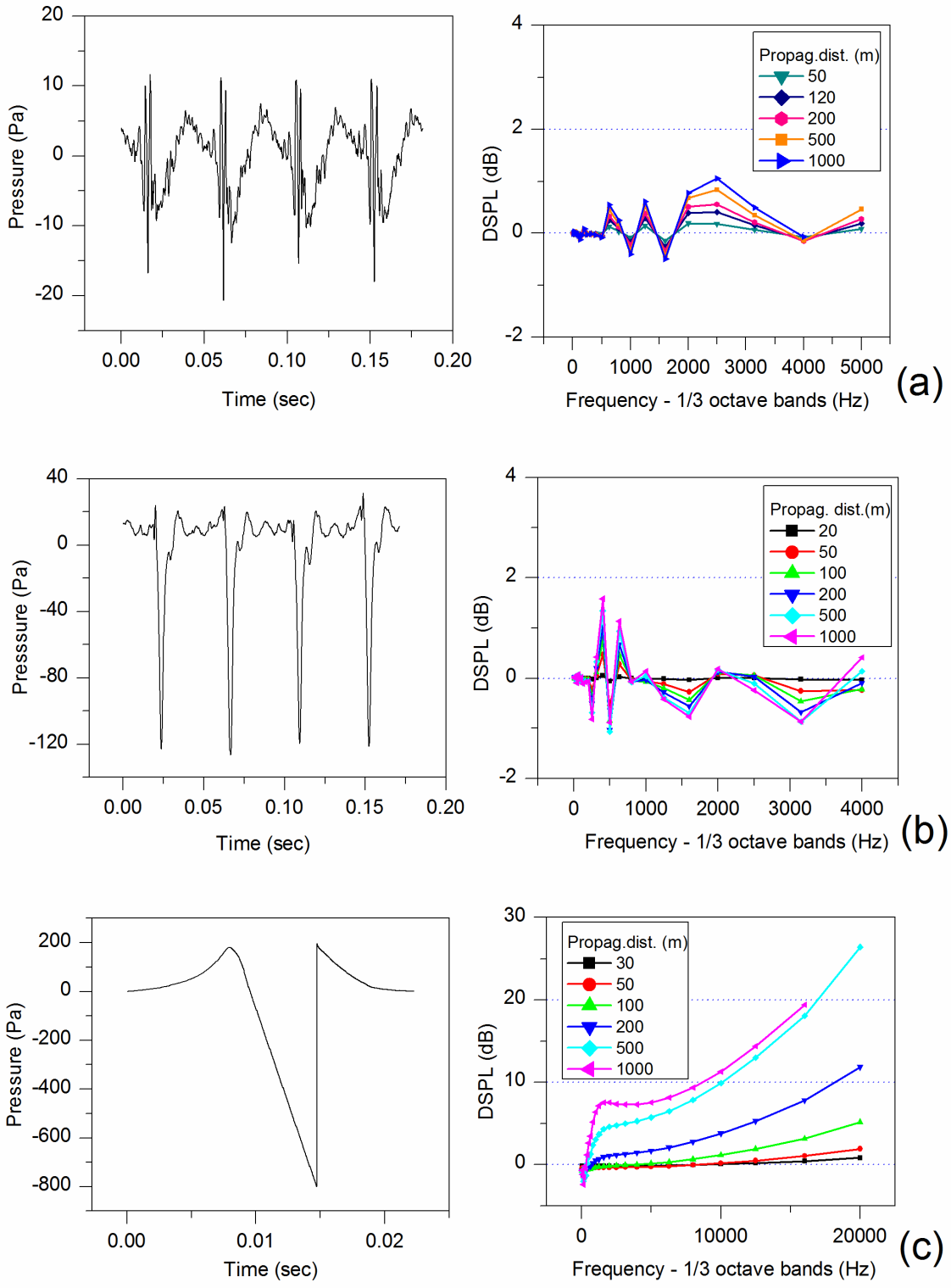

Figure 3-13: Non-BVI noise: Pressure time signals at source (left column) and corresponding DSPL plots (right column); Line (a): Thickness noise combined with BVI noise, M_{AT}=0.720 (signal taken during descent on the rotor plane 21.9m from rotor head center [56]); Line (b): HSI noise, M_{AT}=0.881, shock-free (taken for lifting forward flight below a four-bladed rotor [68]); Line (c):

HSI noise, M_{AT} =0.931, with shock (taken for lifting forward flight on the rotor plane of a two-bladed rotor [57]).

The corresponding DSPL is shown on the right column. The following can be noted:

(i) When shocks are present in the signal (this being the only case that has been considered in the past), the magnitude of DSPL becomes very large. The magnitude is significantly larger than in the BVI cases considered in the previous sections, or in the case of shock-free HSI noise also shown in of Figure 3-13.

(ii) The polarity predicts the evolution type of these non-BVI signals correctly. The polarity of the thickness noise signal and of the HSI noise after delocalization is positive. Accordingly, DSPL resembles the advancing side type. The polarity of the shock-free HSI signal is negative and DSPL resembles the retreating side type. The latter also explains the small magnitude of DSPL despite the large negative amplitude of the noise source signal.

(iii) The weighted rise frequency can be applied only for the thickness noise signal (the other two signals have either negative polarity or contain shocks). Where applicable, however, the weighted rise frequency predicts f_{start} correctly.

3.3 Practical Prediction methods

The employment of BE for the numerical prediction has two main difficulties: (i) it can be time consuming to be included in routine calculations, as for example, in optimization of noise abatement procedures; and (ii) it requires knowledge of the initial pressure time signal, as the power spectrum alone (which is usually known) is not sufficient. In the following three approaches are presented to address these concerns.

These approaches provide an estimate of the magnitude of the nonlinear effects, as well as, of the frequency bands it affects. They can, therefore, be of use to the ever

increasing need to improve the accuracy of helicopter noise prediction tools. Particularly so in studies, where the result sought is the detailed frequency distribution of the energy at the receiver location, rather than a metric comprising all frequencies, such as the overall sound pressure level. Consider, for example, a noise acceptance study, where noise levels produced by a helicopter at a receiver away from it, are evaluated with emphasis placed at the 1000 Hz and 2000Hz octave frequency bands levels, where the human ear is most sensitive.

However, prediction of nonlinear effects presents two difficulties compared to prediction of other propagation effects, such as, spherical spreading and atmospheric absorption. In routine calculations, spherical spreading can be accounted for by simply subtracting 6dB from the level of each one-third octave frequency band for each distance doubling, while atmospheric absorption by subtracting tabulated values in international standards [69]. Similar tabulated values for nonlinear effects do not exist. Recall that nonlinear distortion depends on the initial source signal, that it is counter-acted by other effects during propagation, and that frequencies in the spectrum interact with each other. Specifically for BVI noise, where the source signal depends largely on the flight condition parameters, tabulated values for the general case cannot be produced. In the present work, a numerically generated database is presented which considers this problem and yields corrections for nonlinearity (in dB for each one-third octave band) for the specific case of low speed descent, when only the receiver location is known. Furthermore, correlations between the corrections for nonlinearity and various signal characteristics at the source are presented, which can be used to determine if the effect is large enough to require a precise prediction.

The second difficulty is presented by the fact that the time history of the noise signal at source is needed for the prediction of its waveform distortion. The power spectrum of the noise source, which is traditionally used to describe the noise field produced by a helicopter, is not sufficient. For the case that a precise computation of nonlinear effects is needed, but the phase information at source is missing, a phase-assignment method is presented that allows the prediction of nonlinear effects even when the phase information at source is missing.

3.3.1 Numerically generated database

To address the concern regarding the complexity of the nonlinear calculations, a numerically generated database has been created specifically for BVI noise. Measurements, (ensemble averaged pressure time histories) from the HELISHAPE experiment for low speed descent flight, have been used as noise source signals and their nonlinear evolution has been stored in the database.

Measurements were made at an array of 11 equally spaced microphones [see Figure 3-14(a)] with the array's span positioned normal to the flow, symmetrically arranged with respect to the rotor center, and at several streamwise locations of the array's span [56].

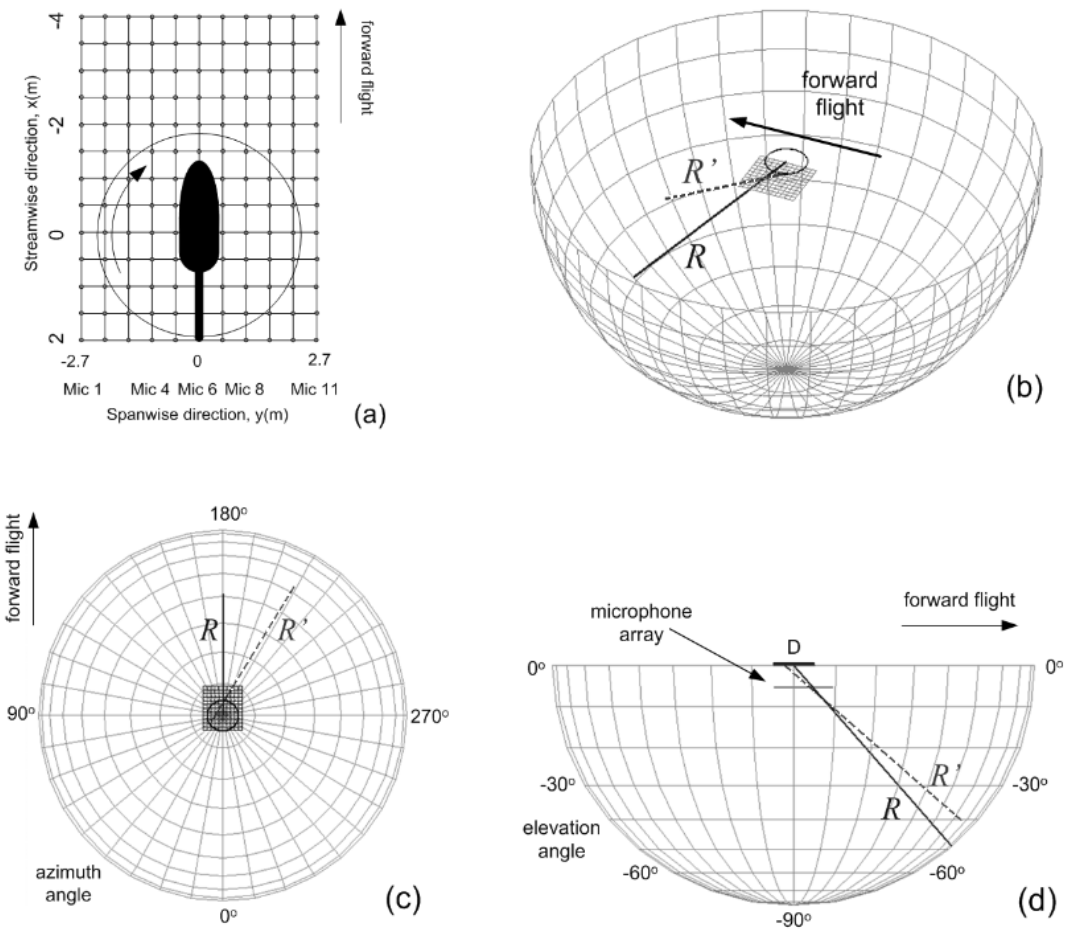

Figure 3-14: Measurements positions in HELISHAPE experiment [(a)]; propagation paths in numerical calculations: perspective view [(b)], top view [(c)], side view [(d)]; propagation path *R* (*R*>>*D*) in the initial numerical calculations, source at the rotor hub, results on hemispherical

surfaces that move with the helicopter; results identified with microphone number and streamwise position of microphone array; propagation path *R'* (*R'*≈ *R*) in the updated calculations corrected for BVI far field directivity, source for advancing side BVI at 0.9 radius on the rotor disk and 60 deg azimuth angle, receivers on hemispherical surfaces that move with the helicopter, receivers identified by *R'*≈ *R*, elevation angle and azimuth angle.

The noise signals measured on the microphone grid were considered as noise source signals coming from a directive stationary point source located at the rotor center and with source radius equal to the distance from the rotor center to the given microphone position. The noise signals were first transformed into full scale data [3] in order to match the frequency regions of a real helicopter rotor, and were subsequently propagated numerically distance R following the propagation path from the rotor head center through the microphone grid to receiver locations on the surface of a hemisphere that follows the helicopter, as shown in Figure 3-14(b). The calculations have been performed employing Eq.(2.1) twice, once including only linear propagation effects (geometrical spreading and atmospheric absorption) and a second time adding nonlinear propagation distortion to the linear calculations. In the following, the propagation distance R from the rotor head center to the receiver, the microphone number and the streamwise position of the microphone array (for example Mic 6/ x=0) will indicate the set of measurements performed using as noise source signal the signal measured at the position identified by its streamwise position and microphone number.

The database provides the difference in the SPL value (DSPL) as given by Eq. (3.1). Data are provided at 143 points on a hemisphere and for 18 different hemisphere radii ranging from 20m to 1.5km - a total of 143x18=2574 receiver locations. The numerically generated database has been integrated into HELENA, a computational tool synthesized under the integrated European project FRIENDCOPTER. Example results from the numerically generated database are those shown in Figure 3-6 (b) for Mic 3 / x=0 (on the advancing side) and for Mic 11 / x=2 (on the retreating side).

As it has been shown in the previous paragraphs, nonlinear propagation distortion effects depend on the characteristics of the main BVI pulse in the source signal measured close to the rotor. It was further shown that the nonlinear propagation evolution can be categorized either as advancing side type or as retreating side type, depending on the polarity of the source signal. At the majority of the receiver locations

nonlinear distortion is of the advancing side type (positive polarity) yielding the characteristic bell shape in the DSPL plot with sizeable DSPL values, while the retreating side type (negative polarity) yields negligible DSPL values [see Figure 3-6 (b)]. The advancing side type nonlinear evolution has the following characteristics:

1) DSPL values are predominantly positive (in other words linear calculations under-predict the noise spectrum away from the rotor),

2) the octave frequency bands affected are the bands centered at 1000 Hz and 2000 Hz, to which the human ear is most sensitive, and

3) the DSPL values increase with increasing propagation distance, until the SPL values diminish themselves with propagation distance, mainly by spherical spreading, and cannot longer be heard.

It is noted that the bell shape of the DSPL plot is attributed to the fact that the noise spectrum at source is relatively weak with most of its energy at low frequencies and a very small high frequency component. The low frequency end of the spectrum undergoes a weak distortion (higher harmonics are generated affecting the immediately higher frequencies). On the other hand, the very low noise levels at the high frequency end of the spectrum, further reduced by spherical spreading, become so low that no distortion takes place at this part of the spectrum, nor is the high frequency end of the spectrum affected by the stronger, but still weak, low frequency part. The DSPL bell can be thought of as depicting the distortion generated by the stronger low frequency end of the spectrum, while at the high frequency end any difference between linear and nonlinear propagation is negligible.

In the present work emphasis is placed on the prediction of DSPL, both with regards to the maximum values it obtains and to the areas around the helicopter at which these maxima occur. Figure 3-15 shows the DSPL predicted after 120 m of propagation (R=120m) for the one-third-octave frequency bands centered at 1250Hz, 1600Hz, 2000Hz, and 2500Hz. The axes indicate the position on the measurement plane (microphone number and streamwise position of the microphone array) to which the calculated DSPL corresponds. It can be observed that not all source signals on the measurement plane undergo the same nonlinear distortion and DSPL depends strongly on the location of the measured source signals on the measurement plane. The one-third-octave frequency bands of 1600 Hz and 2000 Hz are mostly affected. The

maximum values of DSPL at each one of the one-third-octave frequency bands occur at slightly different areas, which move clockwise from the 1250Hz to the 2500 Hz frequency bands. This is in line with the previous paragraph which has shown that the DSPL bell moves to higher frequency, as the rise time of the main BVI pulse becomes shorter. (Rise time is the time in the main BVI pulse from trough to peak). Moving from the advancing downwind side to the upwind and forward positions, the rise time of the main BVI pulse indeed becomes shorter, and, thus, the frequency where $DSPL_{max}$ occurs becomes higher. Finally, it is noted that the maximum value of DSPL among all one-third-octave frequency bands corresponds to source signals measured forward of the helicopter on the measurement plane.

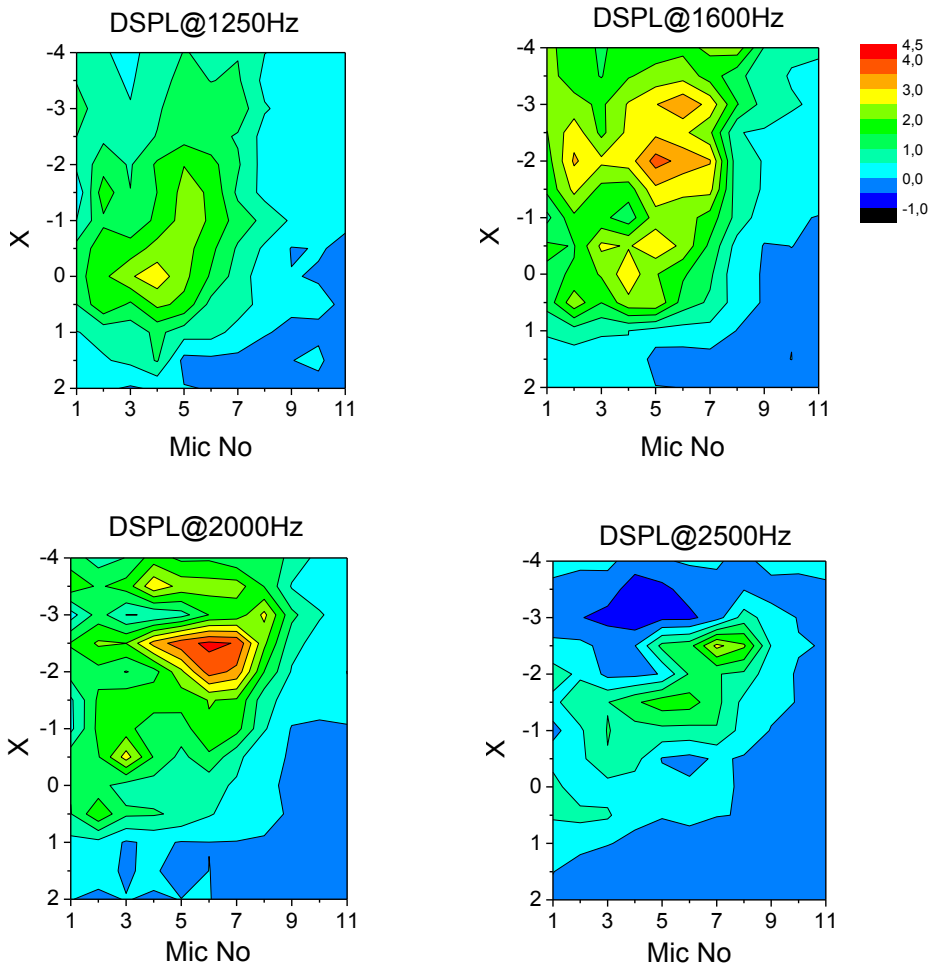

Figure 3-15: DSPL after *R'*=120m of propagation; DSPL shown at one-third-octave frequency bands centred at 1250Hz, 1600Hz, 2000Hz, and 2500Hz; axes indicate the position on the

measurement plane (microphone number and streamwise position of the microphone array) to which the calculated DSPL corresponds.

DSPL was also computed in frequency bands of the spectrum, other than octave and one-third-octave bands, that are specific to helicopter noise. Specifically, we considered the low frequency band (LF) [SPL comprising low frequency levels from the 2nd to the 10th blade passage frequency harmonics (bpfh); an approximate measure for thickness and high speed noise], the medium frequency band (MF) [SPL comprising mid frequency levels from the 6th to the 40th bpfh; an approximate measure for BVI impulsive noise], and the high frequency band (HF) [SPL comprising frequency levels from the 40th to the 80th bpfh; the region that starts after the BVI frequency region and can extend up to the end of the the discrete frequency spectrum of the BVI pulse]. In general, HF was found to be amplified by nonlinear effects (up to 2dB after 1000m of propagation), while small negative values are yielded for LF and MF. This reveals that nonlinear propagation distortion causes energy to be shifted from the thickness and BVI noise frequency regions to higher frequencies.

The overall A-weighted SPL value (OASPL) does not increase appreciably by nonlinear effects. This is attributed to the fact that OSPL is mostly determined by the largest SPL values of the spectrum. For helicopters, this is the low frequency end of the spectrum, which, however, remains almost unaffected by nonlinear effects.

Calculations were repeated for different meteorological conditions. It was observed that neither the DSPL values, nor the affected areas around the rotor change appreciably.

Finally, the calculations were repeated using instantaneous BVI signals, which contain greater levels of broadband noise compared to the averaged BVI signals used initially. The area on the measurement plane where signals undergo the strongest nonlinear propagation distortion remains the same as with the averaged BVI signals (that is, forward of the helicopter as seen in Figure 3-15). The magnitude of the DSPL, however, is reduced to less than half. Nevertheless, these smaller values appear in twice as many one-third-octave frequency bands as before [see, for example, Figure 3-12 (a), where nonlinear effects affect the entire high frequency region, above 4000 Hz].

3.3.1.1 Discussion and far-field directivity

In the following certain assumptions used for the generation of the database are discussed and an updated database is provided considering the BVI source to be located close to the tip of the blade rather than at the rotor hub.

The measured signals used as noise source signals in this study contain many types of rotor noise. No assumption has been made that they are composed solely by impulsive events. Their nonlinear evolution is predicted irrespective of the mechanism that generated the source signals and irrespective of the noise types that they contain. Furthermore, the nonlinear evolution of a noise field depends largely on the pressure time signal at source, which in turn depends on the flight conditions. Thus, the results in the database should only be used for flight conditions similar to those for which they were generated. However, the results in the database do not depend on the location of the measurement plane, as any point along the propagation path can be considered as the starting point of the calculations.

The database results presented in the previous section have been obtained considering the rotor hub as the location of the source, not the true origin of the BVI noise. Employment of a standard BVI localization technique [70] provides four BVI locations on the advancing side. Because retreating side type evolution (negative polarity of the source signal) yields negligible DSPL and regards only a small fraction of data, retreating side type measured signals on the measurement plane have been excluded. For the advancing side type signals a single BVI source location has been considered as the mean position of the four identified BVI source locations. The BVI source is located at 0.9 radius on the rotor disk and at the 60 deg rotor azimuth.

The calculations have been repeated for the advancing side type signals with the new source location. The propagation path is R' in this case [see Figure 3-14(b)-(d)] and starts from the BVI source close to the tip (as described above), passes through the microphone grid and reaches receivers on hemispherical surfaces that move with the helicopter. It was observed that the effect on the magnitude of DSPL is very small. This is expected, as for long propagation distances, $R' \simeq R$, and therefore DSPL remains the same, while for shorter propagation distances, the magnitude of DSPL is so small that corrections for noise source locations are negligible. Although, the far field directivity

of BVI (that is using R' instead of R) does not affect the magnitude of DSPL, it affects considerably the receiver location on the hemisphere to which the resulted DSPL corresponds. See, for example, Figure 3-14 (d). Both propagation paths, R and R', pass through the same microphone on the measurement plane and both use the signal measured at that microphone as source signal. However, the two propagation paths lead to different receiver locations on the hemisphere. In other words, although the magnitude of DSPL is the same in both cases, it refers to different locations around the helicopter. When DSPL results are presented in correspondence to the microphone location on the measurement plane (see, for example, Figure 3-15), the source location is not important. When, however, DSPL results are presented at receiver locations around the helicopter, then the far field directivity of BVI noise must be taken into account.

DSPL results are shown in Figure 3-16 and Figure 3-17 at receiver locations on an hemisphere that moves with the helicopter and has radius R'=120m as a function of the azimuth and elevation angle [see Figure 3-14(b)-(d)]. Figure 3-16 shows the receiver locations around the helicopter that are mostly affected by nonlinear propagation distortion at each one-third-octave frequency band. (In contrast, Figure 3-15 shows the measured signals on the measurement plane that undergo the strongest distortion at each one-third-octave frequency band). Figure 3-17 shows the maximum DSPL irrespective of the frequency band at which the maximum occurs. It can be observed that receiver locations from 180 to 220 deg azimuth angle and from -40 to -70 deg elevation angle are mostly affected. It is noted that the directivity pattern depicted in Figure 3-17 is very similar to that of type "α" BVI pulses [71,72], which radiate to the front of the rotor.

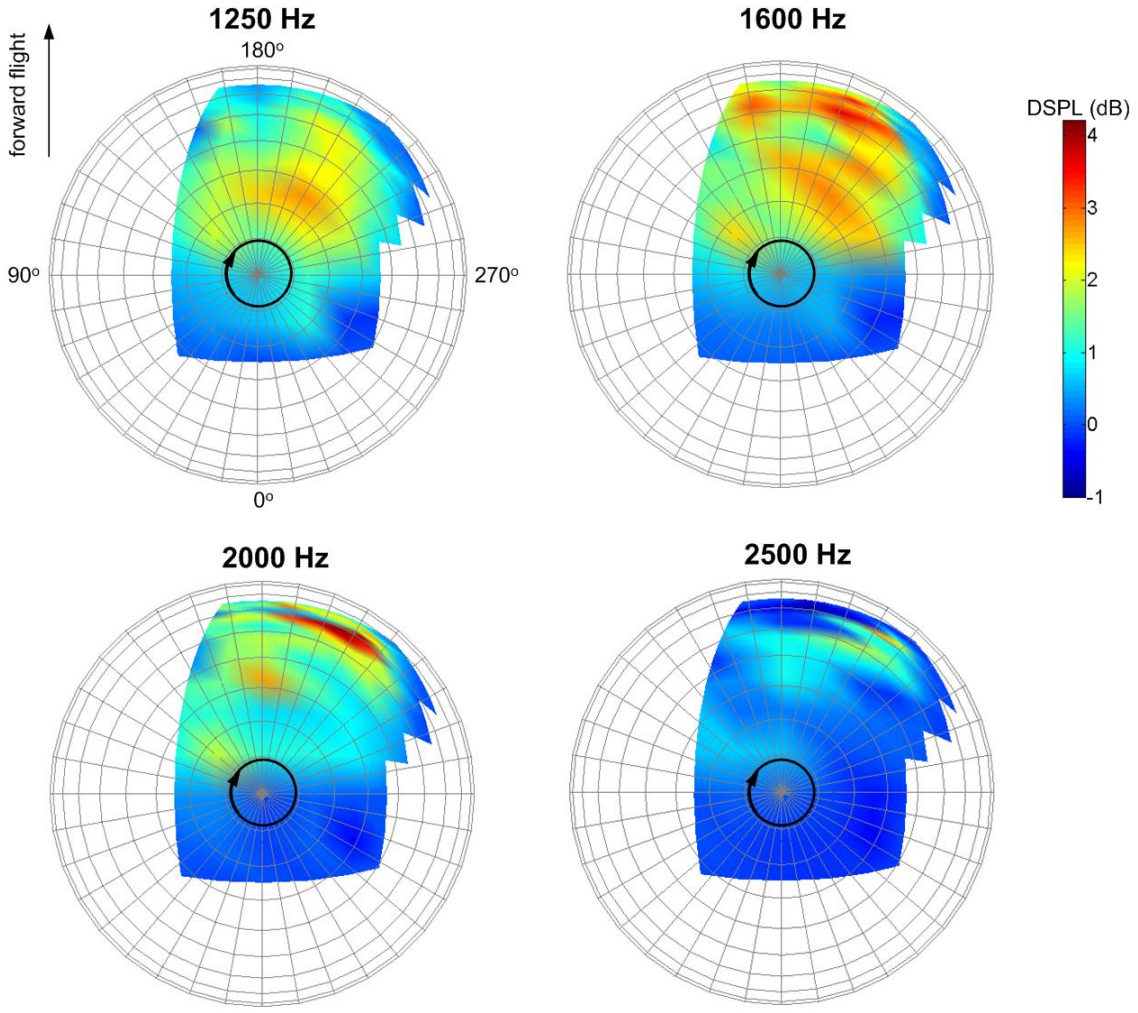

Figure 3-16: DSPL after *R'*=120m of propagation; DSPL shown at one-third-octave frequency bands centred at 1250Hz, 1600Hz, 2000Hz, and 2500Hz; grid indicates the receiver location on a hemisphere of radius *R'*=120m as a function of azimuth and elevation angle at increments of 10 deg.

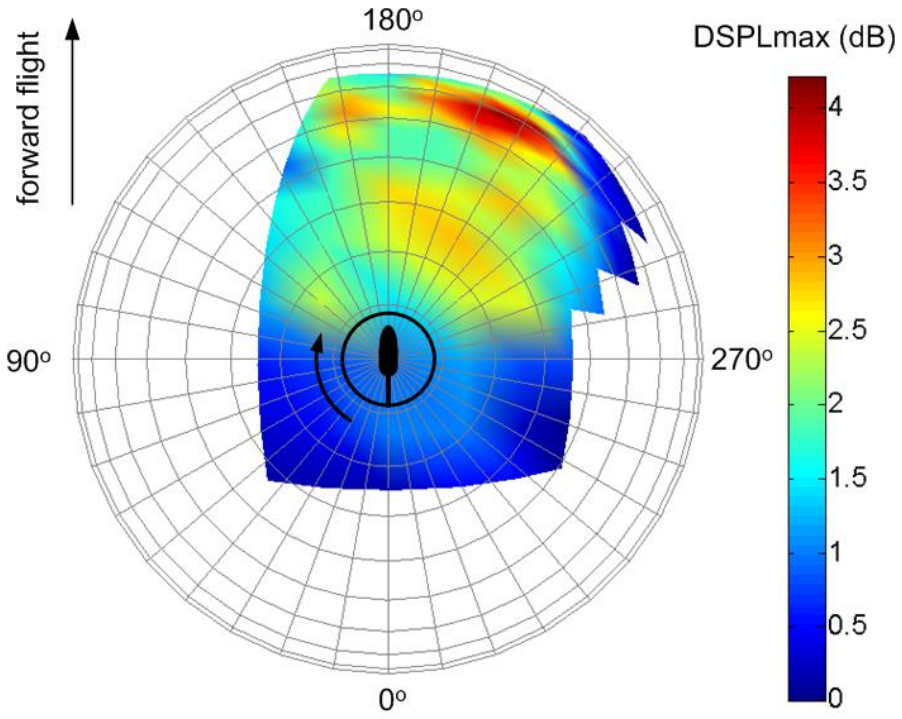

Figure 3-17: DSPLmax (maximum DSPL value irrespective of the one-third-octave frequency band it occurs) after R'=120m of propagation; grid indicates the receiver location on a hemisphere of radius R'=120 m as a function of azimuth and elevation angle.

3.3.2 Correlations

In this section a second remedy is presented that addresses the concern regarding the complexity of the nonlinear calculations. Correlations between predicted DSPL values after propagation and characteristics of the source signal have been investigated. The correlations established from the analysis of the database in hand can be used to provide a physical connection between the BVI noise characteristics and its nonlinear propagation, as well as, an estimate of DSPL in the propagation of BVI noise signals of similar rotors. This will, in turn, determine, if a detailed prediction of nonlinear effects employing the BE is merited.

Further, it should be mentioned that data points corresponding to retreating side type nonlinear evolution have been excluded from the correlations. The correlations regard, therefore, advancing side type nonlinear evolution. As mentioned earlier, this

type characterizes the majority of receiver locations and provides sizeable DSPL values, as opposed to the retreating side type, which yields negligible DSPL.

3.3.2.1 Predictors and nonlinear quantities

Many characteristics of the source signals have been investigated. More specifically, the following signal characteristics, as well as, many of their combinations haven been considered: OSPL, $P_{\max}$, $\left(DP/DT\right)_{\max}$ (the ratio of the maximum peak to trough pressure difference to the equivalent rise time, a characteristic of the steepness of the main/strongest BVI pulse), kurtosis, skewness, CF (crest factor), $dP_{\max}$ (maximum pressure difference between neighboring points in the digitized time signal, which is proportional to the maximum pressure derivative), the low frequency band LF , the medium frequency band MF , and the high frequency band HF .

The above signal characteristics have been correlated with the following quantities that describe nonlinear distortion: DSPL at the one-third octave frequency bands centered at 1600 Hz, 2000Hz and 2500 Hz, $\text{DSPL}_{\max}$ (the maximum value of DSPL irrespective of the one-third octave frequency band at which it occurs), and DSPL at the octave frequency bands centered at 1000Hz and 2000Hz. The correlations of the above nonlinear quantities with the source signal characteristics have been performed at propagation distances of R =120m, 300m, 500m and 1000m.

Only four of the many predictors investigated provided a good correlation with the nonlinear quantities; specifically, $P_{\max} \times CF$, $dP_{\max}$, HF and $\left(DP/DT\right)_{\max}$. Some of the remaining predictors did not correlate well with the nonlinear distortion quantities, while others failed even to predict which noise source signals will undergo stronger nonlinear distortion. Consider, for example, the predictor OSPL that characterizes the intensity of the noise source signal and could, thus, provide an indication on nonlinear effects. However, by observing Figure 3-18, it can be concluded that microphones on the measurement plane having high values of OSPL do not coincide with microphones that produce high values of $\text{DSPL}_{\max}$. It was found that $\left(DP/DT\right)_{\max}$ (see Figure 3-18) is the best predictor for indicating the areas on the measurement plane that will produce high values of $\text{DSPL}_{\max}$. This correlation agrees

with earlier observations of this thesis that the steepness of the main BVI pulse is an important factor for the nonlinear distortion of the BVI signal.

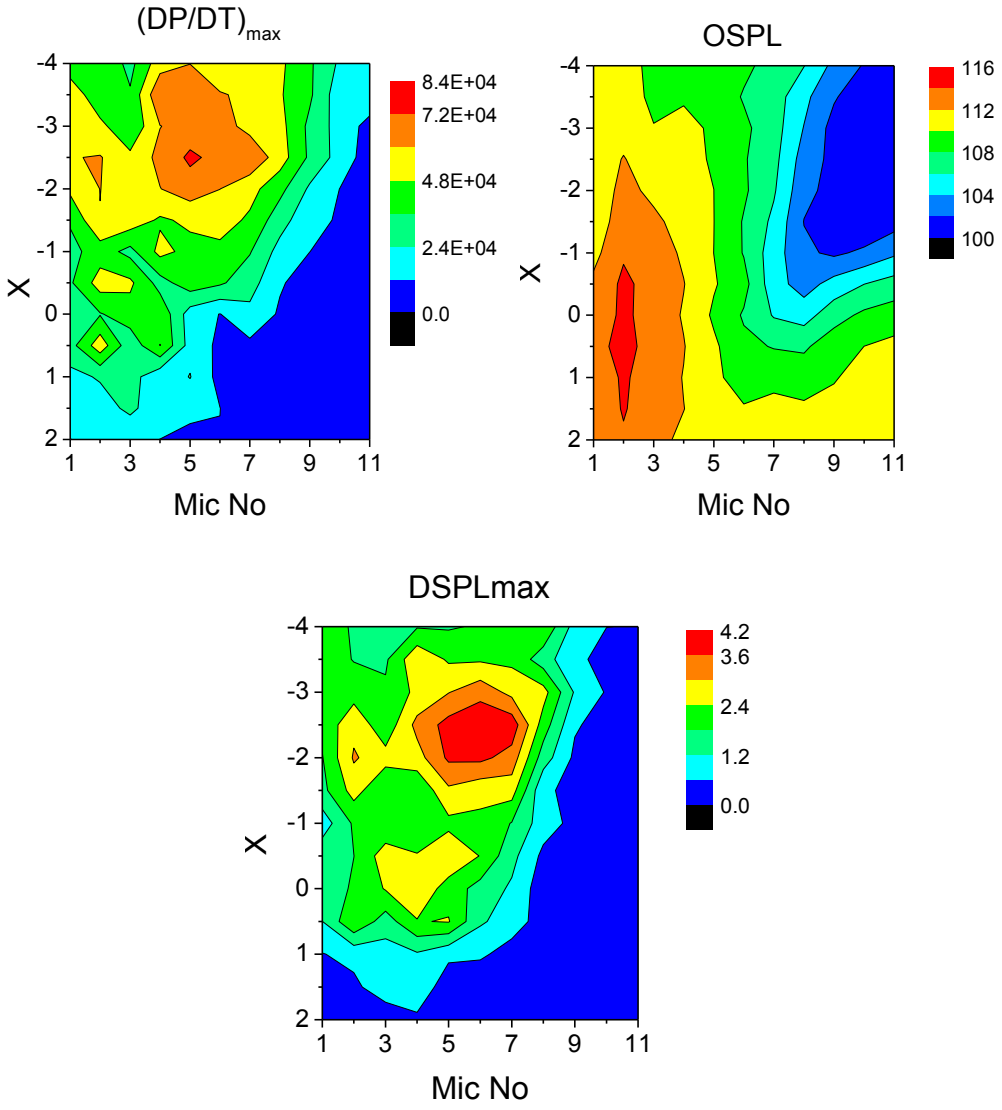

Figure 3-18: Predictors (noise source signal characteristics) $(DP/DT)_{max}$ and OSPL shown at R=16m from source; nonlinear quantity $DSPL_{max}$ (maximum DSPL value irrespective of the one-third-octave frequency band it occurs) after R'=120m of propagation; axes indicate the position on the measurement plane (microphone number and streamwise position of the microphone array) to which the DSPL corresponds.

3.3.2.2 Quantitative correlations between predictors and nonlinear quantities

Figure 3-19 shows examples of correlations between $DSPL_{max}$ and the four predictors: $P_{max} \times CF$, dP_{max}, HF and $(DP/DT)_{max}$ after R=120m of propagation distance. The good correlation can be observed. Lines are fitted between the points in the graphs showing the relation between the quantities. The equations of the fitted lines are to be used for predicting $DSPL_{max}$ after R=120m of propagation distance for averaged BVI signals in low speed descent:

$$DSPL_{max} = -0.1 + 0.015(P_{max} \times CF) \tag{3.6}$$

$$DSPL_{max} = -0.4 + 1.5\, dP_{max} \tag{3.7}$$

$$DSPL_{max} = 12.7 - 0.423HF + 3.45 \times 10^{-3} HF^2 \tag{3.8}$$

$$DSPL_{max} = -0.1 + 4.7 \times 10^{-5} \left(\frac{DP}{DT} \right)_{max} \tag{3.9}$$

Similar equations connecting the four aforementioned predictors with $DSPL_{max}$ can be derived for all propagation distances. Finally, the prediction of $DSPL_{max}$, when instantaneous signals are considered instead of averaged signals, can be based on equations of similar form that have coefficients approximately half of the ones presented here.

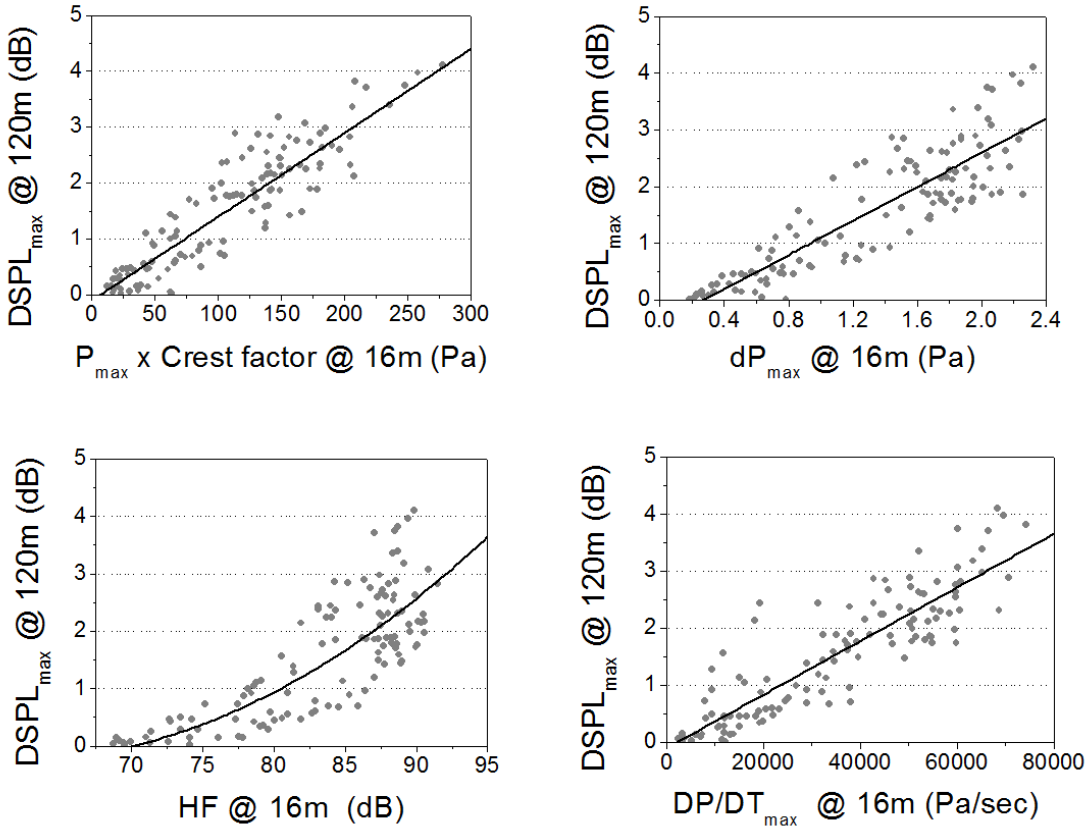

Figure 3-19: Correlations between DSPLmax after R=120m of propagation and characteristics of the noise source signals (predictors).

3.3.2.3 Prediction examples

The correlations presented in the previous subsection are used to make predictions, which are subsequently checked against a second numerically generated database of a similar rotor. The second database is generated similarly to the first one and is based on a different set of HELISHAPE measurements. The flight conditions and the measuring points were the same, but the rotor with a rectangular blade tip was used instead of the swept-back parabolic-anhedral tip. Because the noise source signals are slightly different at the two databases, their nonlinear evolution is also different. The correlations, however, can be used to provide an estimate of DSPL_{max}.

Table 3-2 shows an example of the DSPL_{max} calculation for Mic 3 / x=-1 after R=120 m of propagation. The source data at Mic 3 / x=-1 are analyzed first and the

values of the four predictors [$P_{\max} \times CF$, $dP_{\max}$, HF and $\left(DP/DT\right)_{\max}$] are computed. Based on the values of the predictors and Eqs. (3.6)-(3.9) estimates of $\mathrm{DSPL}_{\max}$ are computed, numerically averaged and compared against the $\mathrm{DSPL}_{\max}$ in the second database for point Mic 3/ x=-1 after R=120 m of propagation. The predicted value using the correlation equations is very close to the one predicted by employing the BE.

Mic 3 / x=-1 @ R=120m		
Predictor	**Predictor Value**	**DSPL (dB)**
$P_{\max} \times CF$	195.36 Pa	2.83
$dP_{\max}$	2.411	3.2
HF	90.095 dB	2.59
$\left(DP/DT\right)_{\max}$	49183	2.21
Average predicted $DSPL_{\max}$		**2.70**
Actual $DSPL_{\max}$		**2.36**

Table 3-2: Prediction example of $\mathrm{DSPL}_{\max}$ using correlation equations for Mic 3/ x=-1.

Figure 3-20 shows the predicted $\mathrm{DSPL}_{\max}$ values (based on the correlations and computed as described above) and the values of $\mathrm{DSPL}_{\max}$ predicted by the BE after R=120m of propagation. The comparison is done for several microphones on the measurement plane. It can be observed that the predictions are reasonably good.

It should be emphasized that the correlations presented here regard averaged noise signals and should be used only for similar helicopter rotors and similar flight conditions. It is very difficult, if at all possible, to find simple correlations to predict propagation distortion in the general case. Nonlinear propagation distortion depends highly on the main BVI pulse, which in turn depends on the aerodynamic properties of

the blade vortex interaction phenomenon. More specifically, the width of the BVI pulse depends on the core size of the vortex and the tip velocity of the blade, while the magnitude of the pulse is related to the vortex strength and the blade attack angle [72]. Thus, BVI locations experiencing the strongest nonlinear effects are the points of high speed interactions, small core size/strong vortices, and great blade attack angles. Nonlinear propagation distortion of BVI pulses is, therefore, very sensitive to blade tip, blade tip Mach number and flight conditions (advance ratio and climbing angle).

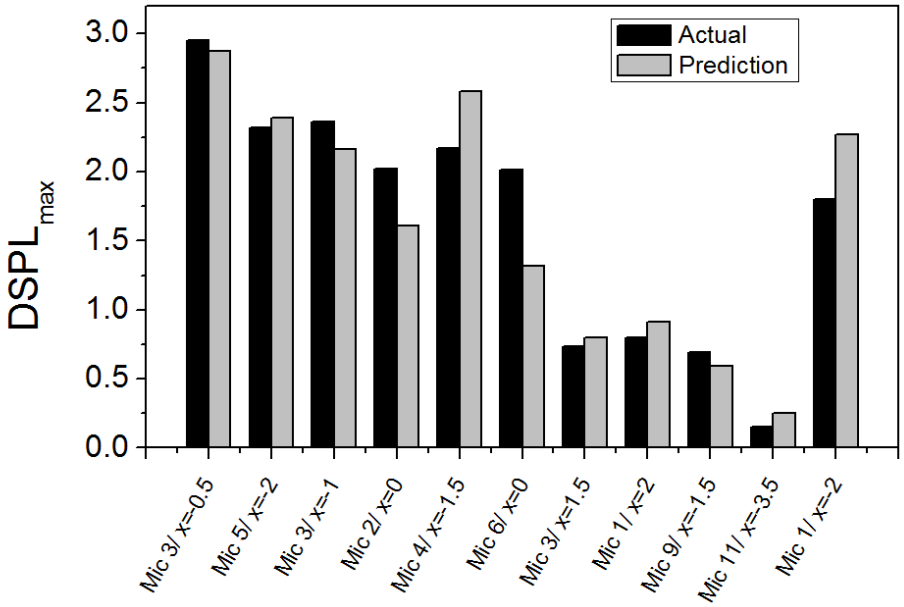

Figure 3-20: Comparison between DSPLmax after R=120m of propagation predicted from Eqs (3.6)-(3.9) (solid) and by employing Eq. (2.1)(pattern); noise source signals from the rectangular blade tip database; noise source signals measured at the locations indicated in the horizontal axis.

3.3.3 Phase Assignment

The problem of the missing phase information is addressed in this paragraph. Often the power spectrum of helicopter noise is provided, not the signal itself. A given pressure time signal corresponds to a unique power spectrum. On the contrary, to a given power spectrum correspond an infinite number of pressure time signals, each

having a different phase distribution. The phase distribution affects the shape of the signal and in turn its nonlinear distortion. In the cases of aircraft noise, a random phase uniformly distributed in $[-\pi : \pi]$ is assigned in order to re-construct the pressure time signal. This method is inappropriate for helicopter noise, as it eliminates the characteristic pulses contained in a helicopter noise signal. The present work proposes the assignment of constant phases, in addition to random phases, in appropriately selected frequencies. The aim of the proposed phase assignment is to create a signal whose main BVI pulses will be similar enough to the main BVI pulses of the original time signal, so that both the re-constructed and the original time signal exhibit the same nonlinear behaviour.

3.3.3.1 Frequency regions

For the application of the phase assignment method the spectrum of the noise source signal is divided into three regions depending on the different noise mechanisms affecting them.

a) Thickness region

The region from the 2nd to the 10th blade passage frequency harmonic (bpfh) [4], or alternatively from the 2nd to the 5th bpfh [73], is considered to be an approximate measure for thickness and high speed noise. In the signals of our database thickness noise was found to be most evident in the region from the 1st up to the 5th bpfh.

b) Main BVI pulse region

The BVI frequency region is defined as the region from the 6th to the 40th bpfh [74], or from the 5th to the 30th [73]. In the averaged BVI signals at hand the start of the BVI region occurs at the 5th bpfh, while the ending frequency varies with the microphone position, from the 50th bpfh for the less impulsive signals to the 80th bpfh for the more impulsive. As this region is by definition discrete, the end of the region can

be determined by visual observing, where the local maxima of the spectrum cease to be equidistance (see Figure 3-21).

c) Broadband region

For the signals at hand broadband noise includes mainly some components of blade wake interaction (BWI) [5]. Broadband frequency region is set from the end of the main BVI region to the end of the spectrum.

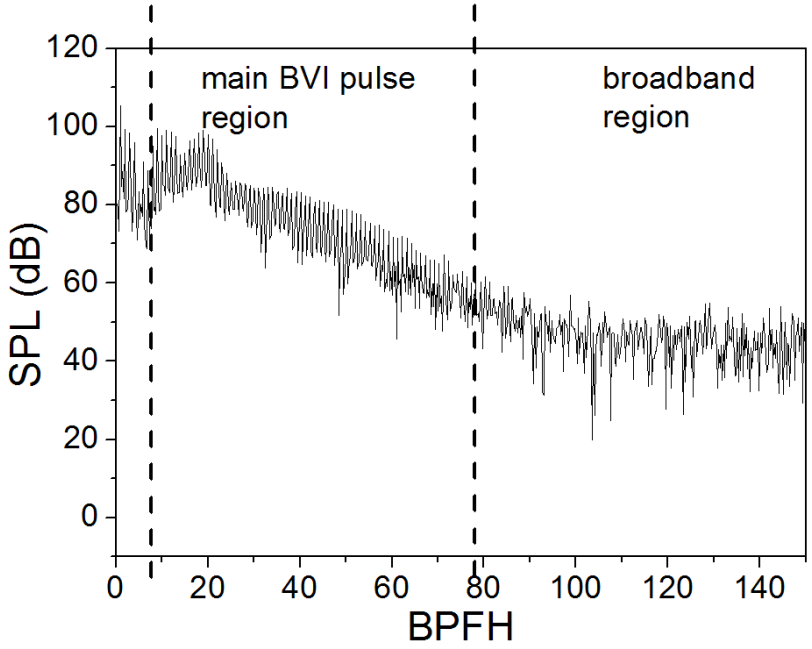

Figure 3-21: Noise spectrum vs. blade passage frequency harmonics (BPFH) for noise source signal measured at Mic 6 / x=-2.5; spectrum divided into frequency regions for the phase-assignment method.

3.3.3.2 Signal Re-construction

Consider the spectrum of a noise source signal, as, for example, the one shown in Figure 3-21. The spectrum can be divided in the frequency regions as discussed above. Firstly, a time signal is created via inverse Fourier transform by considering a constant phase of $-\pi$ for all frequencies up to and excluding the 5th bpfh and zeroing out all other values of the spectrum. A so-constructed signal is shown in Figure 3-22(a).

By applying the constant phase $-\pi$ in the thickness frequency region, a negatively valued symmetrical pulse is created, which resembles loading/thickness noise.

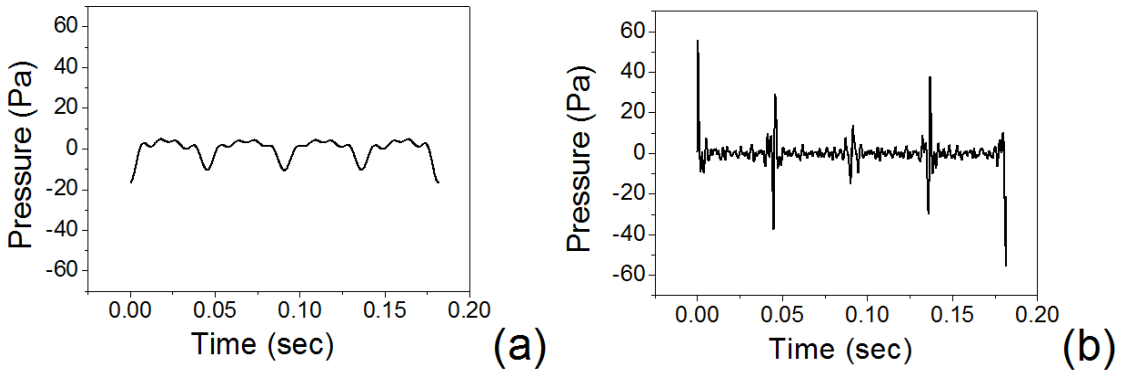

Figure 3-22: Stage 1 of the phase assignment method: signal corresponding to the thickness frequency region [(a)]; stage 2 of the phase assignment method: signal corresponding to the main BVI pulse and broadband frequency region [(b)].

Subsequently, a second time signal is created by assigning a constant phase of $-\pi/2$ to all blade passage frequencies and their neighboring shaft frequencies (the quarter bpfh) in the BVI frequency region. To the remaining frequencies in the BVI frequency region, as well as, to all frequencies in the broadband noise frequency region, random phases are assigned. The values of the spectrum in the thickness frequency region are zeroed out. A so-constructed signal is shown in Figure 3-22 (b). In general, assigning a constant phase contributes to the re-construction of a single BVI pulse within each blade passage, while the assigning of random phases contributes to the re-construction of the non-BVI noise between blade passages. Ideally the BVI energy is distributed only to the blade passage harmonics. However, increased unsteadiness and blade-to-blade differences of the acoustic impulses are shown to spread the energy from the blade passage harmonics to the shaft harmonics [74]. This is taken into account in the proposed phase assignment and an appropriate energy distribution between BVI pulses and non-BVI noise seems to be attained. Further, the value of the constant phase of $-\pi/2$ is applicable to advancing side BVI signals. For retreating side BVI signals the value of $\pi/2$ is used instead.

Finally, the two constructed signals are added together to create the final signal. Before their addition, the signal corresponding to BVI noise [Figure 3-22 (b)] is shifted

in time in order to start later than the signal corresponding to the thickness frequency region [Figure 3-22 (a)]. The time shift is equal to half the time between the first two blade passages. This is done to simulate the phase difference between thickness and BVI noise. The final signal is shown in Figure 3-23(a).

It should be emphasized that the purpose of the phase assignment method is to create a time signal that has the same power spectrum and same impulsive characteristics with the original time signal, so that both signals have the same nonlinear behaviour (expressed in DSPL). The DSPL plots should be similar, not the signals themselves. Finally, it should be recalled that the signals used in this analysis are averaged signals containing low levels of broadband noise. Direct application of the phase assignment method for instantaneous signals can yield under-prediction of the high frequency region and over-prediction of the mid frequency region.

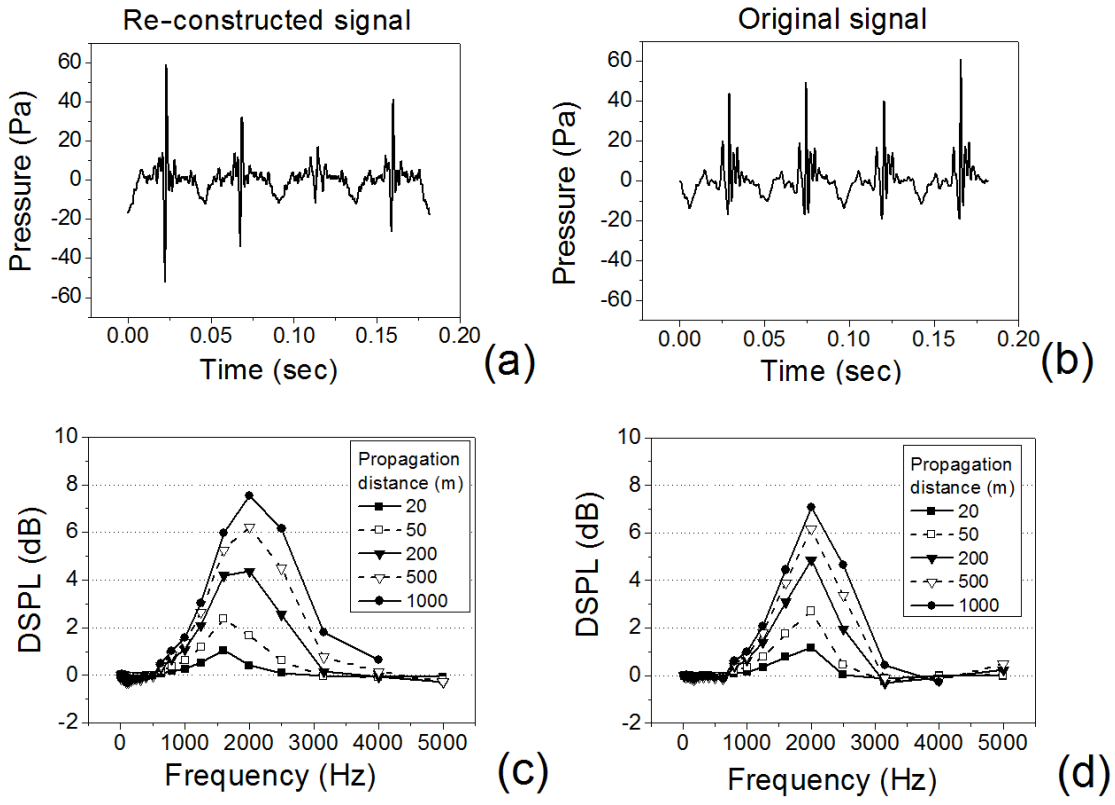

Figure 3-23: Phase assignment method: Re-constructed [(a)] and original [(b)] pressure time signals and their corresponding DSPL plots [(c), (d)] for various propagation distances R; Mic 6 / x=-2.5.

3.3.3.3 Prediction examples

The proposed phase assignment method has been applied to several noise source spectra. Time signals have been constructed from the noise spectra and numerically propagated to predict DSPL over all frequency bands. The DSPL yielded from the re-constructed signal through the phase assignment method compares reasonably well with the DSPL yielded from the original noise source signal (Figure 3-23). The good comparison is further illustrated in Figure 3-24 for other receiver locations in both the advancing and retreating BVI side.

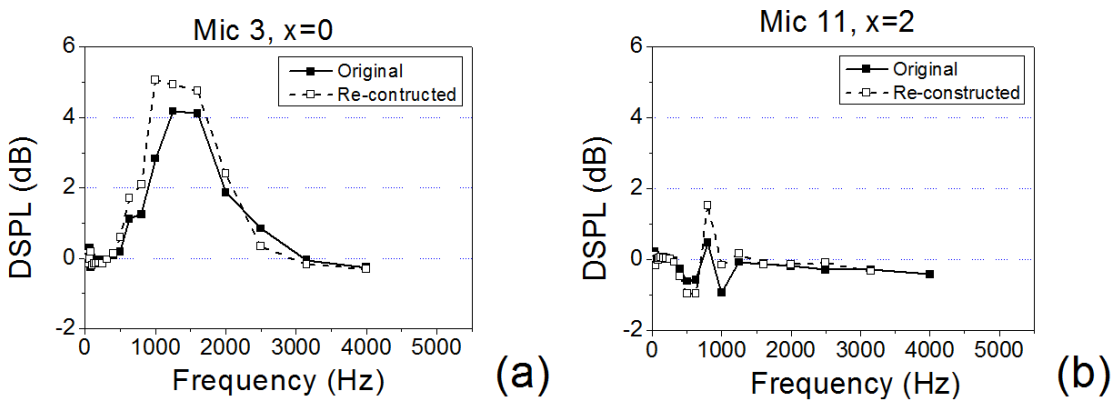

Figure 3-24: Phase assignment method: Comparison between DSPL after R=1000m of propagation yielded by the original noise source signal and the re-constructed signal; noise source signals at the advancing side Mic 3/ x=0 [(a)] and the retreating side Mic 11 / x=2 [(b)].

A final note is to be added. The peak of the DSPL bell ($DSPL_{max}$) was shown in the previous section to depend on certain characteristics of the noise signal at source, specifically on $P_{max} \times CF$, dP_{max} , HF and $\left(DP/DT\right)_{max}$. The four predictors regard the original signals and should not be applied to the re-constructed ones. Except of the predictor HF , which is identical in both signals, (it is recalled that both signals have by construction the same power spectrum), the other three predictors are larger in the re-

constructed signal. This happens mainly, because the first BVI pulse in the re-constructed signal is, in general, stronger than in the original signal (see Figure 3-23). On the other hand, however, BVI pulses in other blade passages of the re-constructed signal are smaller than in the original. So, if one, (instead of evaluating the predictors over the entire signal), evaluates them at each blade passage and takes the average, then the so-calculated average values of the predictors are similar to those of the original signal.

4 Near Field Study: Interaction of Sound with Flow and Solid Boundaries

Except from the atmospheric phenomena that affect the far field propagation of air vehicle noise, the local flow field and the interactions of sound with the aircraft's surfaces strongly affect the acoustic near field of the air vehicle. These near field effects are important for the sound received by the aircraft's passengers and they can also significantly alter the aircraft's emitted sound signature.

The problem with near-field acoustic analysis is that for complex geometries the computational solution of the problem can be very demanding. Hybrid grids, consisting of prisms, tetrahedra, hexahedra and pyramids in 3D, are quite important to treat complex geometries and flow fields [75]. However, high-order methods, which are needed for accurate prediction of sound propagation, cannot be easily applied to hybrid grids, and have a high cost. On the other hand, low-order methods can be easily applied to hybrid grids [76] with relatively low cost. They could provide an alternative if adequate accuracy is achieved. However, low-order methods which simulate propagation of the *total* flow and acoustic field, experience problems in capturing low amplitude acoustic waves [77]. The answer to this problem is given by the use of the flow/acoustics decoupling approach for sound propagation which offers the possibility of using *low order* numerical methods with hybrid meshes. Low-order methods applied to acoustic perturbation equations have been presented in the past for 2-D acoustic problems [77-80]. Those methods were applied to structured grids and were able to capture acoustic waves given the appropriate grid density.

In the present work, a new low-order *combined* CFD/CAA method for the prediction of sound propagation and diffraction in unsteady compressible flow using 3-D hybrid grids is investigated. The *total* flow quantities in the Euler equations of inviscid flow are assumed to be the sum of flow and acoustic variables without the constraint of incompressible or time averaged flow. The decomposition into flow and acoustic fields results in separate equations for the two fields. Consequently, different computational schemes and meshes can be applied for each field. Similar techniques have been developed for flow-structure interaction problems, such as in Ref. [81].

Moreover, the use of grid adaptation in sound propagation is another aspect of the present work. Primarily, grid adaptation has been applied to flow fields (see review in [82]), with little application to sound propagation problems. The present work employs acoustics-guided adapted grid refinement, which improves the accuracy of capturing the acoustic field.

The present chapter is divided into four main sections. Initially, the mathematical formulation of the flow/acoustics interaction method is presented, followed by a section on the numerical implementation for the present scheme. The third section contains the validation cases for sound propagation and interaction with solid boundaries, while at the last section the suggested model is applied to the case of a flying airplane, investigating the effect of flow field and wing shielding on the near-field acoustic levels.

4.1 Flow –Acoustics field decomposition and coupling

In the present study both the flow and acoustic fields are considered to be inviscid. This assumption is quite good for the acoustic field, as viscous effects are slow on an acoustic time scale. Moreover, the inviscid flow assumption is applicable to a wide range of aerodynamic applications. The three-dimensional compressible Euler equations in a Cartesian coordinate system may be written in the form [83]:

$$\frac{\partial U}{\partial t}+\frac{\partial F}{\partial x}+\frac{\partial G}{\partial y}+\frac{\partial H}{\partial z}=0 \tag{4.1}$$

The considered variable vector is given by:

$$U=\left\{\rho,\quad \rho u,\quad \rho \upsilon,\quad \rho w,\quad e\right\} \tag{4.2}$$

where ρ is the fluid density and u,υ,w are the velocity components in the three coordinate directions, respectively. The total energy per unit volume of fluid is defined as

$$e = \rho\left[C_v T + \frac{1}{2}\left(u^2 + \upsilon^2 + w^2\right)\right] = \frac{p}{\gamma - 1} + \frac{1}{2}\rho\left(u^2 + \upsilon^2 + w^2\right) \qquad (4.3)$$

where p, T, C_v and γ are the pressure, temperature, constant volume specific heat, and specific heat ratio, respectively. Note that, in Eq.(4.3), the ideal gas law is used to relate pressure and temperature. The convection terms of Eq. (4.1) are given by

$$\begin{aligned} F &= \left\{\rho u, \quad \rho u^2 + p, \quad \rho u\upsilon, \quad \rho uw, \quad (e+p)u\right\} \\ G &= \left\{\rho \upsilon, \quad \rho \upsilon u, \quad \rho \upsilon^2 + p, \quad \rho \upsilon w, \quad (e+p)\upsilon\right\} \\ H &= \left\{\rho w, \quad \rho wu, \quad \rho w\upsilon, \quad \rho w^2 + p, \quad (e+p)w\right\} \end{aligned} \qquad (4.4)$$

It is considered that the above equations represent the *total* field containing the flow and acoustic parts. Then, the *total* variable vector is split into its fluid flow part ($\overline{U}$), and the acoustic field portion (U'):

$$U = \bar{U} + U' \qquad (4.5)$$

Substitution of the above decomposition into Eq. (4.1) leads to the following:

$$\left(\frac{\partial \bar{U}}{\partial t} + \frac{\partial \bar{F}}{\partial x} + \frac{\partial \bar{G}}{\partial y} + \frac{\partial \bar{H}}{\partial z}\right) + \left(\frac{\partial U'}{\partial t} + \frac{\partial F'}{\partial x} + \frac{\partial G'}{\partial y} + \frac{\partial H'}{\partial z} + \frac{\partial F'_n}{\partial x} + \frac{\partial G'_n}{\partial y} + \frac{\partial H'_n}{\partial z}\right) = 0 \qquad (4.6)$$

where $\bar{F}, \bar{G}, \bar{H}$ are the flow convective vectors, F', G', H' are the vectors containing the linear acoustic terms, and F'_n, G'_n, H'_n are the nonlinear acoustics terms in the three coordinate directions.

At this point it is assumed that the acoustics field does not affect the flow field appreciably, thus giving the following equations for the flow and acoustics parts:

$$\frac{\partial \bar{U}}{\partial t}+\frac{\partial \bar{F}}{\partial x}+\frac{\partial \bar{G}}{\partial y}+\frac{\partial \bar{H}}{\partial z}=0 \tag{4.7}$$

where the expressions of the vectors $\bar{U},\bar{F},\bar{G},\bar{H}$ are the same as the ones for U,F,G,H [Eqs. (4.2) and (4.4)].

The remaining perturbation terms yield the following system, which has also been employed in previous work [39,40]:

$$\frac{\partial U'}{\partial t}+\frac{\partial F'}{\partial x}+\frac{\partial G'}{\partial y}+\frac{\partial H'}{\partial z}+\frac{\partial F'_n}{\partial x}+\frac{\partial G'_n}{\partial y}+\frac{\partial H'_n}{\partial z}=0 \tag{4.8}$$

The above system is intended to model acoustics propagation and not flow generated sound. Specifically, the expressions of the acoustics terms are:

$$U'=\begin{Bmatrix}\rho'\\ \bar{\rho}u'+\rho'\bar{u}+\rho'u'\\ \bar{\rho}\upsilon'+\rho'\bar{\upsilon}+\rho'\upsilon'\\ \bar{\rho}w'+\rho'\bar{w}+\rho'w'\\ e'\end{Bmatrix} \tag{4.9}$$

$$F'=\begin{Bmatrix}\bar{\rho}u'+\rho'\bar{u}\\ \rho'\bar{u}^2+2\bar{\rho}\bar{u}u'+p'\\ \bar{\rho}\bar{u}\upsilon'+\bar{\rho}u'\bar{\upsilon}+\rho'\bar{u}\bar{\upsilon}\\ \bar{\rho}\bar{u}w'+\bar{\rho}u'\bar{w}+\rho'\bar{u}\bar{w}\\ \left(\bar{e}+\bar{p}\right)u'+\left(e'+p'\right)\bar{u}\end{Bmatrix} \tag{4.10a}$$

$$G'=\begin{Bmatrix}\bar{\rho}\upsilon'+\rho'\bar{\upsilon}\\ \bar{\rho}\bar{\upsilon}u'+\bar{\rho}\upsilon'\bar{u}+\rho'\bar{\upsilon}\bar{u}\\ \rho'\bar{\upsilon}^2+2\bar{\rho}\bar{\upsilon}\upsilon'+p'\\ \bar{\rho}\bar{\upsilon}w'+\bar{\rho}\upsilon'\bar{w}+\rho'\bar{\upsilon}\bar{w}\\ \left(\bar{e}+\bar{p}\right)\upsilon'+\left(e'+p'\right)\bar{\upsilon}\end{Bmatrix} \tag{4.10b}$$

$$H'=\begin{Bmatrix}\bar{\rho}w'+\rho'\bar{w}\\ \bar{\rho}\bar{w}u'+\bar{\rho}w'\bar{u}+\rho'\bar{w}\bar{u}\\ \bar{\rho}\bar{w}\upsilon'+\bar{\rho}w'\bar{\upsilon}+\rho'\bar{w}\bar{\upsilon}\\ \rho'\bar{w}^2+2\bar{\rho}\bar{w}w'+p'\\ \left(\bar{e}+\bar{p}\right)w'+\left(e'+p'\right)\bar{w}\end{Bmatrix} \tag{4.10c}$$

and

$$F'_n = \begin{Bmatrix} \rho' u' \\ 2\rho' u' \bar{u} + \bar{\rho} u'^2 + \rho' u'^2 \\ \bar{\rho} u' \upsilon' + \rho' \upsilon' \bar{u} + \rho' u' \bar{\upsilon} + \rho' u' \upsilon' \\ \bar{\rho} u' w' + \rho' w' \bar{u} + \rho' u' \bar{w} + \rho' u' w' \\ u'(e' + p') \end{Bmatrix} \qquad (4.11)\text{a}$$

$$G'_n = \begin{Bmatrix} \rho' \upsilon' \\ \bar{\rho} u' \upsilon' + \rho' \upsilon' \bar{u} + \rho' u' \bar{\upsilon} + \rho' u' \upsilon' \\ 2\rho' \bar{\upsilon} \upsilon' + \bar{\rho} \upsilon'^2 + \rho' \upsilon'^2 \\ \bar{\rho} \upsilon' w' + \rho' w' \bar{\upsilon} + \rho' \upsilon' \bar{w} + \rho' \upsilon' w' \\ \upsilon'(e' + p') \end{Bmatrix} \qquad (4.11)\text{b}$$

$$H'_n = \begin{Bmatrix} \rho' w' \\ \bar{\rho} u' w' + \rho' w' \bar{u} + \rho' u' \bar{w} + \rho' u' w' \\ \bar{\rho} \upsilon' w' + \rho' w' \bar{\upsilon} + \rho' \upsilon' \bar{w} + \rho' \upsilon' w' \\ 2\rho' \bar{w} w' + \bar{\rho} w'^2 + \rho' w'^2 \\ w'(e' + p') \end{Bmatrix} \qquad (4.11)\text{c}$$

The acoustics field pressure (p') is related to the acoustics quantities with the following equation which is obtained from Eq. (4.3) applying the flow-acoustics decomposition:

$$\begin{aligned} e' = {} & \frac{p'}{\gamma - 1} + (\bar{\rho} + \rho')(u' \bar{u} + \upsilon' \bar{\upsilon} + w' \bar{w}) \\ & + \frac{1}{2}(\bar{\rho} + \rho')(u'^2 + \upsilon'^2 + w'^2) + \frac{1}{2}\rho'(\bar{u}^2 + \bar{\upsilon}^2 + \bar{w}^2) \end{aligned} \qquad (4.12)$$

The complete derivation of the 3D Nonlinear Perturbation Equations (NPE) can be found in Appendix A.

The non-dimensionalization of all equations was performed with reference to a characteristic geometry length, such as the obstacle height (*h*) or the sphere diameter (D) for the cases considered here. The velocities for both fields are normalized with the

ambient speed of sound (c_∞), the time with the term h/c_∞, the density with its ambient value (ρ_∞), and the pressure with $\rho_\infty {c_\infty}^2$.

In the present flow-acoustics coupling method, the flow quantities are obtained from solution of Eq. (4.7). The acoustic quantities are obtained from Eq. (4.8) in which the flow quantities are considered known from the preceding calculation with Eq. (4.7).

4.2 Numerical Implementation

The flow and acoustic fields are computed via a standard Finite-Volume space discretization with second order of accuracy. Time marching is done via a four-stage Runge-Kutta method. The scheme is of "central space difference" type, thus requiring the explicit addition of fourth order artificial dissipation.

4.2.1 Finite Volume Spatial Discretization

The Euler equations of inviscid flow are given in integral form for a computation element of volume *V* as follows:

$$\int_V \frac{\partial \bar{U}}{\partial t} dV + \int_V \left(\frac{\partial \bar{F}}{\partial x} + \frac{\partial \bar{G}}{\partial y} + \frac{\partial \bar{H}}{\partial z} \right) dV = 0 \qquad (4.13)$$

Consider a hybrid grid element (tetrahedron, prism, hexahedron or pyramid) with $\hat{i}, \hat{j}, \hat{k}$ being the unit vectors in the x, y, z directions, and $\hat{n}$ being the unit vector normal to the element surface ∂V. The volume integral containing the spatial derivatives in Eq. (4.13) is equivalent to a surface integral via the divergence theorem:

$$\iiint_V \left(\frac{\partial \bar{F}}{\partial x} + \frac{\partial \bar{G}}{\partial y} + \frac{\partial \bar{H}}{\partial z} \right) dV = \iint_{\partial V} \left(\bar{F}\hat{i} + \bar{G}\hat{j} + \bar{H}\hat{k} \right) \hat{n} dS \qquad (4.14)$$

The above surface integral equals the flow residual [$R(\bar{U})$] and is discretized as:

$$R(\bar{U}) = \sum_f \left(\bar{F} S_x + \bar{G} S_y + \bar{H} S_z \right)_f \qquad (4.15)$$

where the summation is over the faces (f) of the grid element, and S_x, S_y, S_z are the face areas projected on the yz, xz, xy planes, respectively. The flux vectors ($\bar{F}, \bar{G}, \bar{H}$) are considered at the face centers, and their values are obtained by averaging from the vertices of the triangular and quadrilateral faces, since the scheme stores the solution at grid points.

Similarly, for the acoustic field and the acoustics residual [$R(U')$] the space discretization involves the same summation over the faces:

$$R(U') = \sum_f \left[\left(F' + F'_n \right) S_x + \left(G' + G'_n \right) S_y + \left(H + H'_n \right) S_z \right]_f \qquad (4.16)$$

The Finite Volume scheme is supplemented with fourth order artificial dissipative terms in order to suppress the appearance of high frequency numerical oscillations [84,85]. The final scheme operations are cast in edge-based form suitable for hybrid grids [86].

Time discretization employs the following four-stage explicit Runge-Kutta method:

$$
\begin{aligned}
U^0 &= U^n \\
U^1 &= U^0 - \frac{1}{4}\frac{\Delta t\, R\left(U^0\right)}{V} \\
U^2 &= U^0 - \frac{1}{3}\frac{\Delta t\, R\left(U^1\right)}{V} \\
U^3 &= U^0 - \frac{1}{2}\frac{\Delta t\, R\left(U^2\right)}{V} \\
U^4 &= U^0 - \frac{\Delta t\, R\left(U^3\right)}{V} \\
U^{n+1} &= U^4
\end{aligned}
\tag{4.17}
$$

The superscripts (n, n+1) denote the time level and $R\left(U^n\right)$ is the residual at time level n. This method is second order accurate in time and is found stable for Courant numbers lower than $2\sqrt{2}$ [84]. The time step (Δt) used for the solution of both fields is given by the CFL condition [86].

4.2.2 Boundary Conditions

Considerable work has been done on acoustic boundary conditions, a review of which can be found in Ref [87]. The boundary conditions that were applied in this study are either Neumann, or Dirichlet type. Consistently with the discretization scheme, the Neumann type of conditions was implemented with the hybrid grids using low order extrapolations at each boundary element.

For the flow computation, characteristic boundary conditions [83] were applied at the farfield boundaries, while for wall boundaries the flow velocity normal to the wall was set to zero and all other flow variables were extrapolated from the interior.

Specifically, the acoustics boundary conditions applied at the farfield were:

$$
{p'_b}^{n+1} = {p'_{b+1}}^{n}
$$

$$v_b'^{\,n+1} = v_{b+1}'^{\,n}$$

$$w_b'^{\,n+1} = w_{b+1}'^{\,n}$$

In addition, when the acoustic farfield is an outlet, the following two conditions were added:

$$J_b^{+,n+1} = J_{b+1}^{+,n}$$

$$J_b^{-,n+1} = J_\infty^{-}$$

while, when the acoustic farfield is an inlet, the expressions are:

$$J_b^{-,n+1} = J_{b+1}^{-,n}$$

$$J_b^{+,n+1} = J_\infty^{+}$$

where $J^+ \equiv u' + \frac{2}{\gamma - 1} c_\infty$, $J^- \equiv u' - \frac{2}{\gamma - 1} c_\infty$. The subscripts b and b+1 indicate the boundary location, and the adjacent location in the interior of the computational domain, respectively. The derivation of the acoustic Riemann Invariants (J^+, J^-) can be found in Appendix B. The remaining acoustic variables at the farfield boundary can be determined using the following formulae:

$$u' = \frac{1}{2}\left(J^+ + J^-\right)$$

$$\rho' = \frac{p'}{c_{av}^{\,2}}$$

For the acoustics wall boundary conditions, the acoustic normal velocity was set to zero and all other variables were extrapolated from the interior. In the above formulas c_{av} is the average sound speed at the far field boundaries, which is used in order to avoid local instabilities due to sound speed variations near the boundaries.

4.3 Validation Results

The validation/test cases presented are grouped in three sections. The first deals with use of the low-order scheme combined with hybrid meshes for free-field sound propagation cases. Local grid refinement based on the acoustic field is employed, along with global refinement for grid convergence studies. Diffraction by solid boundaries is examined in the second section, while the third section investigates the flow-acoustics coupling method for various flow conditions.

4.3.1 Hybrid grids for free-field sound propagation

Free-field propagation cases will be examined in order to verify the method's ability to capture acoustic waves. In terms of sound propagation the cases of a monopole in a resting medium and a uniform flow field will be examined.

Sound propagation in a resting flow field

The case examined in this section is a monopole radiating in a flow field at rest. This is a benchmark case for acoustic propagation models which can be compared against a well known analytic solution [88]. The monopole is placed at the center of the computational domain which is discretized with a hybrid grid including all types of 3-D elements (see Figure 4-1). The computational domain used for the numerical experiments had dimensions 1 x 1 x 1 and the monopole source was located at its center (x, y, z = 0.5, 0.5, 0.5) having a radius of 0.05.

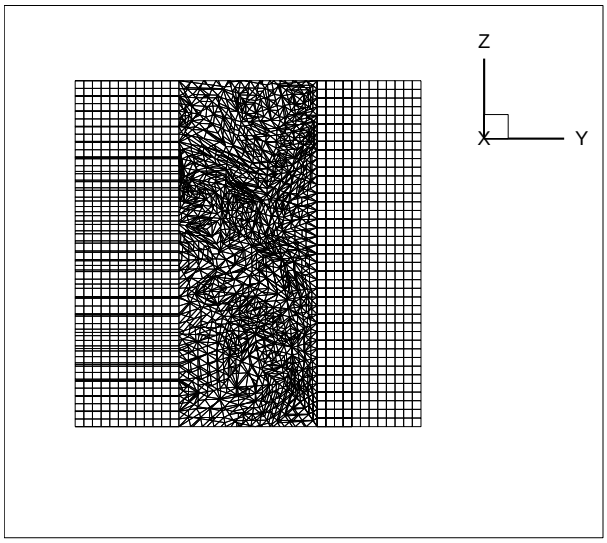

Figure 4-1: The hybrid grid used for monopole sound propagation includes prisms, tetrahedra, pyramids, and hexahedra. A cut through the mesh is shown with the monopole being located at the center of the depicted domain.

The monopole source has a finite radius and is captured by an approximately spherical portion of the local grid. The monopole orientation algorithm, that is used in order to determine the grid nodes for the analytic solution to be applied, can be found in Appendix C. The monopole analytic solution is applied to this portion of the grid as an interior boundary condition. It should be noted that hybrid grids used in this work were, on purpose, of relatively poor quality regarding sound propagation. The ratio of monopole acoustic pressure amplitude to the medium pressure was in the order of 1×10^{-4}, which is similar to the case of aircraft engine sound propagation in the atmosphere. The artificial dissipation constant used for all cases presented was 1×10^{-4} [85].

Figure 4-2 shows the computed acoustic pressure contours. The acoustic pressure is normalized by the monopole source amplitude. The omnidirectional character of the acoustic field proves that monopole sound is propagated equally towards all directions of the hybrid grid.

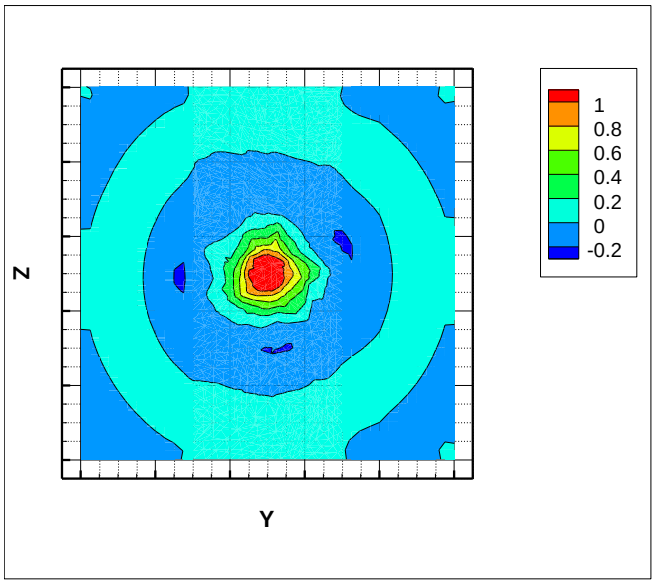

Figure 4-2: Monopole in a free field. Normalized acoustic pressure contours showing spherical symmetry in the YZ-plane.

Grid convergence study was performed for the hybrid grid showing that the method is capable of predicting the acoustic pressure variation (p') (Figure 4-3), and the acoustic amplitude (p'_0) attenuation away from the monopole source (Figure 4-4). It should be noted at this point that acoustic pressure variation (p') refers to the instant acoustic pressure at that point which varies in time, while acoustic amplitude (p'_0) refers to the maximum acoustic pressure amplitude at that point and it is constant in time. The number of grid points of the three hybrid grids used, were 1572 for the coarse grid, 8801 points for dense grid level 1 and 83399 points for dense grid level 2.

Normalized acoustic pressure values are plotted versus the non-dimensional distance kr, where k is the monopole's wavenumber, and r is the distance away from the monopole center [Figure 4-3 and Figure 4-4].

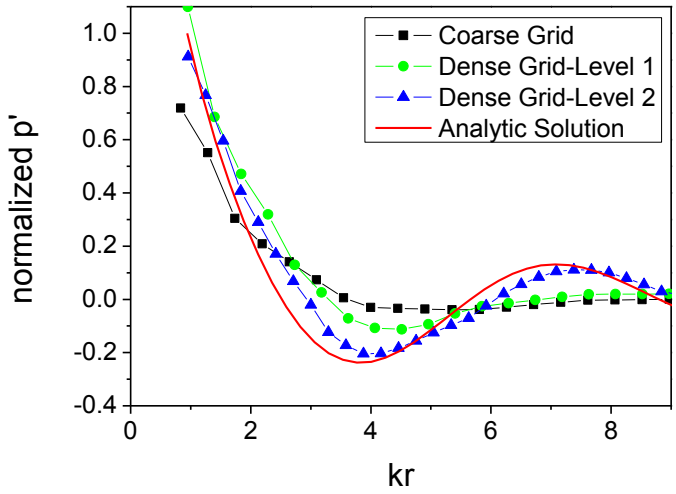

Figure 4-3: Grid convergence study of acoustic pressure variation for a monopole in free field.

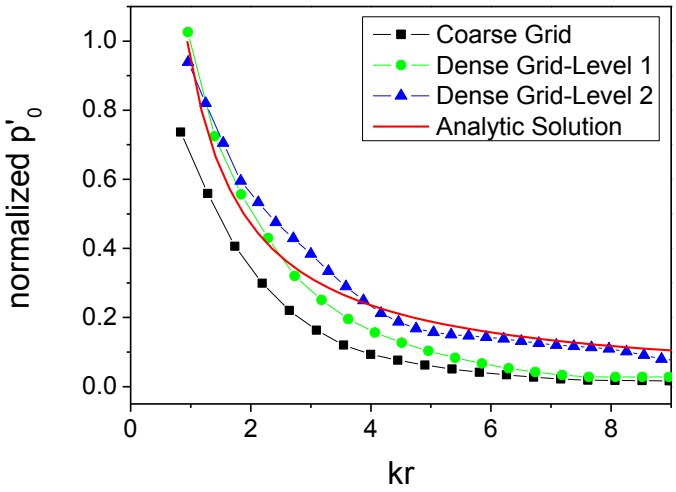

Figure 4-4: Grid convergence study of acoustic pressure amplitude attenuation for a monopole in free field.

Sound propagation in uniform flow

This section deals with the radiation of a monopole source in a subsonic uniform flow, a case whose analytic solution is known [88]. The monopole is again placed in the center of the hybrid grid used for the previous case, in a uniform flow of Mach number 0.3 in the positive *x*-direction. The acoustic waves propagate upstream and downstream with different velocities and their computed contours can be seen in Figure 4-5.

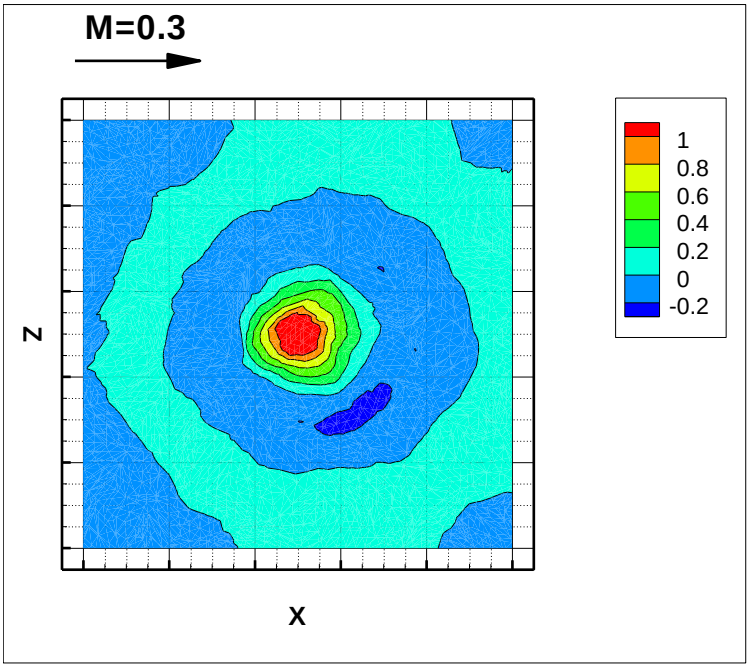

Figure 4-5: Monopole in a uniform flow field (M=0.3). Normalized acoustic pressure contours showing non-symmetric contours due to the flow.

The attenuation of the monopole's acoustic pressure amplitude is shown at a cut in the plane parallel to the flow and passing through the monopole in Figure 4-6. It can be observed that agreement to analytic solution deteriorates upstream of the monopole. This is attributed to the steeper gradients exhibited upstream, which would require a denser grid in order to improve the numerical solution.

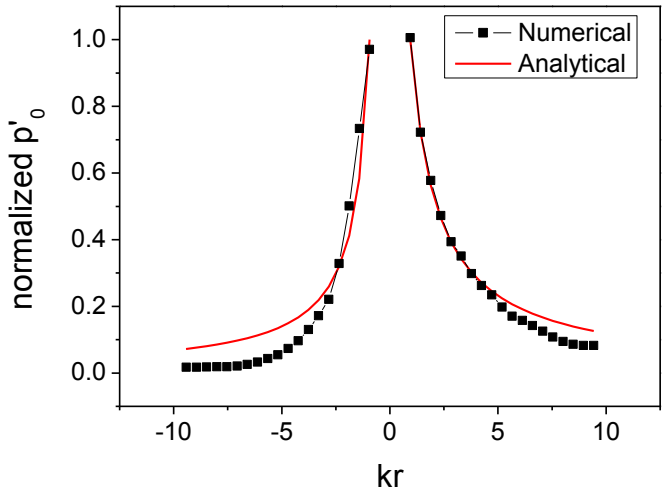

Figure 4-6: Comparison of analytic and computed acoustic pressure amplitude. Case of monopole in a uniform flow field (M=0.3).

SPL-based local adaptation

In this section the effectiveness of hybrid grid adaptation will be examined. On the challenges of grid adaptation with hybrid grids, see Ref. [89]. Initially, a monopole is radiating in a resting field using a coarse structured grid [Figure 4-7 (a)]. The Sound Pressure Level (SPL) values [88] of this case [Figure 4-7 (c)] are used for local grid adaptation resulting in a new hybrid adapted grid [Figure 4-8 (a)].

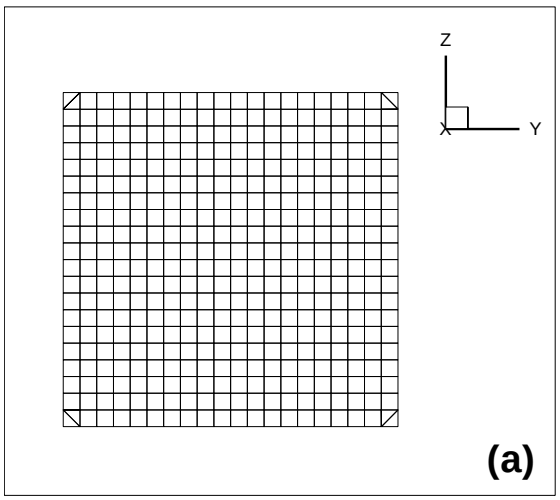

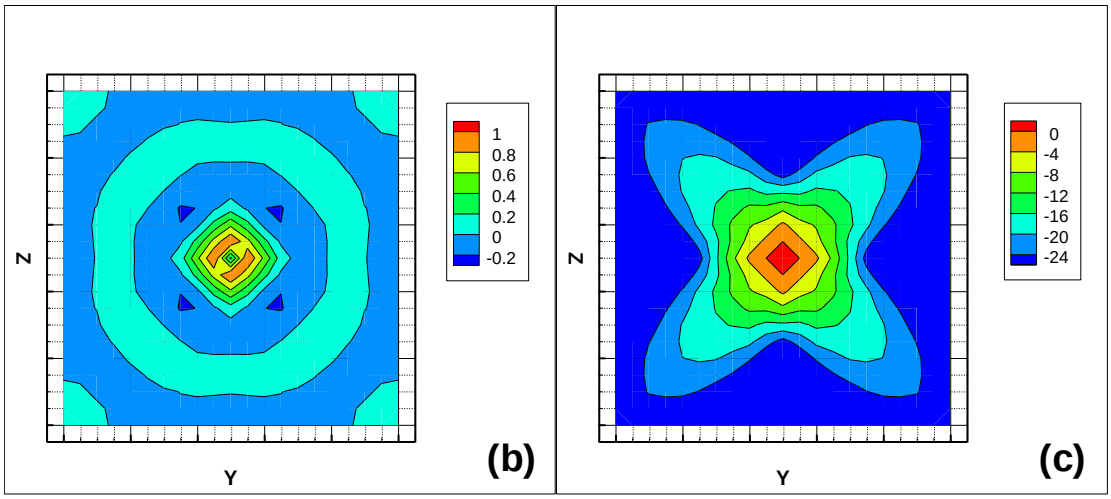

Figure 4-7: Monopole in a free field using a structured coarse grid: (a) grid used, (b) normalized acoustic pressure contours, and (c) SPL contours.

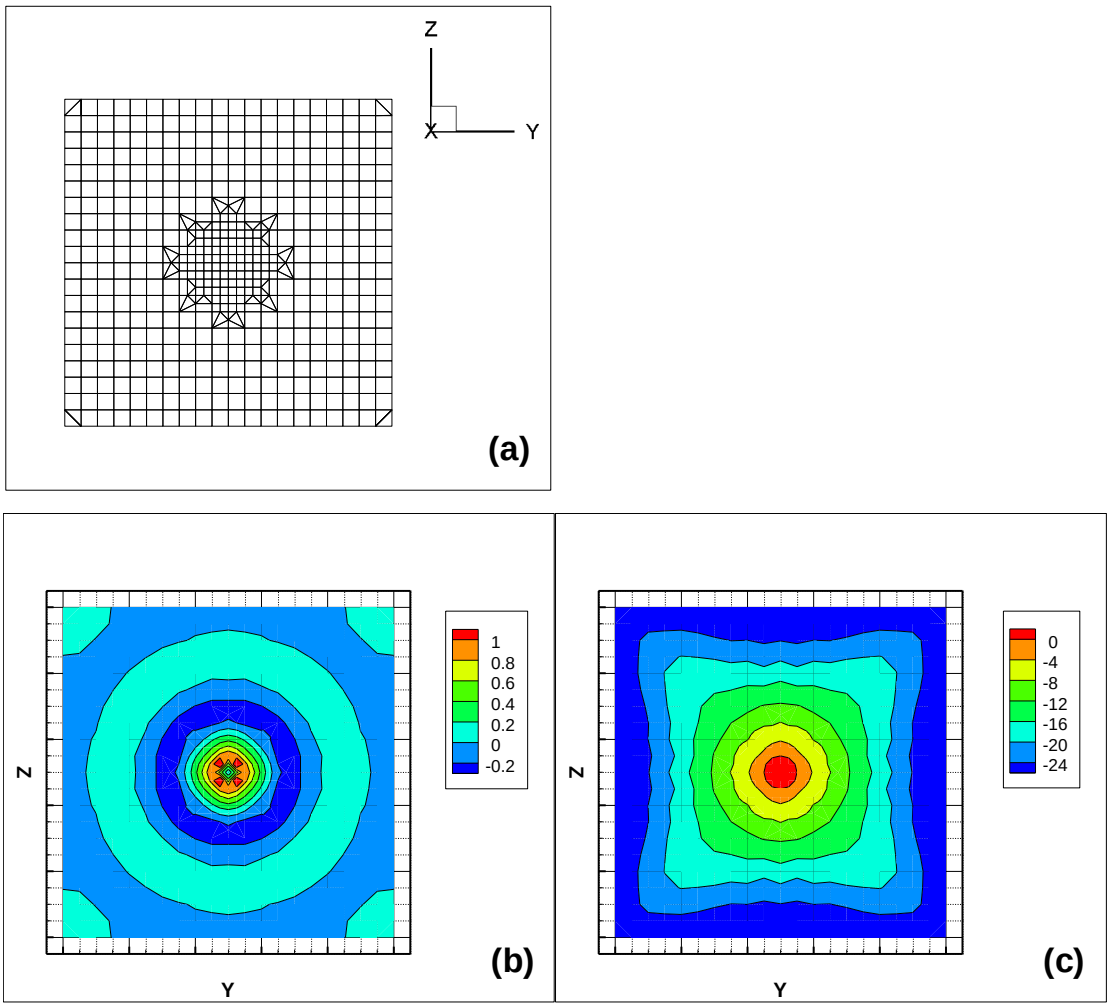

Figure 4-8: Monopole in a free field using an SPL-adapted grid: (a) adapted grid, (b) normalized acoustic pressure contours, and (c) SPL contours.

The new adapted grid improves the monopole propagation results significantly. Specifically, symmetry is improved as shown via comparison between Figure 4-7 (b) and Figure 4-8 (b). Also, the acoustic pressure variation, and acoustic pressure amplitude attenuation prediction is improved as evidenced from Figure 4-9 and Figure 4-10. Despite the fact that local adaptation extends only up to $kr = 4$, the solution improves beyond that point.

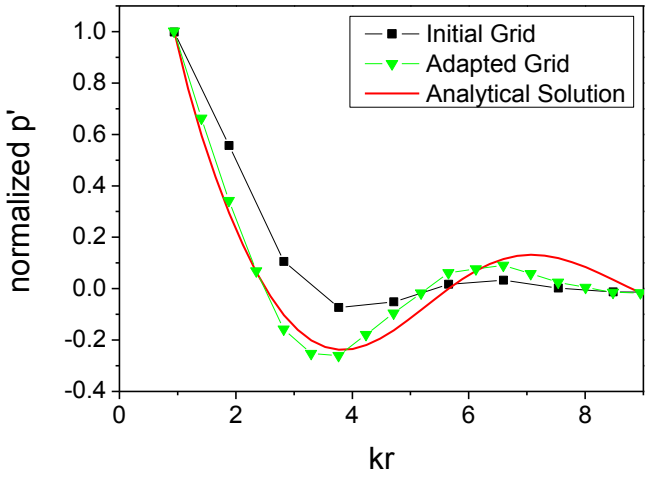

Figure 4-9: Improvement of prediction of monopole acoustic pressure variation using locally adapted grid. Case of a monopole radiating in a free field.

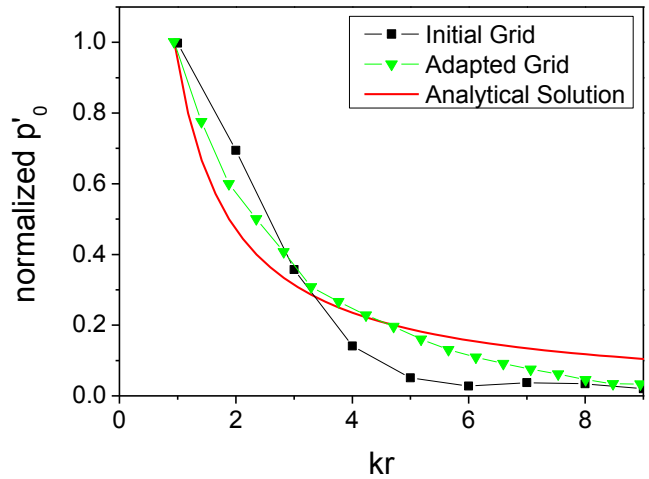

Figure 4-10: Improvement of prediction of monopole acoustic pressure amplitude attenuation using locally adapted grid. Case of a monopole radiating in a free field.

4.3.2 Sound Interaction with solid boundaries

In this section sound interaction with solid boundaries will be examined through sound reflection on a wall, as well as via diffraction on a rigid barrier, and a sphere.

Sound reflection on a wall

Another example of a known analytical solution concerns the incident and reflected waves due to radiation of a monopole near a plane wall [88]. This case is computed using the hybrid grid shown in Figure 4-11 (a), where the monopole is located above the wall (XZ plane). The acoustic pressure contours can be seen in Figure 4-11 (b). The acoustic amplitude distributed along a line passing through the source and which is perpendicular to the wall, is plotted in Figure 4-12. The comparison with the analytical values is quite good.

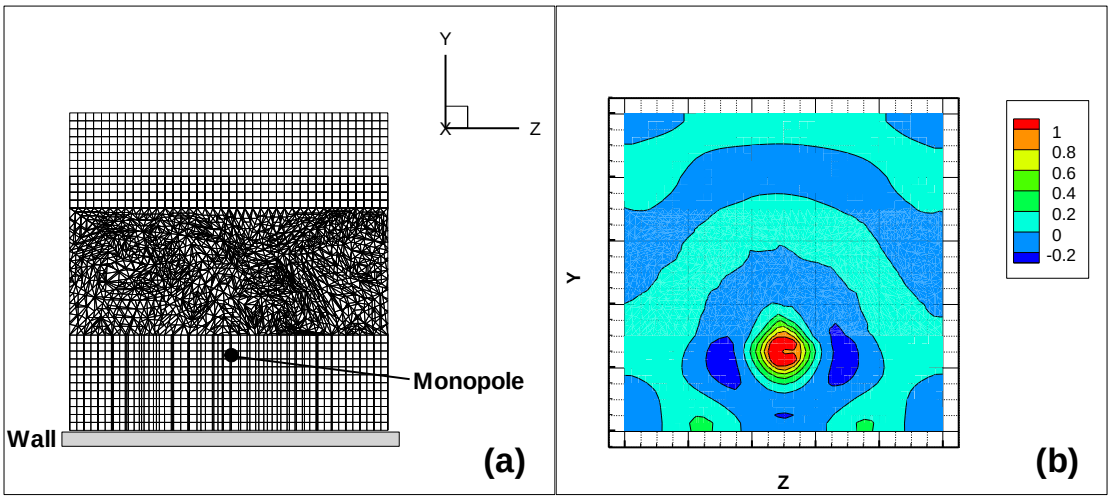

Figure 4-11: Monopole radiating near a plane wall: (a) hybrid grid cut showing wall and monopole position, and (b) normalized acoustic pressure contours.

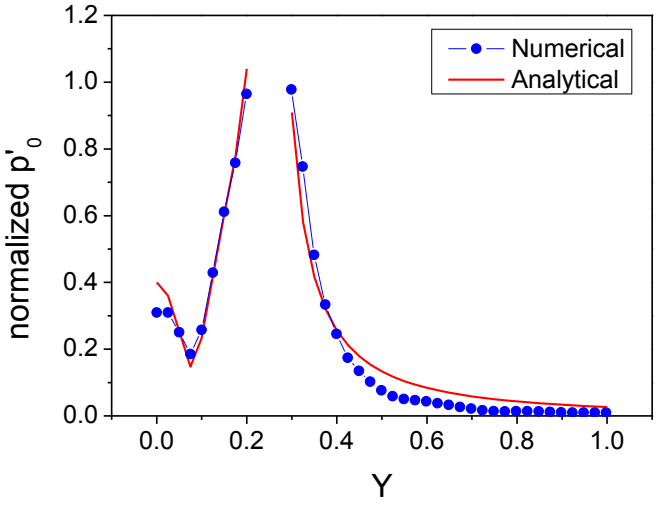

Figure 4-12: Comparison of analytical [88] and numerical solutions. Vertical distribution of pressure amplitude along a line perpendicular to the wall and passing through the monopole source.

Sound pulse diffraction by a barrier – The Friedlander solution

In this section the case of sound diffraction by a rectangular obstacle (barrier) of height *h* is considered. The problem geometry, as well as part of the describing hybrid grid (with 129774 grid points) can be seen in Figure 4-13. The flow field is at rest. The domain boundaries are all acoustic farfield except from the barrier. A sound step pulse is initiated at the left boundary and propagates throughout the domain being diffracted by the rigid barrier. This problem has an analytical solution described by Friedlander [90]. The comparison between the numerical results for points P_1 and P_2, which are located at distances of 0.3*h* in front, and 0.8*h* behind the barrier respectively, can be seen in Figure 4-14 and Figure 4-15. It is observed that the computational solution matches the analytical solution acoustic pressure levels pretty well at all phases and regions of sound propagation. As time passes, the computational solution converges to the analytical solution in both regions, showing that it resolves all existing waves, the incident, the reflected and the diffracted. It can also be observed that the current method predicts correctly both the amplitude and the arrival time of all the different waves that co-exist around the obstacle. The oscillations of the numerical solution are due to the central space discretization scheme.

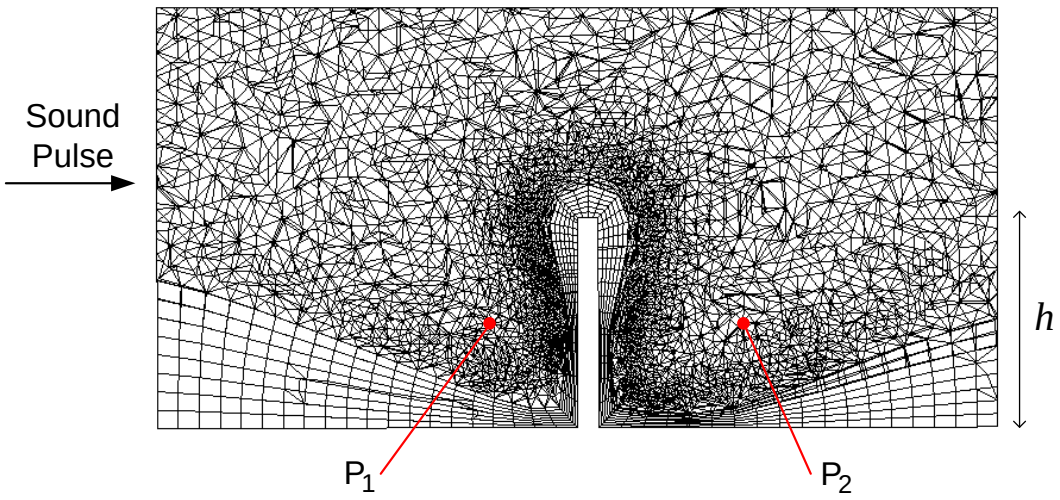

Figure 4-13: Slice of the hybrid grid used for sound pulse diffraction by a barrier. Points P_1 and P_2 are shown in front and behind the barrier, respectively.

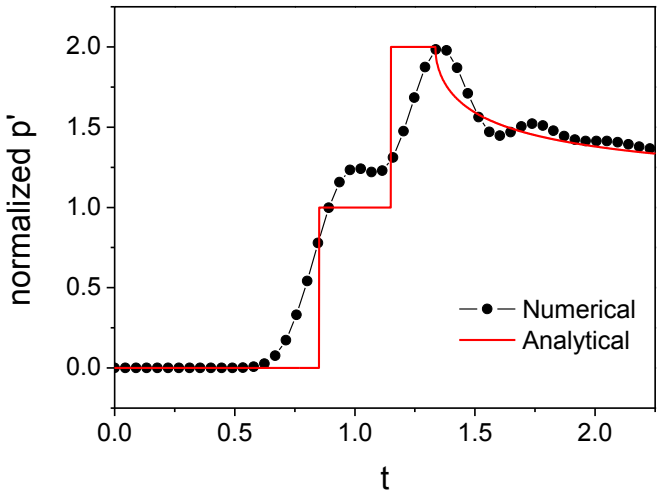

Figure 4-14: Case of a sound pulse diffracted by a barrier: Comparison of analytical [90] and computational solution at point P_1 in front of the barrier.

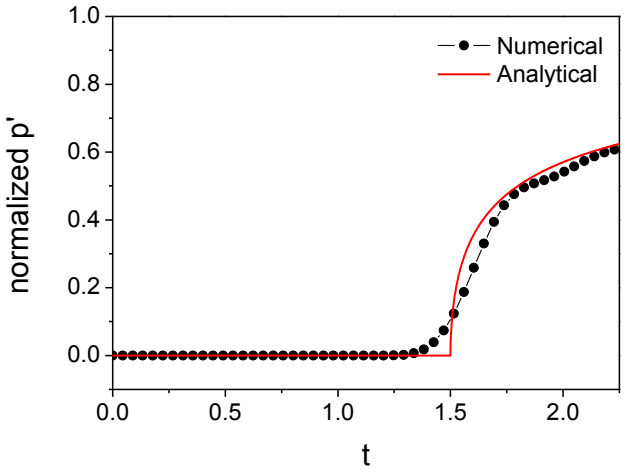

Figure 4-15: Case of a sound pulse diffracted by a barrier: Comparison of analytical [90] and computational solution at point P_2 behind the barrier.

Sound diffraction in non-uniform flow

The effect of a non-uniform flow field on the diffraction of monopole acoustic waves from a sphere is examined next. A sphere is placed in a flow of M=0.3 and a steady non-uniform flow field is created around the sphere [Figure 4-16(b)]. A monopole is then placed inside the flow field and above the sphere as seen in Figure 4-16(a). The number of points for the hybrid grid is 177964.

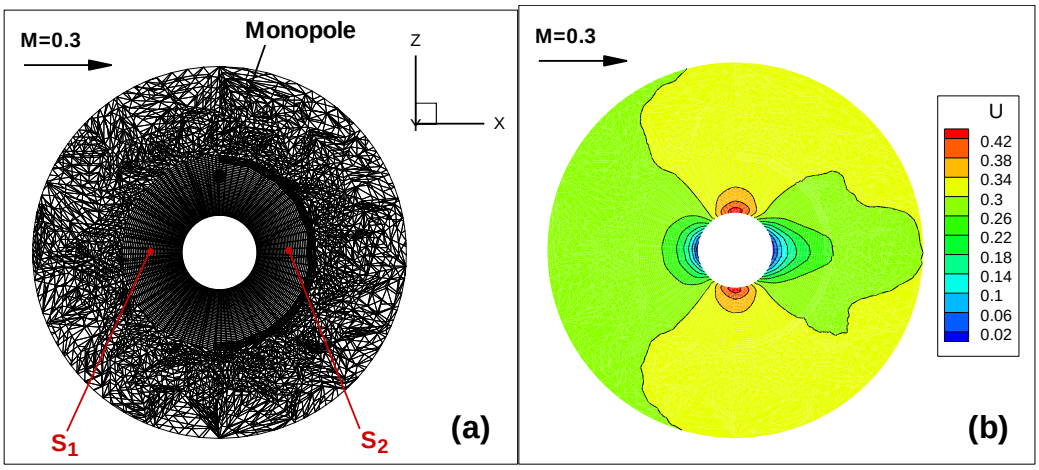

Figure 4-16: Case of monopole sound propagation in a flow of Mach 0.3 around a sphere: (a) hybrid grid cut indicating the monopole location, as well as the sound monitoring point locations S_1 and S_2, (b) u-velocity contours.

It is of interest to examine the effect of the flow field on the sound amplitude. To that extent, the acoustic pressure propagation through the fluid at rest, and through the non-uniform flow field, are compared. Two positions are considered for the comparison: the first is 1 sphere radius upstream [point S_1 in Figure 4-16 (a)], and the second is 1 sphere radius downstream [point S_2 in Figure 4-16 (a)]. The resulting plots can be seen in Figure 4-17. For the resting fluid case, the result at points S_1 and S_2 indicates the same pressure amplitude, as the flow field has no effect on sound propagation and diffraction. For the flow case, the solution at point S_1 (upstream) shows lower amplitude as the flow field inhibits sound propagation, while at point S_2 (downstream) it indicates higher amplitude as the flow field "favours" sound propagation. Moreover, the frequency of the monopole (3 cycles per time unit) is retained for all cases. The low-order model is able to capture the very significant effect of the flow field on sound propagation.

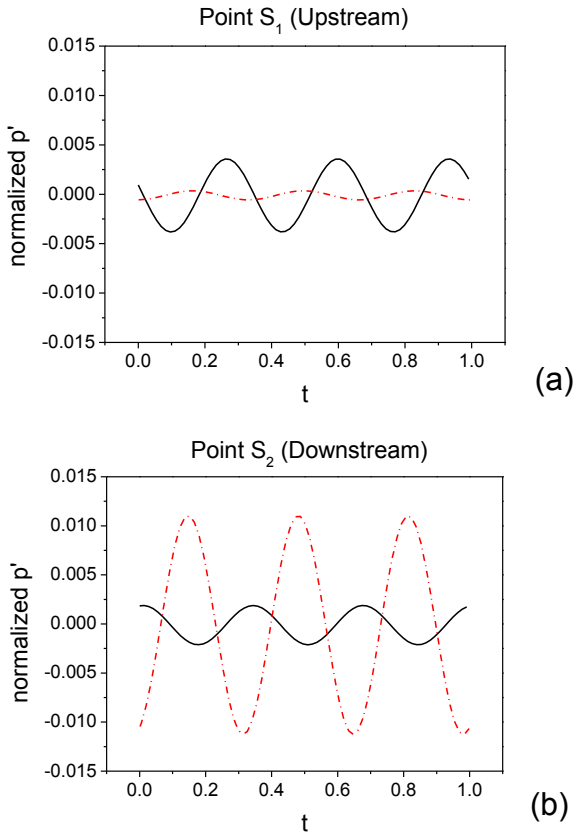

Figure 4-17: Comparison of the acoustic pressure for the cases of no flow (——) and flow (·····) around a sphere of M=0.3 at point S_1 upstream (a), and S_2 downstream (b).

4.3.3 Flow-Acoustics Coupling

The decomposition into two fields offers a simple way to compute each of them using the coupled system. The variation of the flow field in space and time influences sound propagation considerably. The next case involves diffraction of monopole source sound by a rectangular obstacle as shown in Figure 4-18. The obstacle's width is 0.2 times its height and the monopole location is 0.7 obstacle heights upstream of the obstacle. The following three cases are considered:

(i) $U_\infty = 0$ ("*no flow*"): the flow quantities are considered constant ($\rho = 1, P = 1/\gamma$), and only the acoustic field is computed.

(ii) $U_\infty = 0.3$ ("*static interaction"*): the flow field is computed until the vortex shedding behind the obstacle is fully developed (Figure 4-19). At that moment, all the flow quantities are held constant in time ("frozen" field), and the monopole source is introduced. For the rest of the simulation only the acoustic field is computed, while the fully developed flow field remains "frozen" for the purpose of testing the *static* flow-acoustics coupling.

(iii) $U_\infty = 0.3$ ("*dynamic interaction"*): the sound pulse begins at the same time as in the previous Case (ii), but the flow field changes in time and space until the end of the simulation.

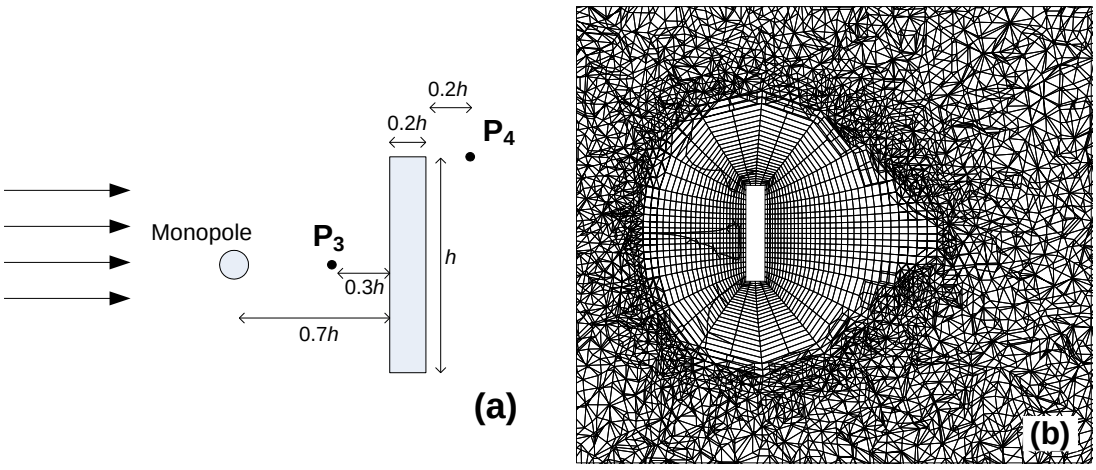

Figure 4-18: Flow past a rectangular 3D obstacle with a monopole source: (a) The points P_3 and P_4 are the points at which the acoustic pressure variation is monitored, and (b) hybrid grid cut at midspan.

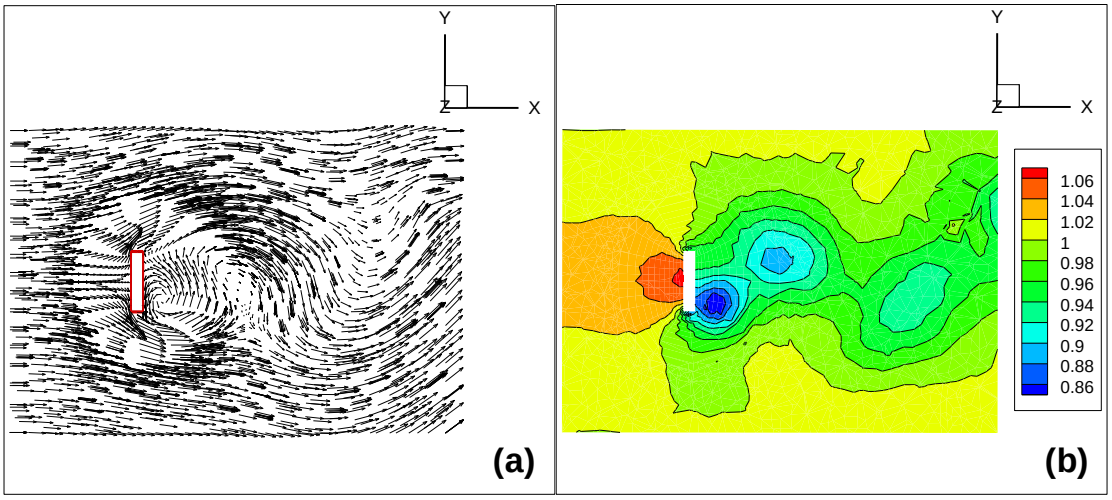

Figure 4-19: Unsteady, fully developed flow past the 3-D rectangular obstacle: (a) flow total velocity vectors on the XY-plane through the midspan of the obstacle, and (b) flow density contours.

In all the cases the computational grid was the same for both fields consisting of 146181 grid points. The inflow boundary was placed two obstacle heights upstream of the obstacle and the outflow boundary five obstacle heights downstream of the obstacle. The amplitude of the emitted sound (P_0) was three orders of magnitude smaller than the free flow pressure.

Comparison of sound propagation without flow and with unsteady flow

The computed acoustic pressure variation at the upstream point P_3 for the "*no flow"* case and for the *"dynamic interaction"* case can be seen in Figure 4-20. As expected, when the flow field is fully developed, it "favours" the propagation and amplifies the acoustic pressure levels experienced at point P_3.

The acoustic pressure variation at the downstream point P_4 is shown in Figure 4-21. This point is downstream of the obstacle and so the diffracted wave from the upper obstacle edge reaches it. It is observed that the flow field has a significant effect on the diffracted acoustic waves.

It can be seen that the role of the flow field in sound propagation is very important as indicated by this application of unsteady flow. The application of the flow/acoustics interaction method proposed here appears to handle the dynamic interaction between the two fields.

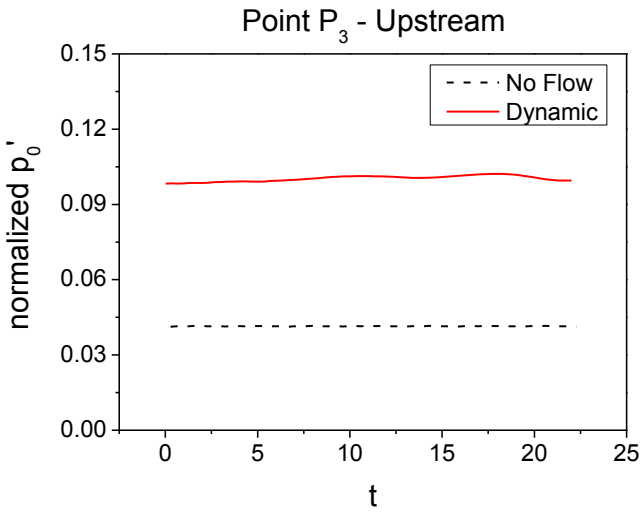

Figure 4-20: Monopole sound propagation past a 3D rectangular obstacle. Comparison of the normalized acoustic amplitude at point P_3 upstream of the obstacle for "no flow", and for "dynamic interaction" of the flow and acoustic fields.

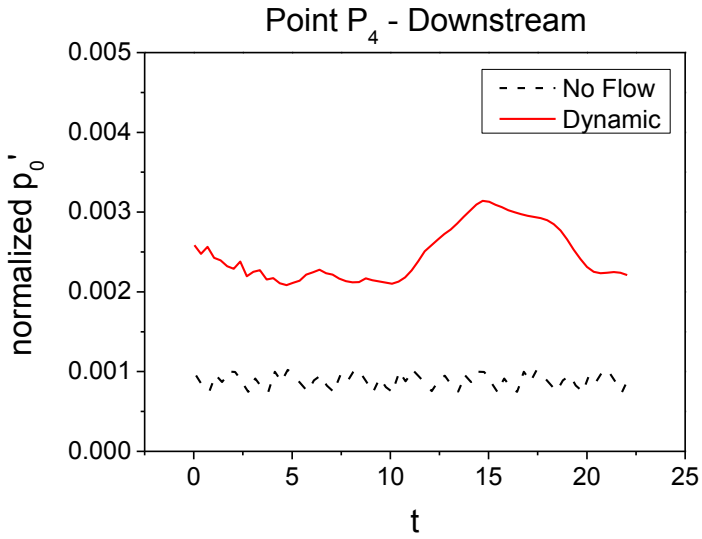

Figure 4-21: Monopole sound propagation past a 3D rectangular obstacle. Comparison of the normalized acoustic amplitude at point P_4 downstream of the obstacle for "no flow", and for "dynamic interaction" of the flow and acoustic fields.

Dynamic vs. static flow-acoustics coupling

In the previous section, it was shown that there are significant differences between sound propagation without flow and with flow. Here the sound propagation with a *fully developed* flow field that remains constant in time ("static interaction") will be compared to the sound propagation with the unsteady flow field examined in the previous section ("dynamic interaction"). In other words, the importance of capturing the dynamic interaction between the flow and acoustic fields will be evaluated as opposed to a static coupling between the two by keeping the flow "frozen" in time.

Figure 4-22 and Figure 4-23 show the acoustic pressure variation for both "frozen" and unsteady flow fields at points P_3 (upstream of the obstacle) and P_4 (downstream of the obstacle), respectively. One can see that where the flow is virtually in steady state, i.e. upstream of the obstacle, there is no difference in sound propagation between the static and the dynamic solution of the flow field (Figure 4-22). On the other hand, where the unsteady flow is significant, the acoustic solution is significantly different, as the diffracted waves travel at different speeds because of the difference in flow distribution downstream of the obstacle (Figure 4-23).

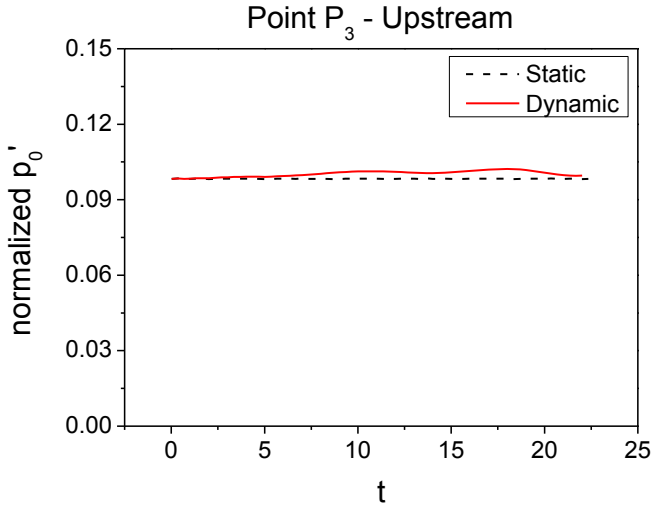

Figure 4-22: Monopole sound propagation past a 3D rectangular obstacle. Comparison of the normalized acoustic amplitude at point P_3 upstream of the obstacle for "static interaction", and for "dynamic interaction" of the flow and acoustic fields.

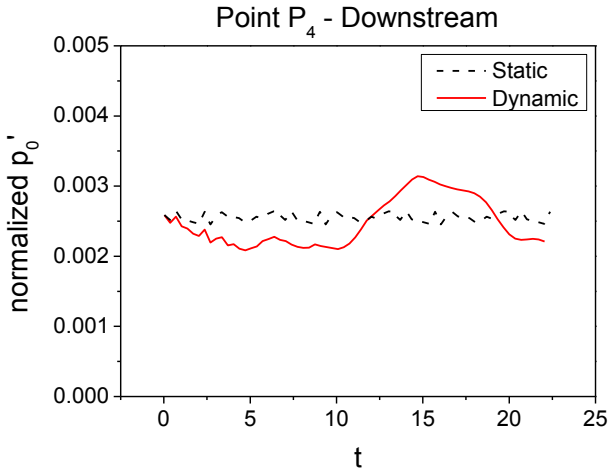

Figure 4-23: Monopole sound propagation past a 3D rectangular obstacle. Comparison of the normalized acoustic amplitude at point P_4 downstream of the obstacle for "static interaction", and for "dynamic interaction" of the flow and acoustic fields.

In Figure 4-24 the acoustic pressure distribution can be seen for the acoustic waves interacting with the unsteady flow field. The diffracted waves from the obstacle edges are observed as they meet behind the obstacle.

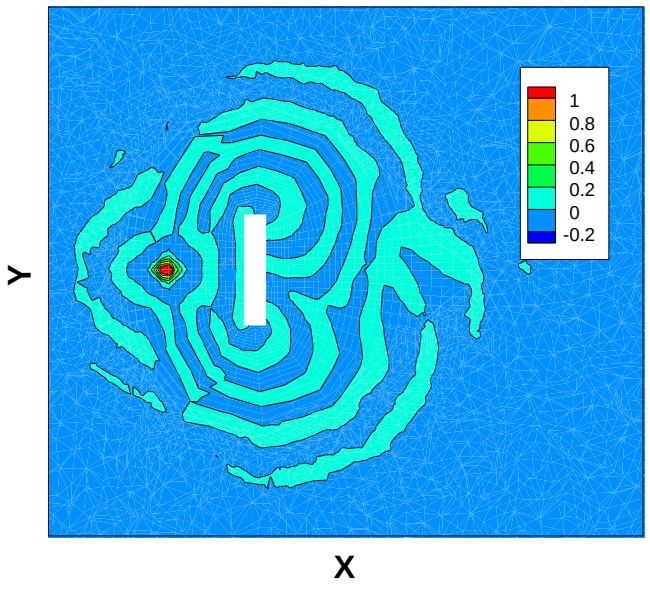

Figure 4-24: Monopole sound propagation past a 3D rectangular obstacle. Contour lines of the normalized acoustic pressure for sound propagation interacting with an unsteady flow field.

4.4 Application for the case of a conventional airplane

The flow interaction method developed in the previous paragraphs is applied to the realistic problem of an air vehicle. The aim of this paragraph is to demonstrate the effect of the flow field and wing shielding on the acoustic levels of a conventional airplane and provide proof of concept for the method developed in the previous paragraphs. For this reason, the airframe geometry of a Boeing 777 is selected being representative of modern airliners [Figure 4-25].

Figure 4-25: Boeing 777-300ER

Before moving into the investigation results, the errors that are encountered in the following computations are referenced:

- Computational errors. The grid used for the aeroacoustic simulations is the same as the flow grid. This offers speed and simplicity, but introduces dissipation and dispersion errors. Boundary conditions also introduce time accuracy computational errors.
- Engine noise modelling errors. The aircraft jet engine noise is determined to be of quadruple nature and characterized by strong directivity, however in the following simulations it was modelled as an omnidirectional monopole. This monopole has approximately the size of the jet engine inlet, with no nacelle

being present. Its placing above the wing, for the shielding investigation, is not a realistic configuration, but is used for comparison with the reference case.

- Monopole orientation errors. Orienting the monopole surface grids in a hybrid mesh results in a surface approximation which can deviate significantly from the spherical shape. This deviation affects the omnidirectional character of the monopole source.

Due to the above limitations the results presented in the following paragraphs are not quantitative, but qualitative only.

4.4.1 Effect of flow field on SPL levels

When a flow field is added to the still air, it affects sound propagation by altering the wave propagation speed and by the introduction of refraction effects. This is the case of a flow around an aircraft, where the complex flow field has a significant effect on the engine's acoustic levels.

In order to demonstrate this phenomenon, the case of a Boeing 777 in a flow of 0.3M is examined. The grid used for the flow field as well as the flow pressure distribution on the aircraft airframe can be seen in Figure 4-26. The hybrid grid is consisting of prisms, used for the boundary layer, pyramids, and tetrahedra and has a total number of 152549 points. The complete flow solution was provided by the 3D inviscid flow solver described in section 4.2. All flow and acoustic runs of this paragraph were performed on the half symmetric grid and the solution is mirrored in order to give the full view of the aircraft.

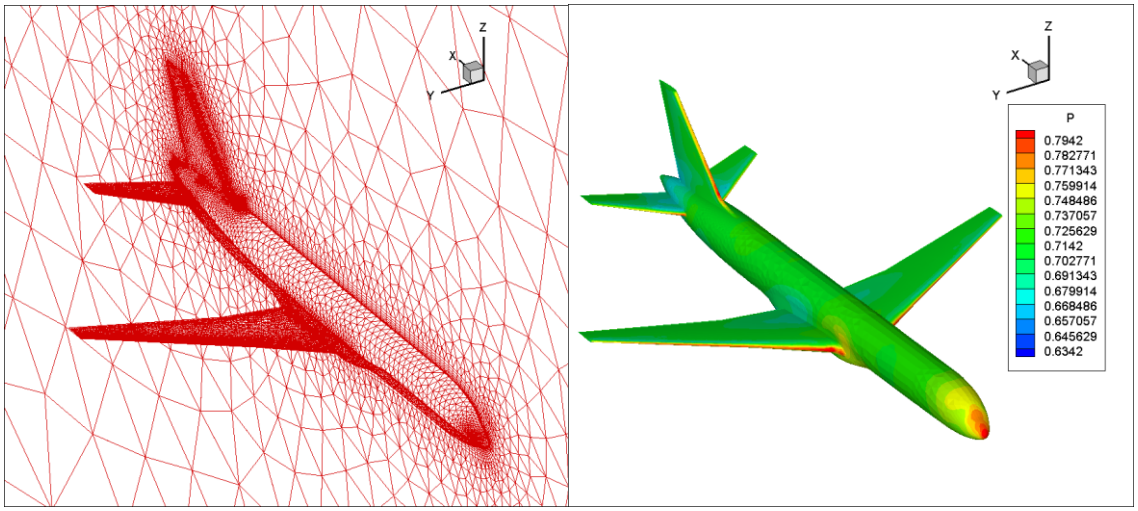

Figure 4-26: Hybrid grid [left] and flow pressure contours [right] on the aircraft surface for M=0.3

As it has already been stated, the hybrid grid used for the flow solver is also used for the acoustic solver and for all the examined cases in this thesis, the engine is modelled as a point monopole. The monopole orientation algorithm is applied determining the monopole surface nodes where the analytical solution is applied. Its radius approximates that of an actual aircraft engine and its acoustic pressure amplitude corresponds to about 120 dB.

The fuselage-engine configuration examined in this case is the "Under the Wing Nacelle" (UWN) configuration where the engines are placed below and in front of the wing. This is the most usual configuration of aircraft used in air transport.

The precise monopole position that models the engine for the UWN case can be seen in Figure 4-27. Its shape is not perfectly spherical due to the hybrid mesh used to describe it.

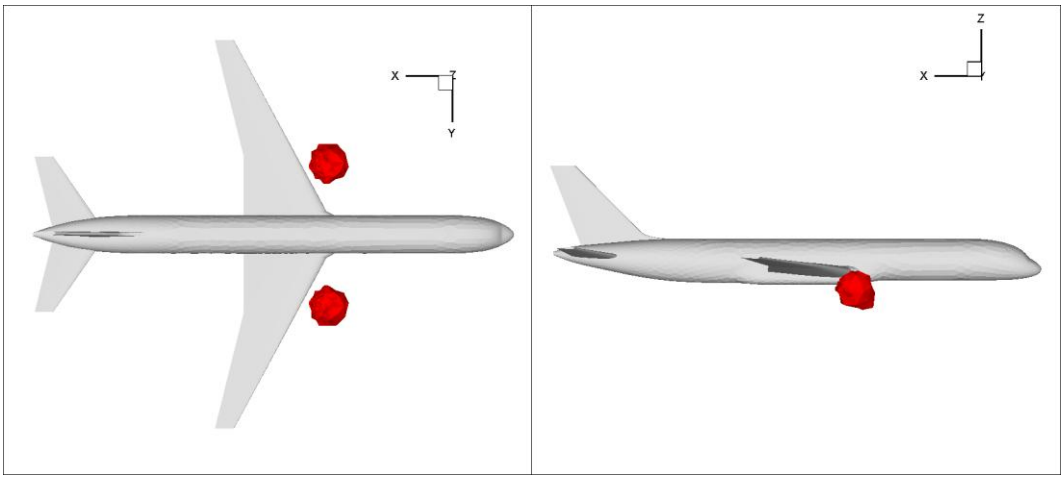

Figure 4-27: Monopole source position for the UWN case, top view (left), side view (right).

In order to examine the flow field effect on the engine noise levels, the acoustic solver is run for the case of the aircraft in steady flow("no flow case") and the aircraft in a flow of 0.3M ("flow case"). The SPL qualitative levels on the aircraft fuselage can be seen in Figure 4-28 for both cases. A displacement of the maximum SPL levels streamwise can be observed for the "flow case".

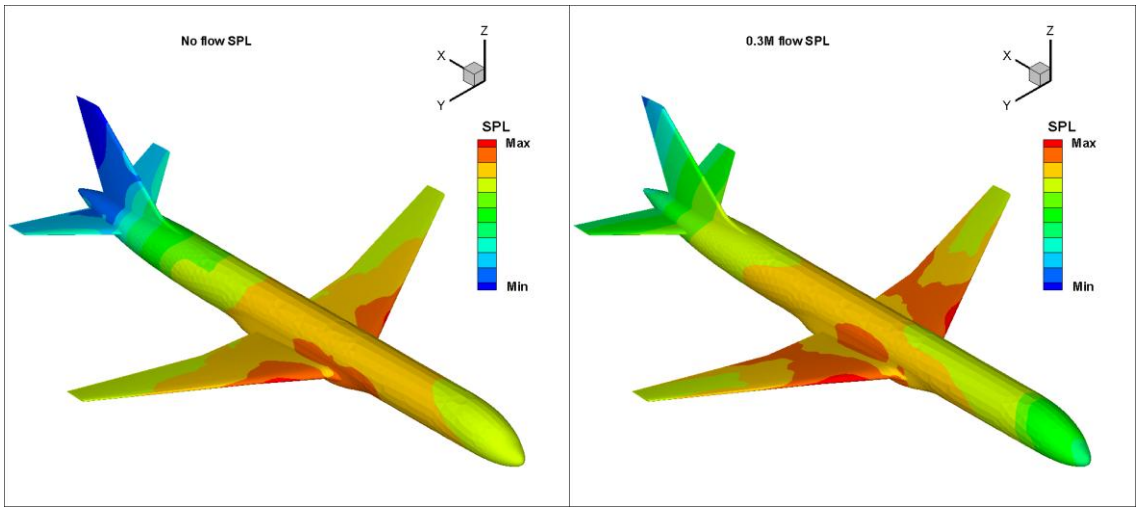

Figure 4-28: SPL contours on the aircraft surface for the UWN configuration: no flow case (left) and flow case (right).

The effect of the flow field can be isolated by subtracting the "no flow case" SPL levels from the "flow case" levels.

$$DSPL=SPL_{flow}-SPL_{noflow}$$

The results on the aircraft fuselage are seen in the left part of Figure 4-29.

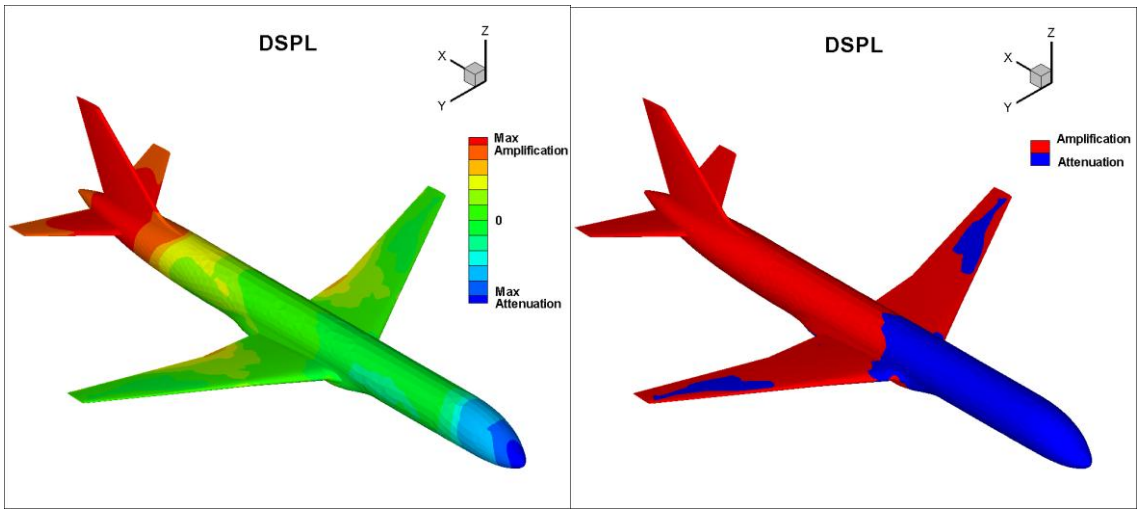

Figure 4-29: DSPL levels on aircraft fuselage (left) and amplification/attenuation regions (right).

It can be observed that:

- The effect of the flow field amplifies engine sound levels at the aft part of the fuselage with maximum amplification levels encountered at the tail section.
- On the fore part of the fuselage the sound levels are attenuated, with maximum attenuation seen at the cockpit region.
- In the right part of Figure 4-29 the amplified and attenuated regions can be clearly distinguished. As expected, the separating line is on the longitudinal position of the engine, where the fore region is attenuated as the flow direction is opposite to sound propagation, while aft region is amplified as flow favours sound propagation. In the same figure, the isolated attenuated regions seen on the outer part of the aircraft wings are regions which are reached only by the diffracted sound field. It seems that the flow field attenuates the diffracted sound field at that part of the wing.

Besides the effect on the fuselage sound levels, flow field also affects the emitted sound. The acoustic signatures for the flow and no flow case, 10 meters below the aircraft fuselage can be seen in Figure 4-30. A change of the local maximum shape can be clearly observed, being spread to the downstream region of the aircraft.

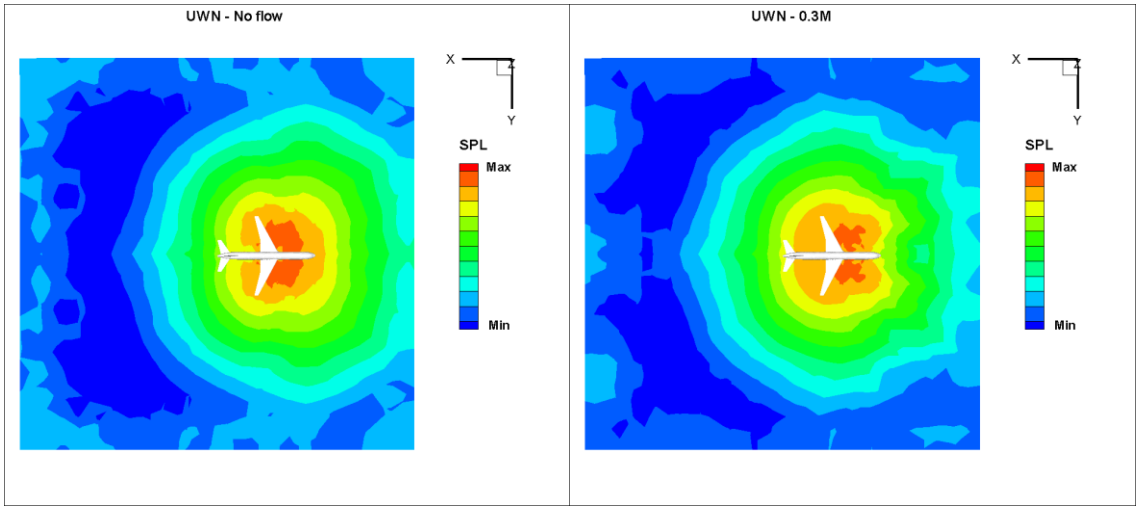

Figure 4-30: SPL signatures 10 meters below the aircraft fuselage, for the no flow case (left) and 0.3M case (right).

The effect of the flow field on the acoustic signatures can be isolated by plotting the DSPL values at the 10m below the fuselage level [Figure 4-31].

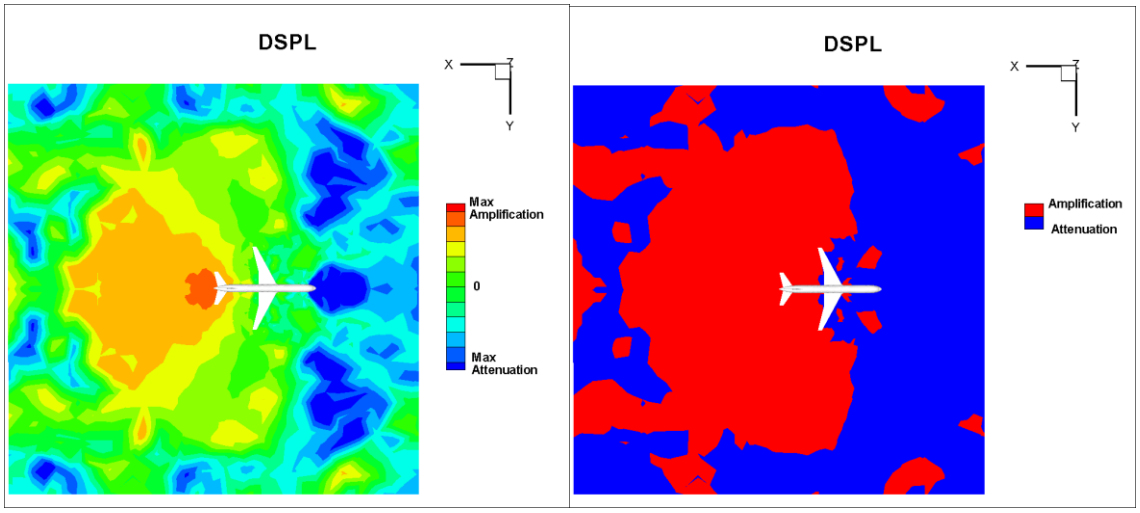

Figure 4-31: Effect of flow field on acoustic levels. DSPL signatures 10m below aircraft fuselage (left) and amplification/attenuation regions (right).

It can be observed that:

- The effect of the flow field amplifies sound levels behind the aircraft.
- In front of the aircraft the SPL is attenuated due to the flow field.

In Figure 4-31 (b) the amplified and attenuated regions can be clearly seen. As expected, the separating line is roughly on the longitudinal position of the engine, where the fore region propagation is attenuated as the flow direction is opposite to sound propagation, while aft region propagation is amplified as flow favours sound propagation. The small amplification and attenuation regions of arbitrary shape seen close to the aircraft fuselage are attributed to the effect of flow on the reflections from the fuselage body, while those seen at the boundaries of the computational domain are expected to be numerical errors and are not taken into account.

4.4.2 Effect of wing shielding on acoustic signature

In order to reduce the emitted noise, the concept of shielding the engine noise using the wing or other parts of the fuselage has been proposed in many novel aircraft configurations. For the Over the Wing Nacelle (OWN) configuration, the engines are placed above the wing in order to reduce the noise emitted below the aircraft.

In the present case the OWN configuration will be examined for a conventional aircraft and compared to the reference case of UWN. In fact the OWN concepts except from the engine displacement, also include significant modifications in the aircraft's airframe, however for the following case the aircraft geometry remains the same. The precise monopole position that models the engine for the OWN case can be seen in Figure 4-32.

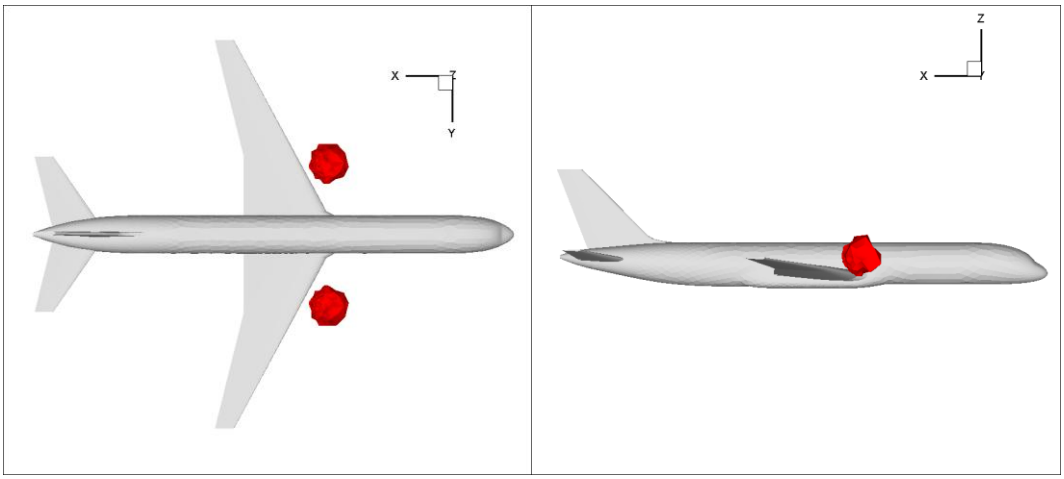

Figure 4-32: Monopole source position for the OWN case, top view (left), side view (right).

The SPL signatures of the OWN case, on a level 10 meters below the fuselage, and how they compare to the UWN case, can be seen in Figure 4-33 for both flow and no flow case.

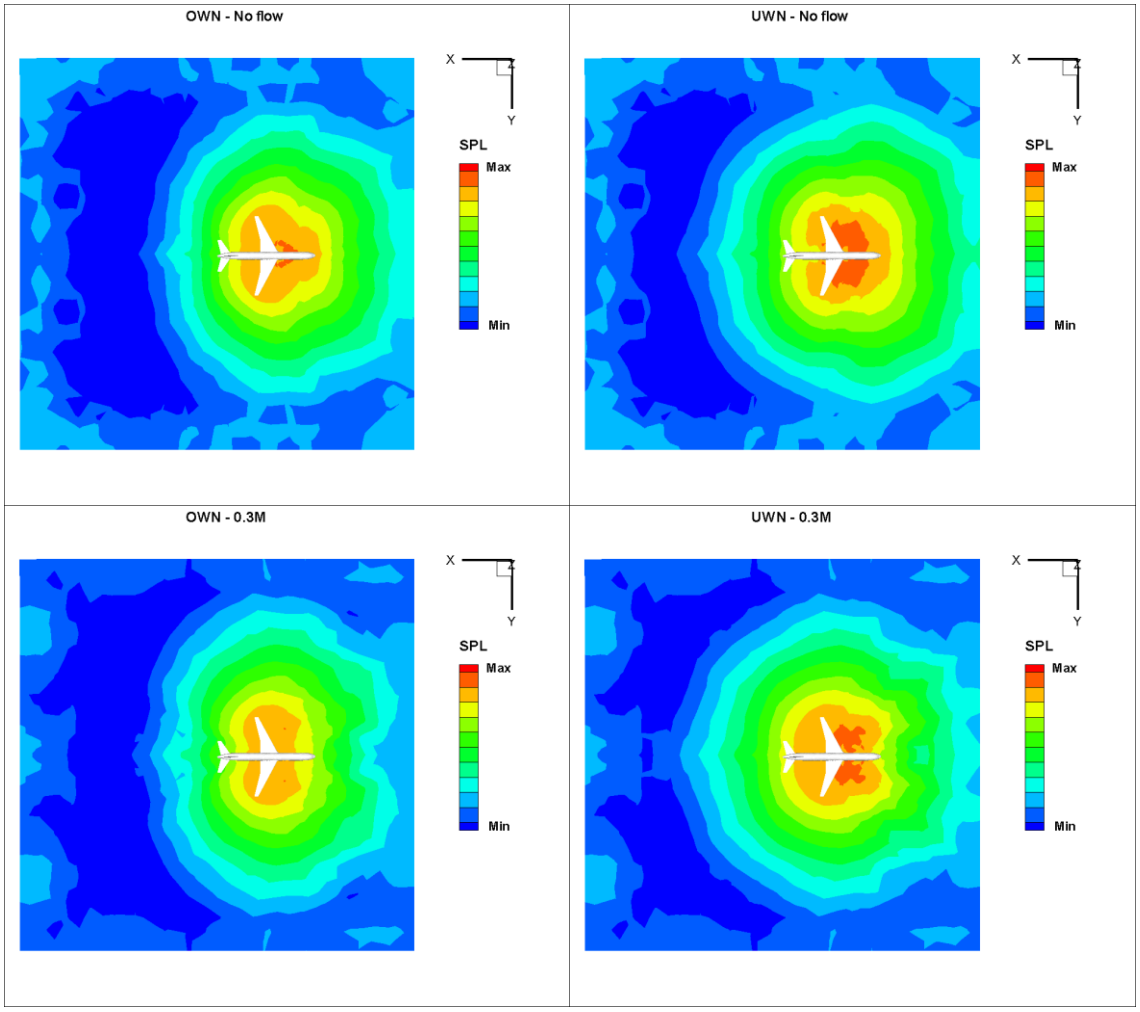

Figure 4-33: SPL signatures 10m below aircraft. Over the Wing Nacelle case (left) and Under the Wing Nacelle case (right).

It can be observed that:

- The lower SPL levels seen for the whole region below the aircraft for the OWN case prove the effectiveness of wing shielding.
- The effect of the flow field is similar for both cases, moving the SPL signature downstream, as it was also shown in the previous paragraph.

The effect of the wing shielding can be isolated using DSPL values, that result by subtracting the UWN SPL levels from the OWN levels.

$$DSPL=SPL_{OWN}-SPL_{UWN}$$

The results are seen on two different levels: (i) 10 meters below and (ii) 20 meters above the aircraft fuselage, for the no flow case (Figure 4-34) and the 0.3M flow case (Figure 4-35) respectively.

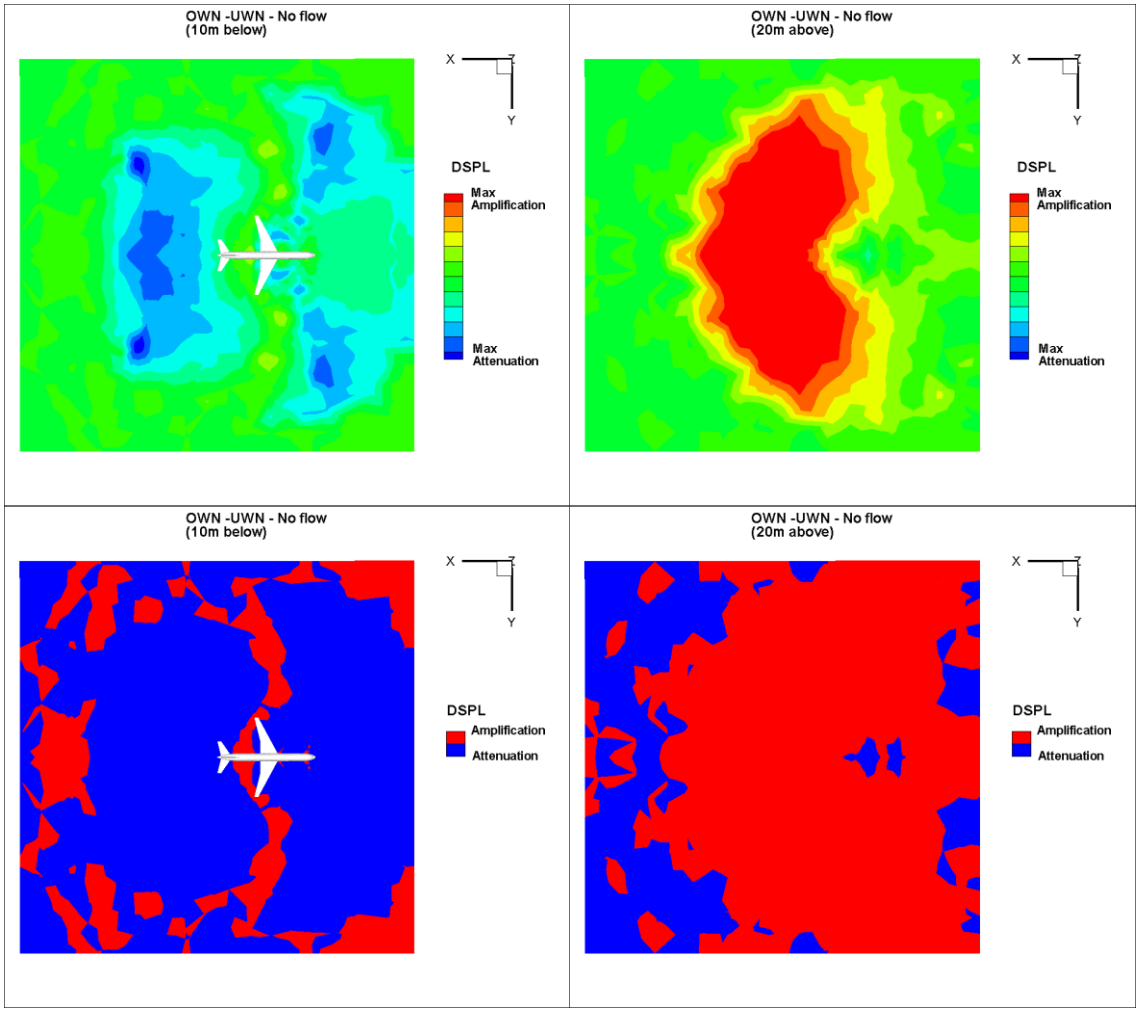

Figure 4-34: Effect of wing shielding on DSPL contours below and above the aircraft for the "no flow" case. DSPL signatures below (left) and above aircraft (right).

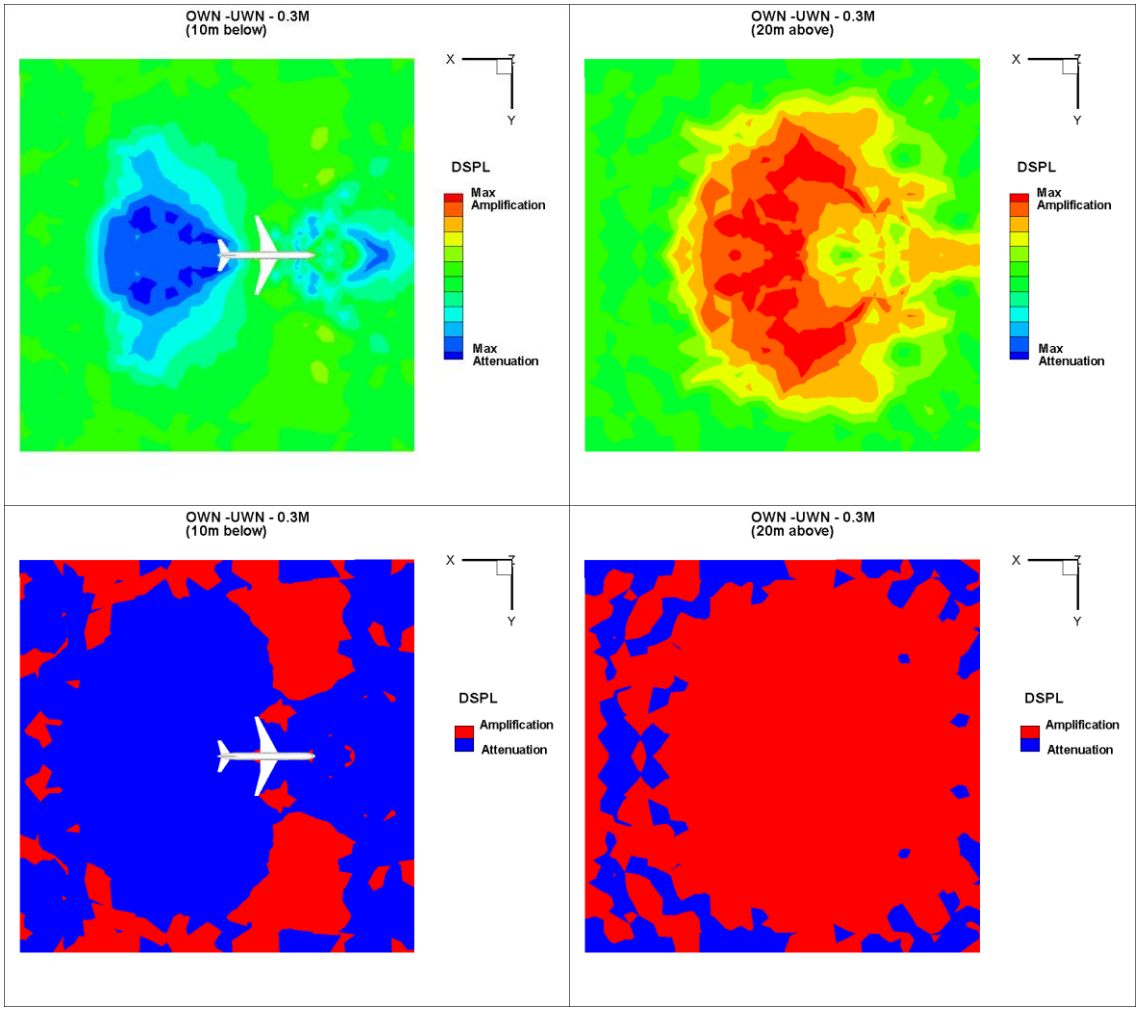

Figure 4-35: Effect of wing shielding on DSPL contours below and above the aircraft for the 0.3M flow case. DSPL signatures below (left) and above (right) aircraft.

It can be observed that:

- Noise levels below the aircraft are attenuated for the OWN case. The downstream attenuated region for both no flow and flow case can be attributed to wing shielding effect. Figure 4-36 (a) shows the approximate noise propagation direct path that is blocked by the wing resulting in the attenuated levels at the downstream lower region. The mixed behaviour of the upstream region is attributed to added reflected-on-the-fuselage paths [Figure 4-36 (b)].
- Noise levels above the aircraft are amplified for the OWN case. Placing the engine above the wing has the opposite results for the region above the aircraft. This is attributed to the added reflections, as well as the vertical displacement of the engines which brings them closer to the 20m level. Figure 4-36 (c) shows the

engine noise propagation reflected path which is added and strongly affects the region above the aircraft.

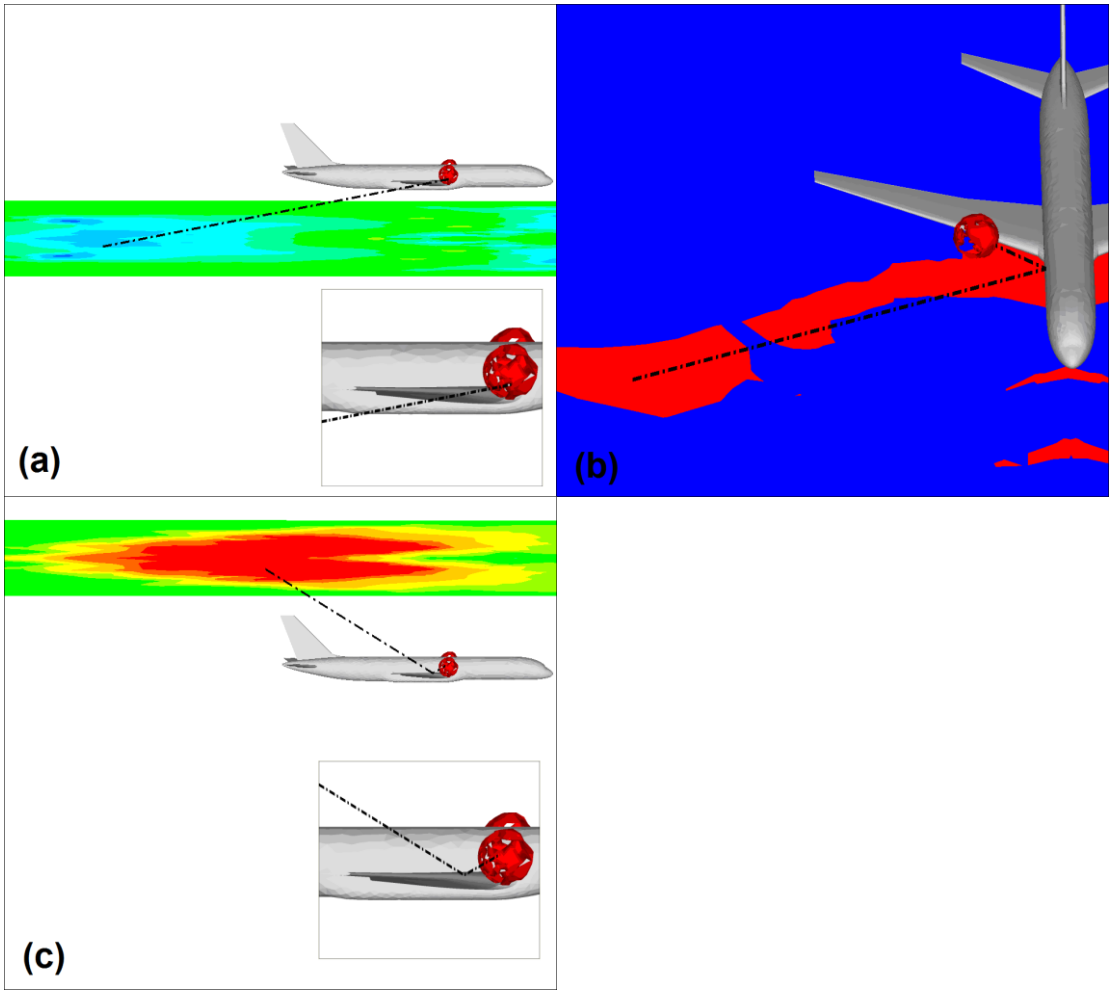

Figure 4-36: Engine monopole propagation direct path blocked by the wing (a) reflected path added on the fuselage (b) and reflected path added by the wing (c) for the OWN case.

5 Investigation of BWI noise in descent flight

Despite the fact that the main scope of this thesis regards far field and near field air vehicle propagation issues, the extensive analysis of the available experimental database provided some interesting results on the mechanism of rotor BWI noise. Though the research objectives of the HELISHAPE test did not initially include broadband noise studies, the microphones and blade pressure transducers used were of high enough sampling rate to allow BWI noise analysis.

BWI noise has been mainly investigated during take-off flight conditions, while descent flight conditions have been overlooked due to the dominance of BVI noise. Moreover the exact mechanism of BWI noise has not been yet exactly determined, while various models have been suggested. The main objective of the present chapter is to examine the importance of BWI noise in descent flight and propose the most appropriate model for these flight conditions.

Initially, in the following paragraphs, BWI noise history and the suggested mechanisms are briefly outlined, providing the state-of-the-art on BWI noise. The acoustic pressure waveforms are then analyzed and BWI acoustic contribution is determined using appropriate filters. Furthermore, the acoustic data are used to determine the location of the dominant BWI region on the rotor disk and compare it to other studies. Coherence analysis is applied to blade pressure data in the specified rotor disk region in order to identify any dominant frequencies in terms of Struhal number, as well as the existence of acoustic dipoles. The Laser Light Sheet (LLS) flow visualization data are also examined in order to detect turbulent flow structures, other than tip vortices, encountered by the blades during their rotation. Finally, the effect of blade-tip shape on BWI noise is briefly outlined by comparing the results of the rectangular blade-tip to those of a swept-back parabolic blade-tip.

5.1 BWI noise history and suggested mechanisms

BWI noise was initially identified by Brooks et al. [6,91] as the dominating noise source for the mid-frequency range in the absence of BVI activity. After a series of wind tunnel tests on model scale rotors, Brooks et al. concluded that broadband rotor noise is generated by the interaction of the rotor blades with the turbulent portion of the wakes of the preceding blades and not to naturally occurring atmospheric turbulence as previously thought. Based on the suggested connection of BWI noise to trailing vortices of the preceding blades, Glegg [92] built a prediction model for BWI noise based on the blade response function of Amiet [93]. This model assumed that the noise was generated from interactions between the blades and turbulence contained in tip vortices. Since the characteristics of a rotor's vortex turbulence were not available, the later was modelled as being isotropic and homogeneous and was taken by 2-D wake measurements. The model's input parameters were rotor wake results and estimations of the wake's turbulence parameters (intensity and length-scales). The results indicated that the turbulence contained in an isolated vortex could not account for BWI noise levels and spectral shape, thus suggesting that large-scale structures might be the dominant feature of the flow responsible for this noise source. In order to define the increased turbulence energy contained in the interacting turbulence, Wittmer et al. [94] searched for other mechanisms of turbulence production inside trailing vortices. They examined the interaction of a streamwise vortex and a spanwise blade in a windtunnel in terms of detailed velocity and turbulence measurements for a range of blade-vortex separations. They showed that perpendicular blade vortex interaction substantially alters the flow and produces a much larger and more intense region of turbulent flow than that presented by the undisturbed vortex. Glegg et al. [95] modified Glegg's model to account for the observations of Wittmer et al. [94] and assumed that only interactions with vortices which have already interacted with a blade should contribute to BWI noise. The new prediction model altered the turbulence parameters, the contributing vortices, and included improved rotor wake results. Their model's results provided a fine prediction of the experimental data spectral shape, but tended to underpredict the overall level.

In order to avoid the use of turbulence characteristics needed in the prediction models, Brooks et al. [96,97] used the measured blade pressure measurements to predict BWI noise. Analysing and presenting the experimental data from the HART [5] test, the blade response coherence functions were determined using cross-correlation methods for different pressure locations on the blade. These functions were implemented in a formulation of Amiet [93] and by accounting for Doppler and convection effects, their model succeeded to predict the directivity and spectral levels for a large range of flight conditions. This method was also combined with a "self" noise prediction method, in order to obtain results for the wide frequency range of rotor broadband noise [98,99] and it showed good agreement to all flight cases of the HART test.

Another analysis of the HART database was done by Brezzilion et al. [100], who analyzed acoustic and blade pressure data for various flight conditions. Their study confirmed the connection of BWI to perpendicular interactions of the blade with tip vortex turbulence. However, they concluded that interactions with parts of the rotor wake other than tip vortices also contribute to BWI.

A third study on HART experimental blade pressures done by Bouchet and Rahier [101] highlighted some characteristics of the turbulence responsible for BWI noise. Using a variety of signal analysis methods, they demonstrated that BWI was not related to blade interactions with isotropic turbulence, but rather to coherent large-scale structures present in the flow. Their study connected the resulting turbulence spectral characteristics to flow structures produced by the interaction of co-rotating wing tip vortices [102].

Based on Bouchet and Rahier results, a recent study of Mauffrey et al. [103] examined the connection of elliptic instabilities [104,105] to BWI noise. These instabilities are formed when two close tip vortices interact with each other in the beginning of the process which eventually leads to the merging of the vortices. Elliptic instabilities are characterized by a sinuous deformation of each vortex in two parallel planes. According to this mechanism, BWI noise results from the perpendicular interaction of the blades with elliptically deformed vortices. Mauffrey et al. [103] performed a numerical simulation of these instabilities in take-off flight conditions and comparing to HART data, observed good agreement in terms of noise levels and directivity.

Even if significant advances in the prediction of BWI noise have been demonstrated, the exact mechanism of BWI is not clear. Most studies on this type of broadband noise address the lack of information and understanding of the origin and development of turbulence in vortical flows.

The studies of Brooks and Burley [96,97], Brezzilion et al. [100] and Bouchet and Rahier [101], are studies on BWI noise that have been based on acoustic and blade pressure measurements' analysis. These studies were all based on HART experimental results, while the case of descent flight conditions has received less attention due to the relative smaller importance of BWI noise in the acoustic spectrum. Despite its smaller importance, it is seen in the HART acoustic spectrum results (Figure 5-1) that the descent case experiences the greater BWI spectrum levels compared to the other conditions, which could be either due to increased blade interactions with wake turbulence or to the contribution of other noise sources in the BWI spectrum range. These levels are investigated in the following paragraphs.

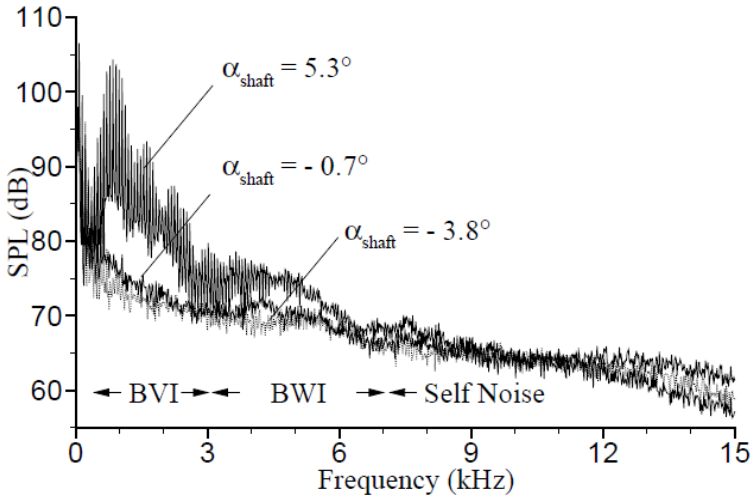

Figure 5-1: Noise spectra for three typical flight conditions (taken from [100]).

5.2 Analysis of acoustic data

The analysis of the acoustic data is performed for both measured acoustic pressure waveforms and spectra. The analysis aims to specify the magnitude of BWI noise, the contribution of BVI noise in the BWI spectrum region and the location of the rotor azimuth region responsible for BWI noise. Further, the acoustic data are examined to determine whether characteristic frequencies in the BWI range can be identified. For this study a frequency range of 0.4 kHz to 2.6k Hz (5-40bpf) is considered characteristic of BVI noise, while the BWI frequency region is set between 2.8 kHz and 6 kHz (43-93bpf). These ranges are similar to those used by Brezillion et al.

A new element in the analysis of the pressure waveforms is that BWI fluctuations for both acoustic and blade pressure data are not derived as the difference between the instantaneous and the average histories, but only instantaneous histories are used. This is due to the error that can be introduced by the ensemble averaging method [106], especially for this database, which contains steep BVI pulses. However, the analysis was repeated using the instantaneous minus average approach and results were almost identical. Consequently, it can be argued that average pressure waveforms are not needed for BWI analysis.

5.2.1 Types of BWI acoustic pressure fluctuations

In order to isolate the BWI pressure component of the acoustic pressure waveforms, a band pass filter for the BWI frequency region of the spectrum (43-93bpf) is applied to the instantaneous acoustic signals. Results are shown for Mic 3 / x=-2, which contains advancing side BVI noise and at the same time high levels of BWI noise [Figure 5-2 (a)]. Similar results are observed for the other advancing side microphones. The resulting BWI-filtered waveform can be seen in Figure 5-2 (c) for one rotor revolution (T). The signal contains both random and periodic components. Closer observation of a single blade passage [shown in Figure 5-2 (d)] reveals that the BWI signal consists of two defined regions. The first region contains the higher amplitude fluctuations, which have the same phase position as BVI pulses [compare Figure 5-2 (b)

and (d)]. These fluctuations will be named "Type I fluctuations" hereinafter. The second region contains lower amplitude fluctuations that come immediately after the strong BVI pulses and will be named "Type II fluctuations".

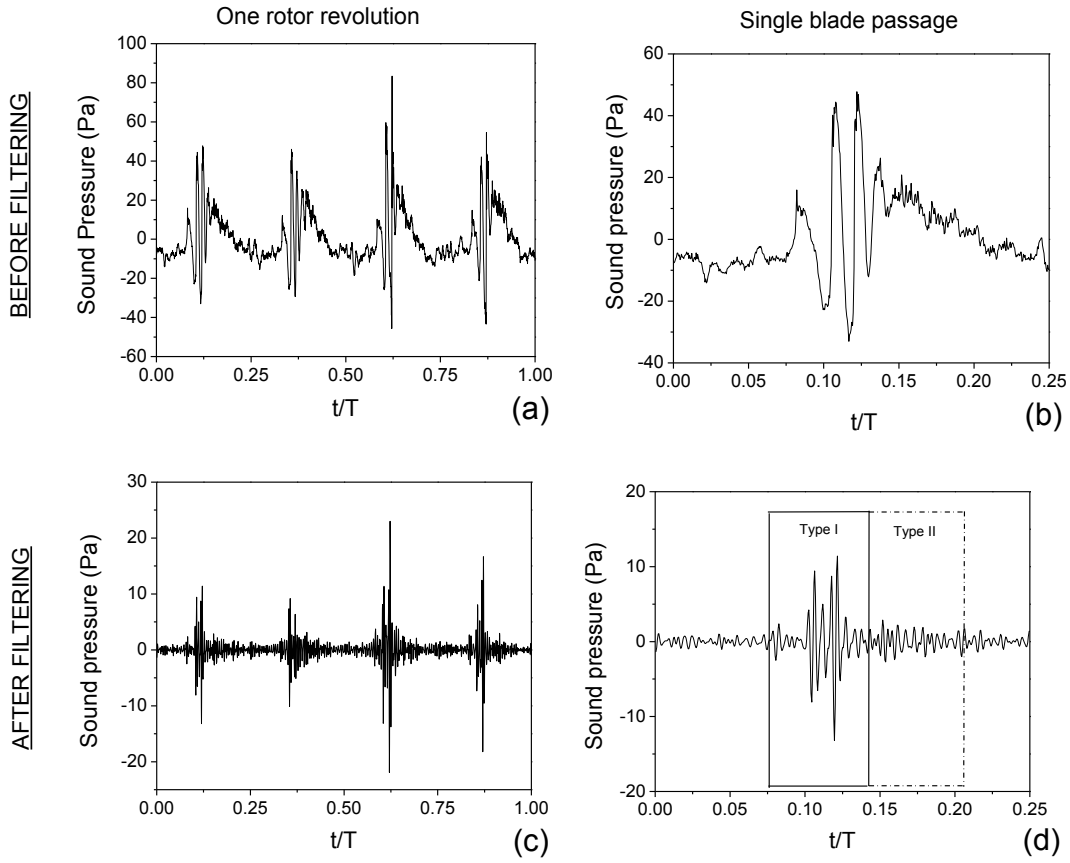

Figure 5-2: Instantaneous advancing side BVI acoustic signal before and after applying the BWI filter for one rotor revolution [(a),(c)] and for a single blade passage [(b),(d)]; fluctuations corresponding to the traditional BWI frequency region are subdivided into Type I and Type II fluctuations (d).

As it will be shown later in this paper, Type I fluctuations correspond to the higher harmonics of BVI noise and are attributed to the steepness of the BVI pulses. The existence of BWI fluctuations connected to BVI impulses has also been referenced by Bouchet and Rahier [100] as "BWI-like" fluctuations in their analysis of blade pressure waveforms and by Brooks as "jitter" [107]. Type II fluctuations represent the actual BWI noise and, as will be shown later, are randomly distributed.

As Type I fluctuations are attributed to the steepness of BVI pulses, this characteristic can affect their amplitude and, thus, their relative importance compared to Type II fluctuations. For the HELISHAPE data, Type I fluctuations are of higher amplitude than Type II. Type I fluctuations might be of smaller amplitude, when the BVI pulses are less steep. For all advancing side signals, Type I fluctuations come before Type II. On the contrary, for microphones containing strong retreating side BVI pulses, Type II fluctuations tend to come before BVI pulses (Figure 5-3). This observation agrees with suggested BWI mechanisms, as blades moving on the retreating side of the rotor experience perpendicular vortex interactions (Type II), before the impulsive parallel blade vortex interactions (Type I). Because retreating side BWI noise levels are very low, they will not be examined further in this study.

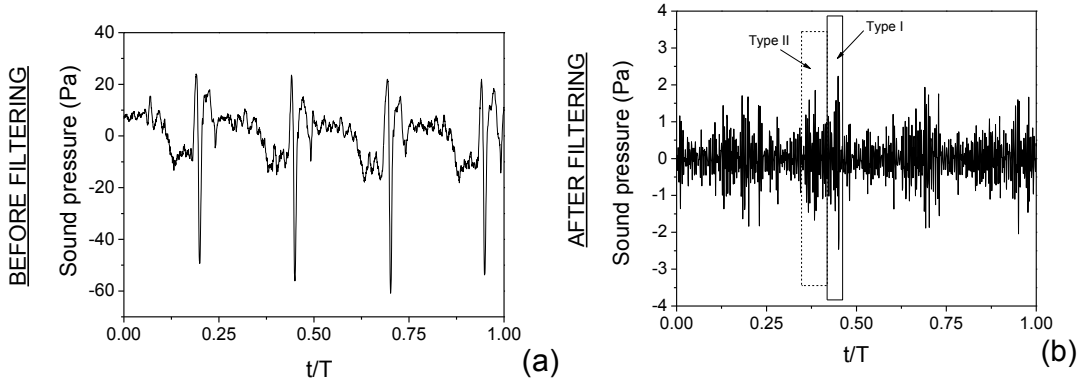

Figure 5-3: Instantaneous retreating side BVI acoustic signal before (a) and after (b) applying the BWI filter.

5.2.2 Azimuthal localization of BWI region on the rotor disk

In order to identify the azimuthal range on the rotor disk that is associated with noise in the BWI frequency region, a BVI localization scheme [108] has been appropriately applied to the BWI fluctuation waveforms. This localization scheme has been applied in the past for localization of BVI pulses and it cannot be directly applied to broadband BWI noise due to the lack of discrete pulses. A procedure is presented here on how to identify the BWI broadband waveform pattern for use with the

localization scheme. First, the BWI-filtered signal is broken into four equal parts, each part corresponding to a blade passage. Overlapping of these parts reveals the general pattern of BWI fluctuations, as seen in Figure 5-4 (a). The four different blade passage BWI fluctuations show strong consistency in terms of phase and amplitude. The average of the absolute values of these fluctuations is evaluated and compared to the average waveform of the same microphone [Figure 5-4 (b)]. It is observed that the greater values of the average BWI fluctuations coincide with the steep BVI slopes of pulses B and C revealing that these fluctuations are in fact the higher harmonics of BVI noise. Brezzilion's conclusion, that parallel BVIs, which generate impulsive noise, are also sources of BWI noise, is validated only partially for this study, as parallel BVIs are seen to be sources of Type I fluctuations, contributing to BWI frequency region solely through their higher harmonics.

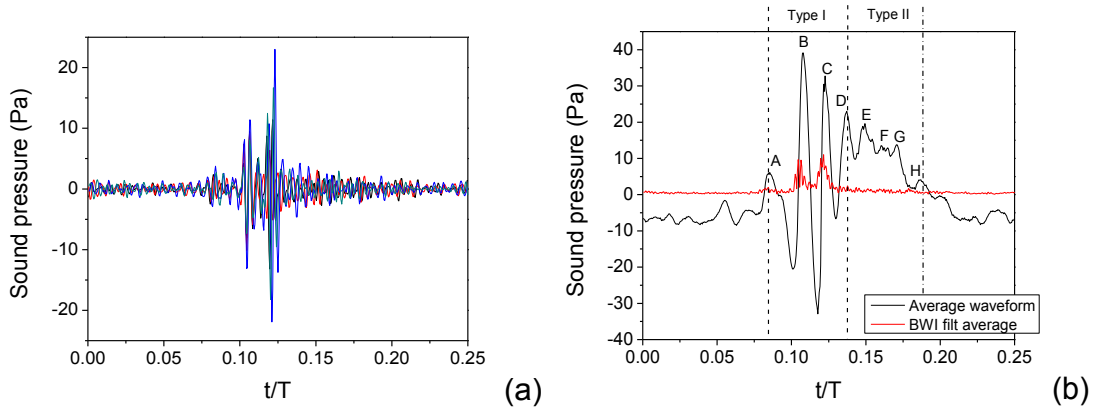

Figure 5-4: Pattern of BWI fluctuations revealed by overlapping all four BWI-filtered blade passages (a) and association of the average of the absolute values of the fluctuations of the four blade passages shown in (a) with the average acoustic pressure waveform (b).

BWI fluctuations of Type II [see Figure 5-4 (b)] can be considered to be between pulses D and H of the average waveform. BVI localization procedure is applied for pulses A, D and H. Azimuth region between pulses A and D can be considered an estimate for the dominant parallel BVI region containing strong discrete pulses and Type I fluctuations. Azimuth region between D and H can be considered as an estimate of acoustically most significant BWI region containing Type II fluctuations. The above

localization results were validated by comparing the BVI locations to HELISHAPE Laser Light Sheet (LLS) measurements and blade pressure measurements.

The azimuthal ranges associated with Type I fluctuations are found to be between 50 and 85 deg (see Figure 5-5). This is the typical region of parallel BVIs in descent flight conditions, which can also be derived from blade pressure measurements. The range for Type II fluctuations is set between 85 and 115 deg, which is the range that blade wake turbulence interaction mostly occurs. This azimuthal range will be called "BWI window" hereinafter. Acoustic measurements of Marcolini and Brooks [109] in descent flight conditions placed the highest BWI levels mainly in the first quadrant of the rotor disk and to a lesser extent in the second quadrant. In the database analyzed here the highest values are also observed in the first quadrant. However, these high values are attributed to the high amplitude Type I fluctuations, which are related to BVI noise.

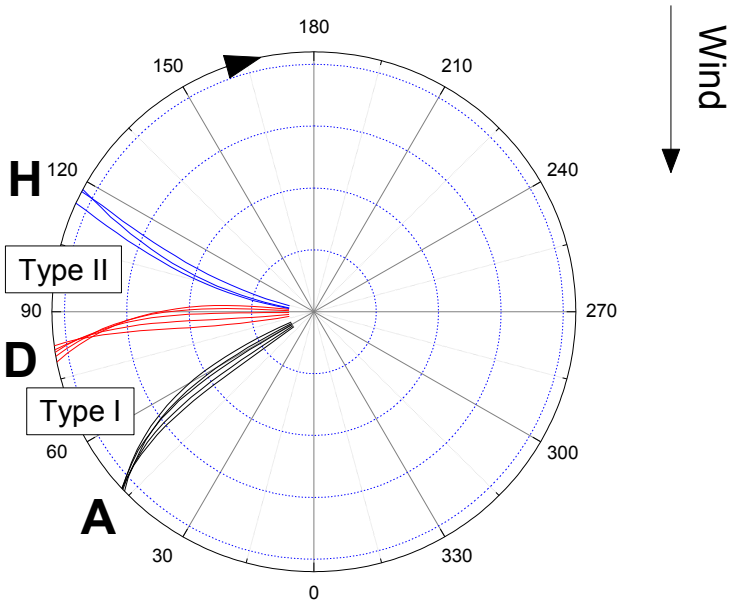

Figure 5-5: Azimuthal ranges on the rotor disk associated with Type I and Type II fluctuations.

5.2.3 Statistical and spectral properties of BWI acoustic pressure fluctuations

The difference in the physical origin of the two types of BWI fluctuations can also be seen by examining the statistical properties of the two regions. The windows used for the statistical analysis of the two types of BWI fluctuations are based on their azimuth range derived in the previous paragraph. The statistical distribution of the fluctuations seen in the Type I region (50 to 85 deg window) deviates significantly from Gaussian distribution [Figure 5-6 (a)]. On the other hand, Type II region fluctuations (85 to 115 deg azimuth, or "BWI window") exhibit an almost Gaussian distribution [Figure 5-6 (b)] revealing their random nature. The results shown in Figure 5-6 for Mic 3 / x=-2 are representative for other microphones containing high BWI levels.

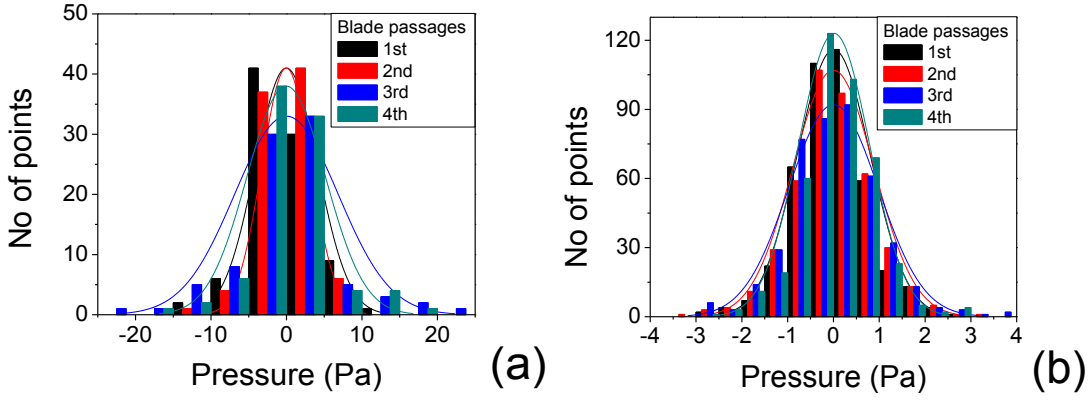

Figure 5-6: Statistical distribution of Type I (a) and Type II (b) fluctuations for Mic 3 / x=-2.

In order to examine the spectral properties of the "BWI window" on the acoustic pressure waveforms, a slightly different filtering approach is followed. As the BWI window can contain contributions of other noise sources except BWI noise, the instantaneous acoustic pressure waveforms, instead of being band-pass filtered to BWI range, are being high-pass filtered to 5bpf. This was done in order to allow spectral analysis to investigate the behaviour of the complete frequency range of the designated "BWI window". A 10% cosine-Tukey window is applied to the "BWI window" and an FFT analysis is performed to the resulting signal. Since the range examined is constant

for all cases (85 – 115deg azimuth window) the resulting resolution bandwidth is approximately 275 Hz. This process was repeated for the "BWI window" of each blade passage and the spectrum for a single microphone acoustic signal was computed by averaging the four "BWI window" spectra.

Figure 5-7 shows the average spectrum levels of the "BWI window" over a large number of microphones in the advancing side of the rotor. It can be observed that the spectrum of the "BWI window" exhibits significant levels in the BVI frequency range signifying the presence of medium frequency loading noise, while no significant distinct frequency or hump can be seen in the BWI frequency range. Specifically, there is no significant evidence of the distinct peak in the region of 2.5 kHz, which has been observed in the acoustic spectra of take-off flight conditions in similar experiments [91].

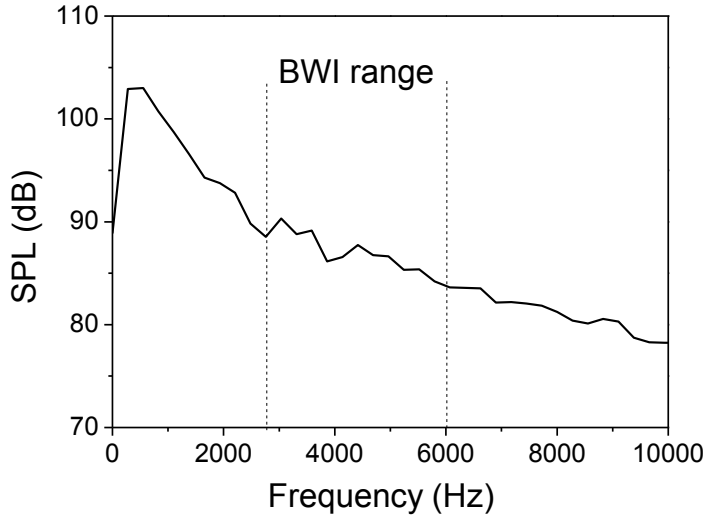

Figure 5-7: Average spectral levels of "BWI acoustic window" over microphones in the advancing side.

5.2.4 Contribution of BVI noise in the BWI spectrum region

The contribution of BVI noise in the BWI spectrum region analyzed in the previous sections in terms of acoustic pressure fluctuations can also be observed in the acoustic spectra.

For the determination of BWI spectrum levels and the formation of the frequency contours below the rotor, the BWI levels of the average spectra are commonly used. This approach can be seen in the contour of Figure 5-8 (a) for the database examined. However, in the case of descent flight conditions, the contribution of BVI noise in BWI frequency region of the average spectra can be significant.

Acoustic data from the HELISHAPE test include both average and coherent power spectra. Ideally, the BWI region levels of the average spectra contain contributions of both BVI and BWI noise (Type I and Type II fluctuations), while the BWI region of the coherent spectra contains only BVI noise (Type I fluctuations) [Figure 5-8 (b)]. Thus, the logarithmic subtraction of the coherent from the average spectra would give an accurate estimate of the BWI noise levels. Unfortunately, this is not the case. The error introduced in the BWI frequency region levels of the coherent spectra, due to the ensemble average method in the calculation of the average waveform, can be significant [106], which means that this process can underpredict the BVI noise contribution.

The strong contribution of BVI noise in BWI region in the database examined can be seen by taking a closer look in the acoustic spectrum. It can be observed that the frequency content of the BWI region [Figure 5-8 (c)], almost in its entire range, is arranged in equally spaced peaks, which also form some greater humps. These characteristics, which are seen over a large number of microphones in the advancing side region, reveal that the effect of BVI impulsive noise in the BWI frequency region is dominant [110]. Moreover, in chapter 3 of this thesis, it has been shown that nonlinear effects, which steepen BVI pulses with propagation distance, can transfer their energy to higher frequencies beyond the traditional BVI range and into BWI range. These findings suggest that BWI contours based on average spectra for descent flight conditions can be misleading.

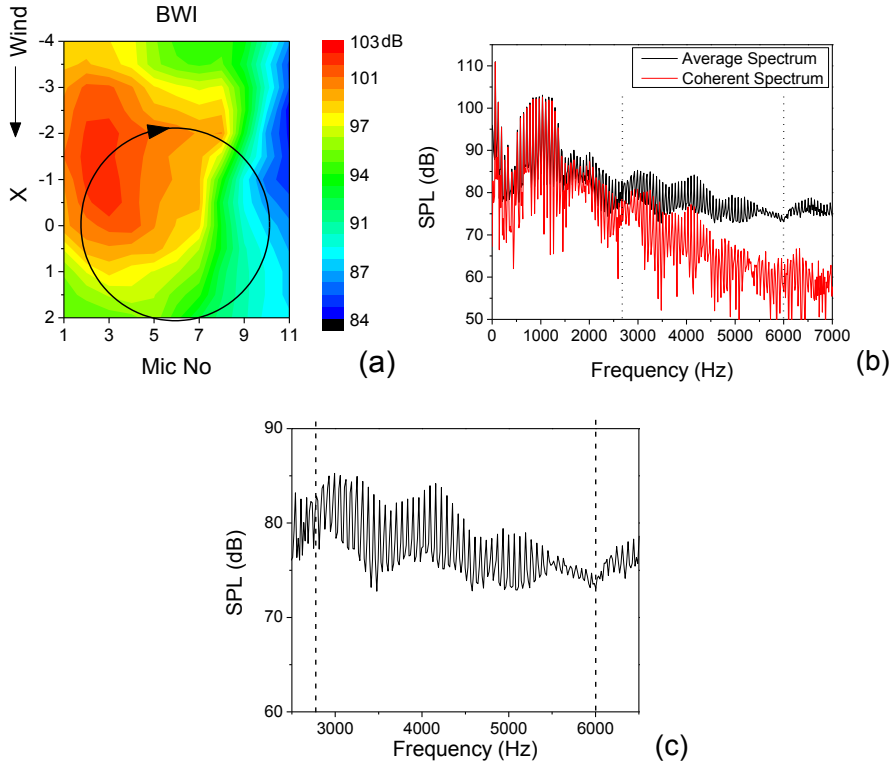

Figure 5-8: BWI noise contour based on average spectra (a); average and coherent spectrum (b) and BWI frequency region of the average spectrum (c) for (Mic 3/x=-2).

The dominant effect of BVI noise in the BWI region, which results in the spectrum retaining the BVI spectrum characteristics, coupled with the acoustically non-significant levels of the BWI frequency region compared to BVI region, could suggest that BWI modelling can be ignored in descent flight conditions and noise generation calculations can be limited to BVI noise with acceptable accuracy.

5.3 Analysis of aerodynamic data

A similar analysis to that of acoustic pressure data is performed for the blade pressure signals. The instantaneous differential pressure waveforms are used to locate the exact BWI region on the rotor disk. Moreover, the pressure and suction side pressure measurements are used for chordwise and spanwise coherence analysis in order

to extract any properties of the wake turbulence interacting with the blades and detect any dipoles that could contribute to BWI noise.

5.3.1 Definition of BWI region on rotor disk and of interacting vortices

In order to locate in span and azimuth the pressure fluctuations regarded as potential BWI noise sources, BWI frequency band-pass filters are applied to the differential pressures (ΔC_p) of the leading edge sensors at 2% chord. The plots of BWI and BVI fluctuations on the rotor disk are shown in Figure 5-9. The region shown ranges from 0.6R to the outboard region, which is known to be the acoustically significant part of the rotor disk. It should be noted that as the angle of attack is changed during the blade's revolution, the pressure distribution changes in the upper and lower blade surfaces and the pressure differential between two fixed points at a fixed chordwise location is not necessarily consistent with the net unsteady lift. However, in the following study, the differential pressures are used to locate the dominant BWI regions around the rotor and not to provide comparisons between them. For each of the BWI regions identified hereinafter the blade angle of attack can be considered steady.

Figure 5-9 (a) shows that BWI differential pressure fluctuations can be found at many regions around the rotor disk. Significant congestion of fluctuations can be seen roughly on three sections of the rotor disk: (i) on the advancing side, (ii) on the downwind retreating side and (iii) at the further downwind end of the rotor disk. Not all of these fluctuations are responsible for BWI noise. Again, Type I and Type II fluctuations will be distinguished with respect to their origin being impulsive blade-vortex interaction or blade-turbulence interaction. In order to distinguish between the different types of fluctuations shown in Figure 5-9 (a), they will be compared against fluctuations resulting from the BWI filtering of averaged blade pressure waveforms, which are therefore exclusively Type I fluctuations attributed to the higher harmonics of BVI pulses [shown in Figure 5-9 (c)].

The region of fluctuations at the further end of downwind side (around azimuth of 0 degrees) is attributed to (i) measurement discontinuities due to one-rotor revolution

recordings and (ii) to interaction of the blades with the upper fuselage wake due to its angle to the free flow, which has been referred as “hub-wake” interaction by Brooks and Burley [98]. The retreating side region shows significant content of BWI fluctuations. However, the acoustic fluctuations in the retreating side region are very small compared to those in the advancing side, as it has been seen in the acoustic analysis section. In the downwind retreating side, the high content of BWI fluctuations, which coincides with blade vortex interaction locations around the azimuth of 300 degrees are Type I retreating side fluctuations and are partially seen in Figure 5-9 (c).

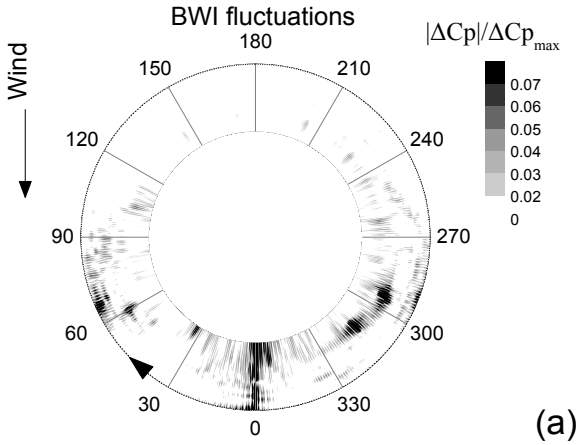

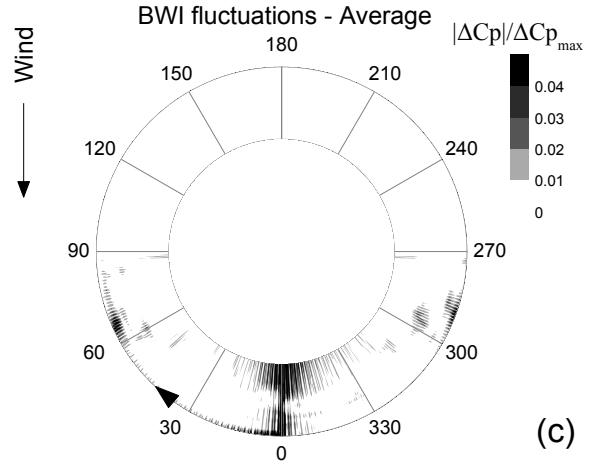

Figure 5-9: BWI differential blade pressure fluctuations on rotor disk from instantaneous signals (a), BVI differential blade pressure fluctuations from instantaneous signals (b) and BWI differential blade pressure fluctuations from average signals (c).

The acoustically most important BWI fluctuations are the ones found on the advancing side of the rotor. The fluctuations seen in Figure 5-9 (a) on the advancing side region (from about 50 to 85 degrees) coincide with parallel BVIs seen in Figure 5-9 (b) and are therefore Type I BWI fluctuations. Smaller fluctuations seen in the region of 85 to 115 deg can be characterized as Type II fluctuations as are they are only present in the instantaneous plot [compare Figure 5-9 (a) and (c)]. These fluctuations seem to be small in amplitude but they are exactly in the region, which has been found from the acoustic analysis to be the most significant for BWI noise. Combination of the acoustic and aerodynamic localization results sets the Type II fluctuations region (and, thus, the acoustically most important BWI region) to be between 0.85R at 85 deg and 0.62R at 115 deg azimuth. The 0.7R pressure transducer was selected as being in the most active BWI region of the rotor disk and it will be used for statistical and spectral analysis shown in the following paragraph.

In order to determine the exact vortices found in that region, rotor wake geometry charts [111] are used. Figure 5-10 shows the blade vortex interaction locations for a flight condition case very close to that examined in this study. The vortices, which correspond to the derived BWI region, are shown to be enclosed in the red dashed line.

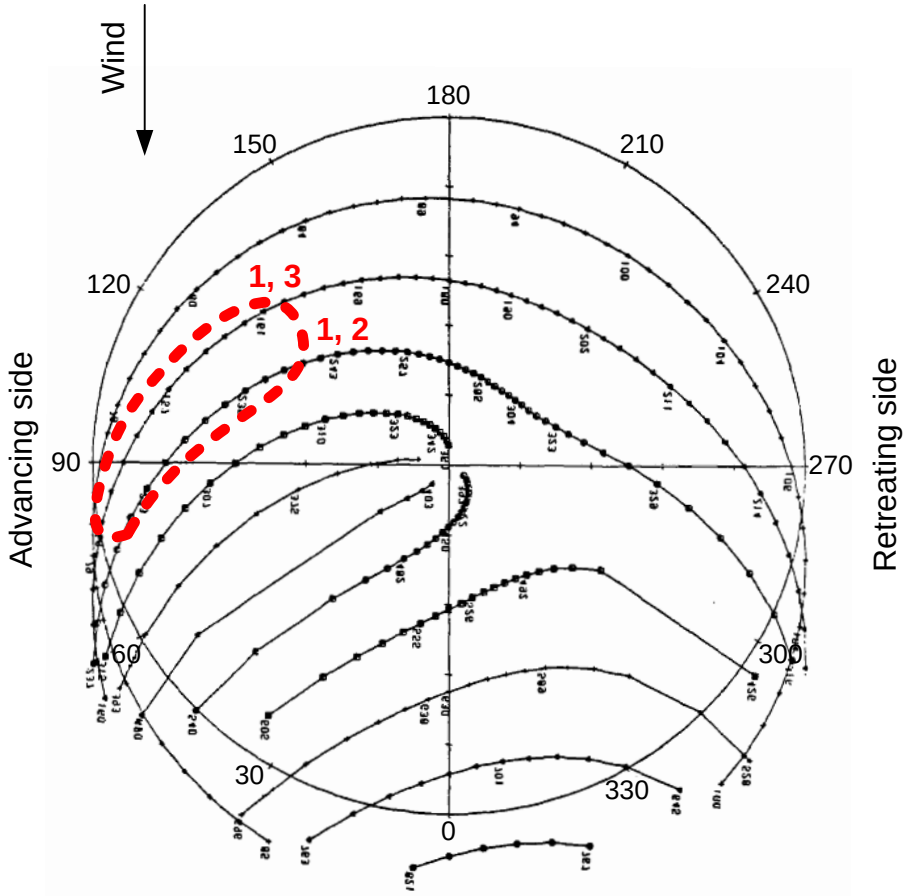

Figure 5-10: Plot of potential BVI locations and vortices encountered in the acoustically dominant BWI region ("BWI window").

In terms of interaction angle, the interactions shown in the circled BWI region are oblique, almost perpendicular. This agrees with existing knowledge for this type of noise source. A closer look into Figure 5-10 shows that BWI noise is mostly attributed to the interaction of blade 1 with two vortices that come from the preceding blades: blade 3 vortex having an age of 150-160deg and blade 2 vortex having an age of 230 to 235 deg.

These interaction locations are shown in Figure 5-10 as "1,3" and "1,2" respectively. Both vortices have already encountered one or more interactions, while blade 4 vortex, which is generated from exactly the previous blade, has an age of less than 80 deg, has not experienced an interaction with a blade and does not contribute to BWI pressure fluctuations.

5.3.2 Statistical and spectral properties of BWI blade pressure fluctuations

The statistical and spectral analysis of blade pressure waveforms is not done for differential pressures, but for single side pressure measurements similar to Bouchet and Rahier study.

The measured instantaneous blade pressure waveform at 0.7R for the lower side (pressure side) can be seen in Figure 5-11 (a) and the filtered BVI and BWI components of the advancing side in Figure 5-11 (b). In Figure 5-11 (b) the BWI fluctuations are seen in the region between 85 and 115 deg coinciding with the region of two BVI pulses (1,2 and 1,3). This region is shown in the dotted box, which indicates the bounds of the respective "BWI window" to be used for the spectral and statistical analysis.

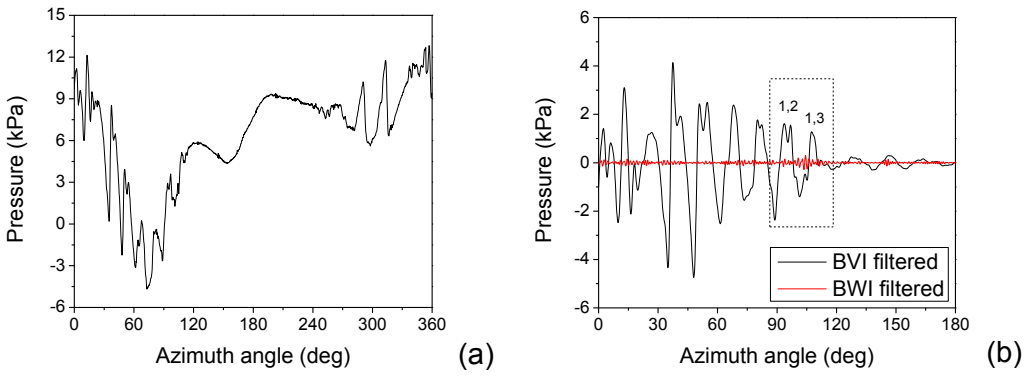

Figure 5-11: Blade pressure waveform at 2% chord, 0.7R, pressure side (a) and corresponding BVI/BWI filtered signals on the advancing side (b).

Regarding probability distribution, Type I blade pressure fluctuations do not exhibit a Gaussian distribution, similar to Type I acoustic fluctuations. On the other hand, Type II blade pressure fluctuations' distribution [Figure 5-12 (a)] is seen to have only minor deviations from gaussianity.

For the spectral analysis, in order to get results beyond the BWI region, the blade pressure signals were high-pass filtered at 38bpf (2500 Hz). Coherence is defined as:

$$\gamma = \frac{\left|S_{x,y}\right|^2}{\left|S_{x,x}\right|\left|S_{y,y}\right|} \tag{5.1}$$

where $\left|S_{x,x}\right|$ and $\left|S_{y,y}\right|$ are the autospectra of the blade pressure signals recorded at x and y respectively, and $\left|S_{x,y}\right|$ is the cross-spectra between the two positions. Coupled with the phase of the cross-spectra, coherence can provide some interesting results on the properties of the turbulence encountered by the blade. In the following analysis coherence is plotted versus non-dimensional frequencies, namely Struhal number (S_t):

$$S_t = fc / U \tag{5.2}$$

where f denotes the frequency, c the blade chord and U the chordwise convection speed with respect to the blade section.

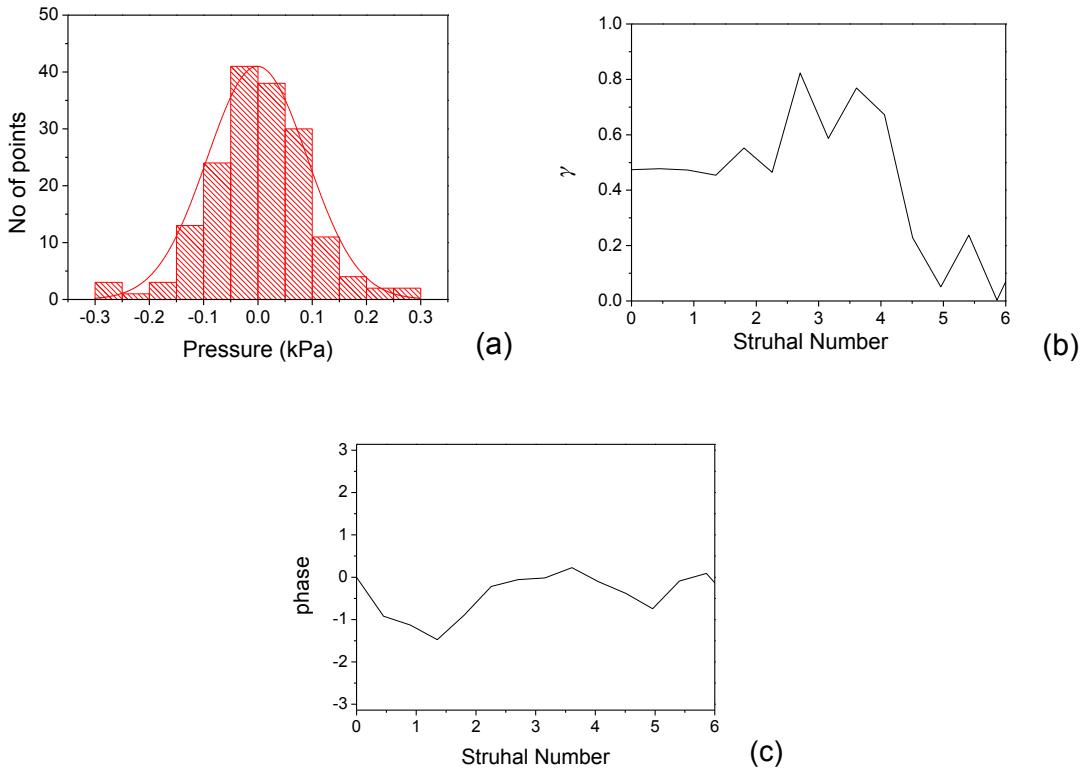

Figure 5-12: Statistical Distribution of Type II blade pressure fluctuations (a). Chordwise coherence vs. Struhal Number (b) and cross-spectra phase (c) at 2%-6% chord, 0.7R, pressure side.

Chordwise coherence between 0.02c and 0.06c, was examined for the "BWI window" for both the pressure and suction side. While the suction side gave non-significant results, the pressure side coherence and phase for the "BWI window" (0.7R, 85 to 115 deg) can be seen in Figure 5-12 (b) and (c). It can be observed that significant coherence values can be seen in the region of 3-4 Struhal number coupled with a cross-spectra phase around zero. The spanwise coherence study also did not provide significant coherence values.

The coherence between the BWI fluctuations of the pressure and suction side is interesting to be examined for acoustic purposes. In the study of Bouchet and Rahier [100] made for take-off flight conditions there was proof of acoustic dipoles in the region of 2.5 Struhal number. The same coherence analysis in the descent flight conditions of the HELISHAPE database did not provide any out of phase high coherence value which could be considered proof of acoustic dipoles (Figure 5-13).

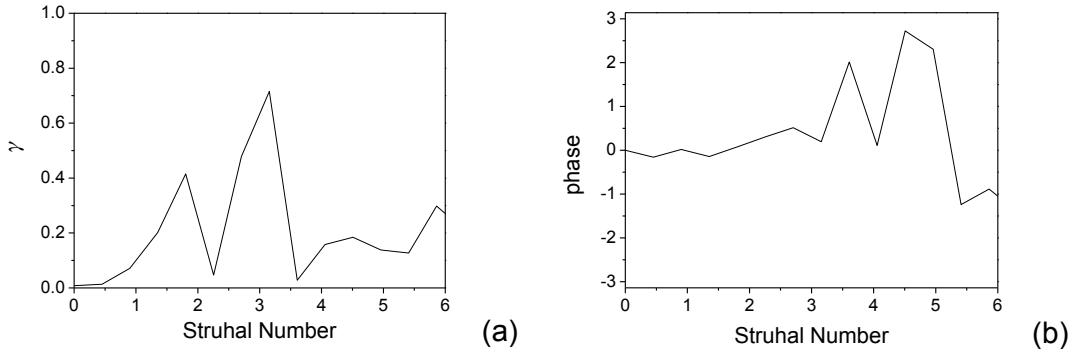

Figure 5-13: Suction-pressure side coherence (a) and cross-spectra phase (b) at 2% chord, 0.7R.

The existence of a chordwise coherence in the range of 3-4 Struhal number, as well as the lack of acoustic dipoles, reinforces Glegg et al. [94] BWI noise modelling, which uses a turbulent velocity spectrum with a distinct peak at $fc/U = 3.4$ and Amiet's theory. Also the connection of Type II pressure fluctuations with vortices having already encountered a blade passage provides additional evidence to that direction.

5.4 Laser light sheet analysis

For completeness of the analysis report on the HELISHAPE descent database, the following observation based on the LLS flow visualization data, is noted.

A component of the turbulence structure present in the rotor flow can be seen in the LLS flow visualization images. The portion of the flow highlighted by the laser sheet in Figure 5-14 (a) connects the turbulent regions of the two corotating vortices as a result of their interaction. It should be noted that the train of vortices produced by the subsequent blade passages are unequal due to their core evolution with age.

The shape of this flow resembles the S-shape of the straining out phenomenon found in the interaction of unequal corotating vortices [112,113] [Figure 5-14 (b)], where filamentary vorticity breaks away from the smaller vortex and is wrapped around the larger vortex. Calculations on the experiment's vortices' core radius [114] found in the BWI rotor disk region, gave ratios in the order of 0.8, which support the effect of straining out. The contribution of those filaments to BWI noise could be significant as they form a sheet of eddies in the region between two sequential vortices and contribute to the rearrangement of turbulence around the vortices' cores.

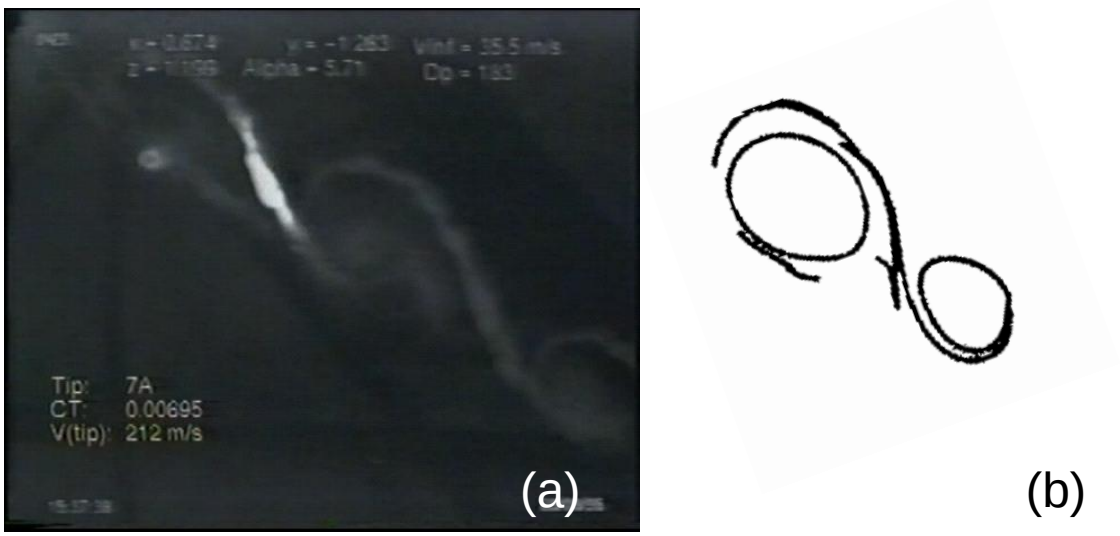

Figure 5-14: LLS flow visualization image (a) and shape of "straining out" encountered in a pair of co-rotating vortices [112] (b).

5.5 Effect of blade tip shape

A similar analysis to the one applied to blade 7A with the rectangular tip has been applied to blade 7AD that has a swept-back parabolic anhedral tip. The two cases show both similarities and differences.

The probability distribution and spectral analysis showed that Type I and II fluctuations are characterized by the same properties for both blade tip cases. The location of the BWI region and of the vortices encountered is the same for both blade tips, showing that, as far as descent case is considered, blade tip has no significant effect on the turbulence encountered by the blade.

The most important difference between the two cases was seen in the acoustic spectrum data. The BWI frequency region of the average spectra seems to be significantly higher for the rectangular blade tip case [Figure 5-15 (a)]. Comparison of the BWI band-pass-filtered acoustic pressure fluctuations of the two blades [Figure 5-15 (b)] shows that this difference is largely attributed to Type I fluctuations, which are of higher amplitude in the rectangular case. This is due to the steeper BVI pulses compared to the swept blade tip case, which amplify the higher frequencies (scalloping) of the acoustic spectrum [73]. Type II fluctuations seem to be similar for the two blades suggesting that there is no difference in acoustic fluctuations originating from blade turbulence interaction. This is clearly shown in the "BWI window" averaged spectrum of both blade tips in Figure 5-15 (c).

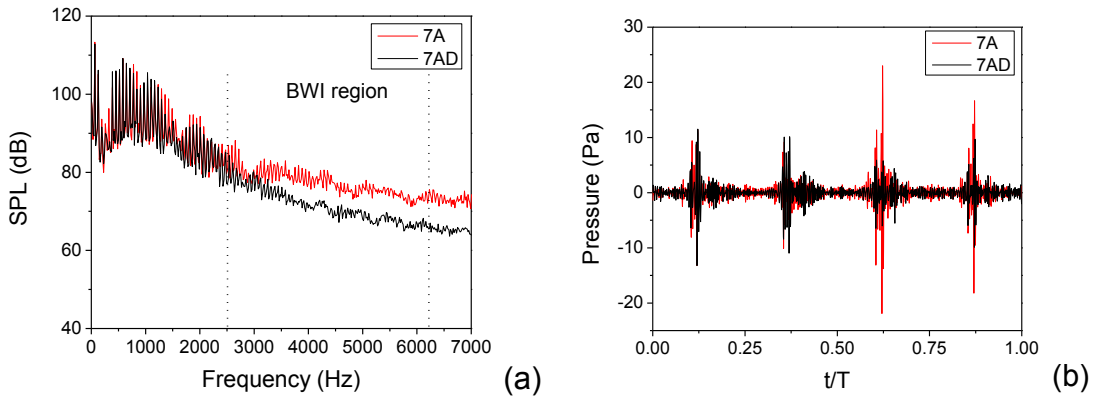

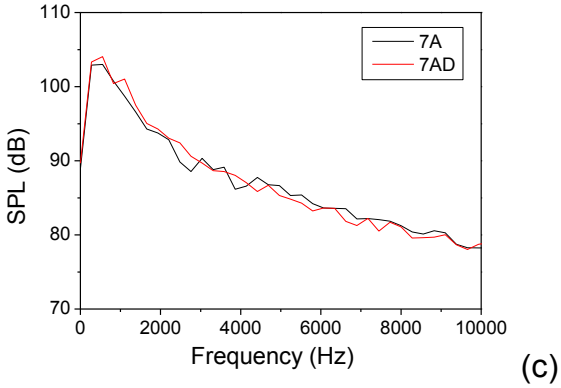

Figure 5-15: Average spectra (a) and acoustic fluctuations after BWI filtering (b) for the two different blade tips (Mic 3/x=-2) and average spectrum levels of the BWI window (c).

6 Conclusions

The present thesis examined (i) the nonlinear propagation of air vehicle noise in the far field region using the Burgers Equation and (ii) the interaction of sound with flow and solid boundaries in the near field region using a newly developed low order method. A by-product of the HELISHAPE experimental database analysis resulted in some interesting observations on the BWI noise mechanism. Conclusions of this work can be subdivided in the three following paragraphs.

6.1 Burgers equation application for farfield nonlinear propagation

In the present work, the effect of nonlinear propagation distortion on helicopter main rotor noise was presented. The case of low-speed descent was examined, where Blade Vortex Interaction (BVI) noise is the dominant noise contributor. The study was based on measured data close to the rotor, obtained from the HELISHAPE experiment, and numerical calculations employing the augmented Burgers equation predicting the noise level at the far field with and without nonlinear effects.

It was shown that nonlinear effects in BVI noise propagation, which have been ignored in the past, can be important in certain cases. Specifically, it was shown that:

- Advancing side BVI noise is affected by nonlinear distortion, while retreating side BVI noise is not.
- Octave frequency bands of 1000 and 2000 Hz are mostly affected.
- The difference between linear and nonlinear calculations can be as high as 7 dB for the affected frequency bands.
- Receiver locations from 180 to 220 deg azimuth angle and from -40 to -70 deg elevation angle seem to be mostly affected.

Based on the signal characteristics at source, two quantities which can characterize the nonlinear propagation of the BVI signal were derived.

- Polarity: this quantity is based on the pressure gradient of the source signal and can be used to determine whether a BVI signal will evolve as an advancing or a retreating side signal.
- Weighted rise time: this quantity is a measure of the impulsiveness of the BVI signal at source and can be used to determine at which frequency nonlinear effects start to appear.

Other results of the rotor noise nonlinear propagation investigation include:

- A second blade tip shape, which was used in the experiment, was shown to be similarly affected by nonlinear distortion as its acoustic pressure waveforms did not change drastically compared to the initial blade tip.
- Instantaneous signals are less affected by nonlinear distortion (smaller DSPL values) than averaged signals, due to their higher frequency broadband content.
- High speed impulsive noise experienced great DSPL values when shocks where present in the signal.
- Polarity and weighted rise time were also shown to be applicable in the non-BVI cases considered.

Finally the present work provided an estimate of the magnitude of the nonlinear effects, as well as, of the frequency bands it affects. Specifically, three new methods are presented:

- A numerically generated database that provides a rough guideline for DSPL values and corresponding frequency bands, when only the receiver location is known. No numerical estimations have to be made for this method, making it a very fast method, which, however, has to be applied only for similar rotor cases.

- Correlation equations between DSPL and various signal characteristics at the source have been derived. They are very simple to be applied and can be used to determine whether a detailed prediction is needed.
- Predictions on nonlinear propagation distortion cannot often be performed because only the noise spectrum is given, not the pressure signal itself. The phase-assignment method is derived that reconstructs a pressure time signal from the available noise spectrum assigning specific phases to frequency regions. Burgers equation is then applied to the reconstructed signal giving an estimate of the expected nonlinear effects.

6.2 New method for the prediction of near-field propagation effects

The prediction of the propagation in the near field of an aircraft is a complex problem as many phenomena are involved. In order to include the flow field effect on sound propagation, as well as the interference of the emitted sound with solid boundaries, a new low-order method, using adaptive hybrid grids in 3D, was presented. A special splitting of the total inviscid flow field allowed the formulation of a simple flow/acoustics interaction method to treat sound propagation through complex inviscid flow fields.

The key assumptions of this splitting were that sound propagation does not affect the flow-field and that flow generated sound is insignificant compared to the acoustic sources present in the flow field.

The new method's characteristics are the following:

- Minimal computational cost.

  A typical, low-order finite volume spatial discretization was employed for minimal computational cost. Low order boundary conditions appropriate for hybrid grids were applied for the acoustic farfield, and the interaction of sound with solid surfaces.

- Applicable for propagation in adaptive hybrid grids.
  Hybrid grid convergence study showed the method capable of predicting monopole sound propagation. Local, SPL-based grid adaptation was applied and proved effective in improving the accuracy of the present low-order method for sound propagation.

- Successful prediction of the interaction of sound with solid boundaries.
  The reflection of a monopole sound on a wall and the diffraction of a sound pulse by a rigid barrier were examined. Results compared well with analytic solutions proving that sound diffraction can be predicted using this low order scheme. Monopole sound diffraction by a sphere in a steady mean flow showed a significant effect of the flow field on the diffracted sound. Relatively poor quality hybrid grids were purposely used in this work in order to test the method.

Except from the method validation results, other applications demonstrated the following findings:

- The superiority of dynamic over static coupling was demonstrated.
  The flow/acoustics interaction method applied in this study, allowed the low order method to work with hybrid grids and unsteady flow fields. The case of monopole source propagation through a strongly unsteady flow field past a rectangular obstacle was examined using static and dynamic flow/acoustics coupling. The importance of dynamic coupling was shown over static flow coupling.

- Proof of concept was provided by application for an airplane.
  The method was applied to a realistic geometry of a conventional airplane, where engines were modeled as monopoles under the wing (UWN configuration). The effect of the flow field on the SPL levels was clearly shown on the fuselage and on the acoustic signature below the fuselage. The effect of wing shielding was also shown by comparing the

UWN case to over the wing nacelle (OWN) case. It was shown that placing the engine above the wing provided lower SPL levels below the aircraft fuselage.

A subject of subsequent work is the inclusion of the viscous terms in the governing equations of both fields, as well as the use of different meshes for each field.

6.3 BWI noise characteristics in descent flight conditions

The analysis that was performed on the HELISHAPE descent flight condition's database provided characteristics of BWI noise, as well as evidence of the generating mechanism. The database analysis' results were the following:

Results based on the analysis of the acoustic pressure database:

- BWI fluctuations can be categorized as Type I or Type II, according to their association to BVI or BWI noise, respectively. Type II fluctuations, showing a Gaussian probability distribution, provided the "BWI window" corresponding to azimuth range of 85 to 115 deg on the rotor disk.
- A spectral analysis of this window throughout a large number of advancing side microphones did not provide any distinct peaks in the BWI frequency range, as the case seen in take off conditions of other experiments.
- The shape of the average spectra of the entire acoustic signals showed that the contribution of BVI noise in BWI frequency region is significant, which renders the use of average spectra for BWI noise contours questionable.

Results based on the analysis of the blade pressure database:

- Blade pressure fluctuations can be also categorized as Type I or Type II having similar probability distribution characteristics to their acoustic counterparts.
- The dominant BWI region on the rotor disk was set by localization of the acoustic signals and BWI blade-pressure fluctuations. Comparison of the

resulting BWI region with rotor wake charts showed that BWI noise is associated to vortices which have already encountered a blade passage.

- Chordwise coherence between 0.02c and 0.06c at pressure side provided significant coherence in the range of 3 to 4 Struhal number. Spanwise coherence failed to provide significant coherence values, while the coherence between pressure and suction sides did not show the existence of acoustic dipoles in the BWI range.

Results based on the analysis of the LLS data:

- LLS images show significant turbulent regions around tip vortex cores, which seem to interact in an S-shape. This interaction, which resembles the vortex straining out phenomenon, can affect the redistribution of turbulence around and in the region between vortex cores. This phenomenon could be of importance for BWI noise prediction models.

Regarding the effect of blade-tip on BWI noise:

- Analysis of a second database corresponding to a swept back blade-tip, did not show to affect the levels of BWI noise, while the levels of the BWI frequency region of average spectra were considerably lower due to less steep BVI pulses.

In conclusion, regarding BWI noise in descent flight conditions, the existence of BWI fluctuations around vortices which have already encountered a blade passage, the strong chordwise coherence of the blade pressure fluctuations in the region of 3 to 4 Struhal number, as well as the lack of acoustic dipoles in the BWI frequency range, can support the modelling proposed by Glegg et al. or Brooks and Burley based on Amiet's theory. Nevertheless, the acoustic analysis of the present database suggests that BWI noise can be ignored in descent flight conditions, as BVI noise dominates the BWI frequency region of the acoustic spectra.

REFERENCES

1. Brentner, K. S. and Farassat, F., "Helicopter noise prediction: The current status and future direction," J. Sound Vib. 170, 79-96 (1994).
2. Brentner, K. S. and Farassat, F., "Modeling aerodynamically generated sound of helicopter rotors," Progress in Aerospace Sciences 39, 83-120 (2003).
3. Schmitz, F. H., Rotor noise, in Aeroacoustics of Flight Vehicles: Theory and Practice, Vol. 1: Noise Sources, edited by H.H. Hubbard (Acoustical Society of America, American Institute of Physics, New York, 1994).
4. Tangler, J. L., "Schlieren and Noise Studies of Rotors in Forward Flight", American Helicopter Society 33rd Annual Forum Proccedings, Washington, DC, May 1977.
5. Splettstoesser, W. R., Kube, R., Wagner, W., Seelhorst, U., Boutier, A., Micheli, F., Mercker, E., and Pengel, K., "Key results from a higher harmonic control aeroacoustic rotor test (HART)," J. American Helicopter Soc. 42, 58-78 (1997).
6. Brooks, T. F., Marcolini, M. A., and Pope, D. S., Main Rotor Broadband Noise Study in the DNW, Journal of the AHS, Vol. 34(2), 1989, pp. 3-12.
7. Lowson, M. V., "Progress towards quieter civil helicopters", Aeronautical Journal (ISSN 0001-9240), vol. 96, no. 956, June-July 1992, p. 209-223.
8. Aeroacoustics of Flight Vehicles: Theory and Practice, Vol. 1: Noise Sources, edited by H.H. Hubbard, Acoustical Society of America, American Institute of Physics, New York, 1994.
9. Webpage: http://adg.stanford.edu/aa241/AircraftDesign.html (accessed on 21st December 2011).
10. Lighthill M. J., "On sound generated aerodynamically, I: General Theory", Proc. R. Soc. London Ser: A, vol. 211, pp. 564-587, 1952.
11. Lighthill M. J., "On sound generated aerodynamically, II: Turbulence as a source of sound", Proc. R. Soc. London Ser: A, vol. 222, pp. 1-32, 1954.
12. Hosder, S., Schetz, J.A., Grossman, B., and Mason, W.H. "Airframe Noise Modeling Appropriate for Multidisciplinary Design and Optimization", AIAA

Paper 2004-0698, AIAA Aerospace Sciences Meeting and Exhibit, Reno, NV, January, 2004.

13. Aeroacoustics of Flight Vehicles: Theory and Practice, Vol. 2: Noise Control, edited by H.H. Hubbard, Acoustical Society of America, American Institute of Physics, New York, 1994.
14. Daigle, G. A., Effects of atmospheric turbulence on the interference of sound waves above a finite impedance boundary, JASA 65(1), Jan. 1979, pp 45-49.
15. Lamancusa, J. S., "Outdoor sound propagation", Noise Control course notes, Penn State, 2009.
16. Embleton, T. F. W., and Daigle, G. A., "Atmospheric Propagation," Aeroacoustics of Flight Vehicles: Theory and Practice, Vol. 2: Noise Control, edited by H.H. Hubbard, Acoustical Society of America, American Institute of Physics, New York, 1994.
17. Hamilton, M. F., and Blacktock, D. T., Nonlinear Acoustics, Academic press, San Diego 1998.
18. Menounou, P. and Blackstock, D. T., "A new method to predict the evolution of the power spectral density for a finite-amplitude sound wave", J. Acoust. Soc. Am. 115 (2), pp. 567-580, 2004.
19. Pierce, D., Acoustics: An introduction to its Physical Principles and Applications, (Acoustical Society of America, American Institute of Physics, New York, 1994).
20. Tam, C. K. W., "Computational aeroacoustics: An overview of computational challenges and applications", Int. J. of Comp. Fluid Dyn. , 18(6), pp. 547-567, 2004.
21. Curle, N., "The influence of solid boundaries upon aerodynamic sound", Proc. R. Soc. London, Ser: A 231, pp. 505–514, 1955.
22. Ffowcs Williams, J. E. and Hawkings, D. L., "Sound generation by turbulence and surfaces in arbitrary motion", Philos. Trans. R. Soc. London, Ser. A: 264, pp. 321–342, 1969.
23. Lyrintzis, A. S., "Review of the use of Kirchhoff's method in computational aero-acoustics", J. Fluids Eng. 116, pp. 665–676, 1994.

24. Wells, V. L. and Renaut, R. A., “Computing aerodynamically generated noise”, Annu. Rev. Fluid. Mech. 29, pp. 161–199, 1997.
25. Tam, C. K. W., Webb, J.C. and Dong, Z., “A study of the short wave components in computational acoustics”, J. Comp. Acoust. 1, pp. 1–30, 1993.
26. Zingg, D. W., “Comparison of high-accuracy finite-difference methods for linear wave propagation”, SIAM J. Sci. Comput. 22(2), pp. 476–502, 2000.
27. Sparrow, V. W., and Raspet R., “A numerical method for general finite amplitude wave propagation in two dimensions and its application to spark pulses”, J. Acoust. Soc. Am. Volume 90, Issue 5, pp. 2683-2691 (1991).
28. Lele, S. K., “Compact finite difference schemes with spectral-like resolution”, J. Comput. Phys. 103, pp. 16–42, 1992.
29. Lockard, D. P., Brentner, K. S. and Atkins, H. L., “High-accuracy algorithms for computational aeroacoustics”, AIAA J. 33(2), pp. 246–251, 1995.
30. Thomas, J. P. and Roe, P. L., “Development of non-dissipative numerical schemes for computational aeroacoustics”, AIAA Paper 93-3382, 1993.
31. Canuto, C., Hussaini, M. Y., Quarteroni, A. and Zang, T., Spectral Methods in Fluid Dynamics , Springer-Verlag, New York, 1987.
32. Kurbatskii, K. A. and Mankbadi, R. R., “Review of computational aeroacoustics algorithms”, Int. J. of Comp. Fluid Dyn. , 18(6), pp. 533-546, 2004.
33. Hardin, J. C. and Pope, D. S., “An acoustic/viscous splitting technique for computational aeroacoustics”, Theor. Comput. Fluid Dyn. 6(5–6), pp. 334–340, 1994.
34. Ekaterinaris, J. A., “New formulation of Hardin-Pope equations for aeroacoustics”, AIAA J. 37(9), 1033–1039, 1999.
35. Slimon, S. A., Soteriou, M. C., Davis, D. W., “Computational aeroacoustics simulations using the expansion about incompressible flow approach.” AIAA Journal 37(4), pp. 409-416, 1999.
36. Shen, W. Z. and Sorensen, J. N., “Aeroacoustic modeling for turbulent flows” 15th Nordic Seminar on Computational Mechanics, Aalborg Denmark, 2003.
37. Shen, W. Z., Michelsen, J. A., Sorensen, J. N., “A collocated grid finite volume method for aeroacoustic computations of low-speed flows”, J. of Comp. Phys., 196(1), pp.348-366, 2004.

38. Farshchi, M., Siamak, K. H., Mohammad, E., “Linearized and non-linear acoustic/viscous splitting techniques for low Mach number flows”, Int J. Num. Meth. in Fluids, 42(10) , pp. 1059 – 1072, 2003.
39. Morris, P. J., Long, L. N., Bangalore, A. and Wang, Q. Z., “A parallel three-dimensional computational aeroacoustics method using nonlinear disturbance equations”, J. of Comp. Phys., 133, pp. 56-74, 1997.
40. Hansen, R. P., Long, L. N. and Morris, P. J., “Unsteady, laminar flow simulations using the nonlinear disturbance equations,” AIAA Paper 2000-1981, 2000.
41. Kozubskaya, T. K., Abalakin, I. V., Bobkov V. G., “A half-stochastic model for noise in free turbulent flows”, AIAA Paper 2001-2258, 2001.
42. Bechara, W., Bailly, C., Lafon, P., & Candel, S., "Stochastic approach to noise modeling for free turbulent flows", AIAA J. 32(3), 455-463, 1994.
43. Viswanathan, K. and Sankar, L. N., “Toward the direct calculation of noise: fluid/acoustic coupled simulation”, AIAA J. 33(12), 2271–2279, 1995.
44. Long, L.N.,“A non conservative nonlinear flow field splitting method for 3-d unsteady fluid dynamics”, AIAA Paper 2000-1998, 2000.
45. Bogey, C., Bailly, C. and Juve, D., “Computation of flow noise using source terms in linearized Euler’s equations”, AIAA J. 40(2), 235-243, 2002.
46. Ewert, R., Schröder, W., “Acoustic perturbation equations based on flow decomposition via source filtering”, J. of Comp. Phys. 188(2), pp. 365 – 398, 2003.
47. Gabard G., Lefrancois, E., and Ben Tahar, M., “Aeroacoustic noise source simulations based on Galbrun's equation”, AIAA Paper 2004-2892, 2004.
48. Morfey, C. L., and Howell, G. P., “Nonlinear propagation of aircraft noise in the atmosphere,” AIAA Journal, Vol. 19, (8), 1981, pp. 986-992.
49. McInerny, S. A., Gee, K. L., Dowing, M., and James, M., “Acoustical Nonlinearities in Aircraft Flyover Data,” Paper AIAA 2007-3654, 13th AIAA/CEAS Aeroacoustics Conference, Rome, Italy, May 21-23, 2007.
50. Gee, K. L., Sparrow, V. W., James, M. M., Dowing, J. M., Hobbs, C. M., Gabrielson, T. B., and Atchley, A. A., “The role of nonlinear effects in the

propagation of noise from high-power jet aircraft," J. Acoust. Soc. Am., Vol. 123, (6), June 2008, pp. 4082-4093.

51. Gee, K. L., Sparrow, V. W., Gabrielson, T. B., and Atchley, A. A., "Nonlinear Modeling of F/A-18E Noise Propagation," Paper AIAA 2005-3089, 11th AIAA/CEAS Aeroacoustics Conference, Monterey, California, May 23-25, 2005.
52. Gee, K. L., Gabrielson, T. B., Atchely, A. A., and Sparrow, V. W., "Preliminary analysis of nonlinearity in military jet aircraft noise propagation," AIAA J. 43, 1398-1401 (2005).
53. Barger, R. L., "Theoretical prediction of nonlinear propagation effects on noise signatures generated by subsonic or supersonic propeller or rotor-blade tips," Report No. L-13388, NASA, Hampton, Virginia, 1980.
54. Isom, M. P., "Acoustic Shock Waves generated by a transonic helicopter blade," 36th AHS Annual Forum, Washington, DC, May 1980.
55. Papamoschou, D. and Mayoral, S., "Jet Noise Shielding for Advanced Hybrid Wing-Body Configuration", AIAA-2011-912, 49th AIAA Aerospace Sciences Meeting including the New Horizons Forum and Aerospace Exposition, Orlando, Florida, Jan. 4-7, 2011.
56. Schultz, K. J., Splettstoesser, W., Junker, B. and Wagner, W., A parametric windtunnel test on rotorcraft aerodynamics and aeroacoustics (HELISHAPE) – test procedures and representative results, 22nd European Rotorcraft Forum, Brighton, UK, 1996.
57. Schmitz, F. H., Boxwell, D. A., Splettstoesser, W. R. and Schultz, K. J., "Model-rotor high speed impulsive noise: Full-scale comparisons and parametric variations," Vertica 8, 395-442 (1984).
58. Yu, Y. H., "Rotor blade-vortex interaction noise," Progress in Aerospace Sciences 36, 97-115 (2000).
59. Cleveland, R. O., Hamilton, M. F., and Blackstock, D. T., "Time-domain modeling of finite-amplitude sound in relaxing fluids," J. Acoust. Soc. Am. 99, 3312-3318 (1996).
60. Lee, Y.-S., and Hamilton, M. F., "Time-domain modeling of pulsed finite-amplitude sound beams," J. Acoust. Soc. Am. 97, 906-917 (1995).

61. Gee, K. L., Sparrow, V. W., James, M. M., Dowing, J. M., and Hobbs, C. M., "Measurement and prediction of nonlinearity in outdoor propagation of periodic signals," J. Acoust. Soc. Am. 120, 2491-2499 (2006).
62. Cleveland, R. O., Chambers, J. P., Bass, H. E., Raspet, R., Blackstock, D. T., and Hamilton, M. F., "Comparison of computer codes for the propagation of sonic boom waveforms through isothermal atmospheres," J. Acoust. Soc. Am. 100, 3017-3027, (1996).
63. Boxwell, D. A., Schmitz, F. H., Splettstoesser, W. R., and Schultz, K. J., "Helicopter Model Rotor-Blade Vortex Interaction Impulsive Noise: Scalability and Parametric Variations," 10th European Rotorcraft Forum, The Hague, Netherlands, August 1984.
64. Schmitz, F. H., Boxwell, D. A., Lewy, D. A., and Dahan, C., "Model to full-scale comparisons of helicopter blade vortex interaction noise," J. American Helicopter Soc 29, 16-25 (1984).
65. American National Standards Institute, Committee S1, Acoustics, Method for Calculation of the Absorption of Sound by the Atmosphere, ANSI S1.26-1995, New York, NY: American National Standards Institute, September 1995.
66. Martin, R. M., and Hardin, J. C., "Spectral Characteristics of Rotor Blade/Vortex Interaction Noise," J. Aircraft 25, 62-68 (1988).
67. Schneider, O., and van der Wall, B. G., "Conditional averaging of microphone data from HART-II," Report No. IB 111-2006/37, DLR, Braunschweig, Germany.
68. Morgans, S., Karabasov, S. A., Dowling, A. P., and Hynes, T. P., "Transonic Helicopter Noise," AIAA J. 43, 1512-1524 (2005).
69. American National Standards Institute, Committee S1, Acoustics, "Method for Calculation of the Absorption of Sound by the Atmosphere", ANSI S1.26-1995, New York, NY: American National Standards Institute, September 1995.
70. Splettsoesser, W. R., Schultz, K. J., and Martin, R. M., "Rotor Blade-Vortex Interaction Impulsive noise Source localization", AIAA Journal, Vol. 28, (4), 1990, pp. 593-600.

71. Schmitz, F. H., and Sim, B. W., “Radiation and Directionality Characteristics of Helicopter Blade-Vortex Interaction Noise”, Journal of the American Helicopter Society, Vol. 48, (4), Oct. 2003, pp. 253–269.
72. Sim, B.W., Schmitz, F. H., and Aoyama, T., “Near/Far-Field Radiation Characteristics of Advancing Side Helicopter Blade-Vortex Interaction (BVI) Noise,” American Helicopter Society 56th Annual Forum Proceedings, Virginia Beach, VA, May 2-4, 2000.
73. Rogers, J. C., and Dai, R., “Signal Analysis of Helicopter Blade-Vortex-Interaction Acoustic Noise Data”, NASA Ames Research Center, Doc ID: 19990028654, 1998.
74. Martin, R. M., and Hardin, J. C., “Spectral Characteristics of Rotor Blade/Vortex Interaction Noise”, Journal of Aircraft, Vol. 25, (1), Jan. 1988, pp. 62-68.
75. Kallinderis, Y., "Hybrid grids and their applications", Chapter 35, Handbook of Grid Generation, Editors: J. F. Thompson, B. K. Soni, and N. P. Weatherill, CRC Press, 1999.
76. Kallinderis, Y., and Ahn, H. T., “Incompressible Navier-Stokes method with general hybrid meshes”, Journal of Computational Physics, Vol. 210, pp. 75-108, 2005.
77. Stoker, R., W., and Smith, M., J., “An evaluation of finite volume direct simulation and perturbation methods in CAA applications”, AIAA 93-0151, 31st Aerospace Sciences Meeting and Exhibit, Reno, NV, January 11-14, 1993.
78. Khan, M. M. S., “Computations of aeroacoustic fields using finite volume method,” Proceedings of the 1st IMACS Symposium on Computational Acoustics, New Haven, CT, August 1986.
79. Khan, M. M. S., Brown, W. H., and Ahuja, K. K., “Computational aeroacoustics as applied to the diffraction of sound by cylindrical bodies,” AIAA Journal, vol 25, no. 7, July 1987, p. 949-956.
80. Kallinderis, Y., Manolesos, M. and Menounou, P., “A flow/acoustics interaction method for the prediction of sound propagation”, Int. Journal of Aeroacoustics, Vol. 6, no. 2, pp. 171-197, 2007.

81. Ahn, H. T., and Kallinderis, Y, "Strongly coupled flow/structure interactions with a geometrically conservative ALE scheme on general hybrid meshes", Journal of Computational Physics, Vol. 219, pp. 671-696, 2006.
82. Kallinderis, Y., "Grid adaptation by redistribution and local embedding", 27th Computational Fluid Dynamics Lecture Series, VKI, Brussels, Belgium, March 1996.
83. Hirsch, C., Numerical Computation of Internal and External Flows. Vol. 1 and 2, Wiley, New York, 1990.
84. Jameson, A., Schmidt, W., and Turkel, E., "Numerical solutions of the Euler equations by finite volume methods using Runge-Kutta time-stepping schemes," AIAA Paper 81-1259, 1981.
85. Kallinderis, Y. and McMorris, H., "Magnitude of artificial dissipation for numerical simulations," AIAA Journal, 33, 1526-1529, 1995.
86. Kallinderis, Y., "A 3-D finite volume method for the Navier-Stokes equations with adaptive hybrid grids", Applied Numerical Mathematics, 20, p. 387-406, 1996.
87. Hixon, R., "Radiation and wall boundary conditions for computational aeroacoustics: A review," International Journal of Computational Fluid Dynamics, vol 18 (6), August 2004, p. 523-531.
88. Crocker, M. J., Handbook of Acoustics, Wiley-Interscience Publication, 1998.
89. Kallinderis, Y., and Kavouklis, C., "A dynamic adaptation scheme for general hybrid meshes", Comp. Meth. in Appl. Mech. and Engng., Vol 194, pp. 5019-5050, 2005.
90. Friedlander, F. G., Sound Pulses, Cambridge University Press, 1958
91. Brooks, T. F., Jolly, J. R. and Marcollini, M. A., Helicopter Main Rotor Noise: Determination of Source Contributions using Scaled Model Data, NASA Technical Paper 2825, August 1988.
92. Glegg, S. A. L., Prediction of Blade Wake Interaction Noise Based on a Turbulent Vortex Model, AIAA Journal, Vol. 29 (10), 1991.
93. Amiet, R. K., Acoustic Radiation from an Airfoil in a Turbulent Stream, Journal of Sound and Vibration, Vol. 41 (4), pp 407 - 420, 1975.

94. Wittmer, K. S., Devenport, W. J. and Glegg, S. A. L., Perpendicular Blade Vortex Interaction, AIAA Journal, Sept 1995, pp 1667-1674.
95. Glegg, S. A. L., Witmmer, K. S., Devenport, W. J. and Pope, D. S., Broadband Helicopter Noise, AHS Specialists' Meeting for Rotorcraft Acoustics and Aerodynamics, Williamsburg, Virginia, Oct 1997.
96. Brooks T. F., Burley C. L., Blade Wake Interaction Noise for a Main Rotor, Journal of the AHS, 49 (1), 2004, pp 11 – 27
97. Burley, C. L., Brooks, T. F., Splettstoesser, W. R., Schultz, K.-J., Kube, R., Bucholtz, H., Wagner, W., and Weitmeyer, W., Blade Wake Interaction Noise for a BO-105 Model Main Rotor, AHS Technical Specialists' Meeting for Rotorcraft Acoustics and Aerodynamics, Williamsburg, VA, Oct 1997.
98. Brooks, T. F., and Burley, C. L., Rotor Broadband Noise prediction with Comparison to Model Data, AIAA Paper No. 2001-2210, 2001.
99. Burley, C. L., and Brooks, T. F., Rotor Broadband Noise prediction with Comparison to Model Data, Journal of the AHS, 49 (1), 2004.
100. Brezillion, J., Prieur, J. and Rahier, J., Investigation on Broadband Helicopter Noise, AHS Rotorcraft Acoustics and Aerodynamics Specialists Meeting, Williamsburg, Virginia, Oct 1997.
101. Bouchet, E. and Rahier, G., Structure of the Blade Pressure Fluctuations Generated by Helicopter Rotor Blade-Wake Interaction, 56th AHS Annual Forum, Virginia Beach, Virginia, May 2000.
102. Devenport, W. J., Vogel, C. M. and Zsoldos, J. S., Flow structure produced by the interaction and merger of a pair of co-rotating wing-tip vortices, J. Fluid Mech, vol 394, pp. 357-377, 1999.
103. Mauffrey, Y., Rahier, G. and Prieur, J., Numerical Investigation on Blade/Wake-Interaction Noise Generation, Journal of Aircraft, Vol. 46, No. 5, 2009.
104. Le Dizes, S., and Laporte F., Theoritical predictions for the elliptical instability in a two-vortex flow, J. Fluid Mech., Vol. 471, pp 169-201, 2002.
105. Meunier, P., and Leweke, T., Elliptic Instability of a Co-rotating Vortex Pair, J. Fluid Mech., Vol. 533, pp 125-159, 2005.
106. Schneider, O. and Van der Wall, B.G., Comparison of Simple and Conditional Averaging Methodology Based on Results of the HART II Wind Tunnel Test,

International Forum on Rotorcraft Multidisciplinary Technology, Seoul, Korea, (2007).

107. Brooks, T. F., Effect of signal jitter on the spectrum of impulsive noise, NASA Technical Memorandum 100477, June 1987.
108. Splettsoesser, W. R., Schultz, K. J. and Martin, R. M., Rotor Blade-Vortex Interaction Impulsive noise Source localization, AIAA Journal, Vol. 28, 593-600, April 1990.
109. Marcolini, M. A. and Brooks, T. F., Rotor Noise Measurement Using a Directional Microphone Array, AIAA Paper 87-2746, 1987.
110. Martin, R. M. and Hardin, J. C., "Spectral Characteristics of Rotor Blade/Vortex Interaction Noise", J. Aircraft, Vol.25, No. 1, 1987.
111. Egolf, T. A. and Landgrebe, A. J., Helicopter Rotor Wake Geometry and its Influence in Forward Flight, Volume II – Wake Geometry Charts, NASA CR 3727, 1983.
112. Dritschel, D. G., and Waugh, D. W., Quantification of the inelastic interaction of unequal vortices in two-dimensional vortex dynamics, Phys. Fluids , Vol. 4, 1992.
113. Trieling, R. R., Velasco Fuentes, O. U., and van Heijst, G. J. F., Interaction of two unequal co-rotaring vortices, Phys. Fluids, Vol. 17, 2005.
114. Govindaraju, S. P., and Saffman, P. G., Flow in a Turbulent Trailing Vortex, Phys. Fluids, Vol. 14 (10), 1971.

APPENDICES

A. Derivation of 3D Nonlinear Perturbation Equations

The 3D Compressible Euler equations in conservative form are:

$$q_t + F_x + G_y + H_z = 0 \tag{A.1}$$

$$q = \begin{bmatrix} \rho \\ \rho u \\ \rho v \\ \rho w \\ e \end{bmatrix}, \quad F = \begin{bmatrix} \rho u \\ \rho u^2 + p \\ \rho uv \\ \rho uw \\ (e+p)u \end{bmatrix}, \quad G = \begin{bmatrix} \rho v \\ \rho vu \\ \rho v^2 + p \\ \rho vw \\ (e+p)v \end{bmatrix}, \quad H = \begin{bmatrix} \rho w \\ \rho wu \\ \rho wv \\ \rho w^2 + p \\ (e+p)w \end{bmatrix}$$

The total energy per unit volume is defined as:

$$e = \rho\left[C_v + \frac{1}{2}\left(u^2 + v^2 + w^2\right)\right] = \frac{p}{\gamma - 1} + \frac{1}{2}\rho\left(u^2 + v^2 + w^2\right)$$

To derive the nonlinear disturbance equations, the flow vector q is split into its mean value $\bar{q}$ and a perturbation q':

$$q = \bar{q} + q' \tag{A.2}$$

Or

$$\rho = \bar{\rho} + \rho'$$
$$u = \bar{u} + u'$$
$$v = \bar{v} + v'$$
$$p = \bar{p} + p'$$

For the conservative form of the perturbations equations Eq.(A.2) is substituted in the Euler equations Eq.(A.1) as follows.

- ***Continuity equation:***

$$\frac{\partial}{\partial t}\left[\bar{\rho}+\rho'\right]+\frac{\partial}{\partial x}\left[\left(\bar{\rho}+\rho'\right)\left(\bar{u}+u'\right)\right]+\frac{\partial}{\partial y}\left[\left(\bar{\rho}+\rho'\right)\left(\bar{v}+v'\right)\right]+\frac{\partial}{\partial z}\left[\left(\bar{\rho}+\rho'\right)\left(\bar{w}+w'\right)\right]=0\Rightarrow$$

$$\frac{\partial}{\partial t}\left[\bar{\rho}+\rho'\right]+\frac{\partial}{\partial x}\left[\bar{\rho}\bar{u}+\rho'\bar{u}+\bar{\rho}u'+\rho'u'\right]+$$
$$+\frac{\partial}{\partial y}\left[\bar{\rho}\bar{v}+\rho'\bar{v}+\bar{\rho}v'+\rho'v'\right]+\frac{\partial}{\partial z}\left[\bar{\rho}\bar{w}+\rho'\bar{w}+\bar{\rho}w'+\rho'w'\right]=0\Rightarrow$$

$$\frac{\partial}{\partial t}\left[\bar{\rho}\right]+\frac{\partial}{\partial x}\left[\bar{\rho}\bar{u}\right]+\frac{\partial}{\partial y}\left[\bar{\rho}\bar{v}\right]+\frac{\partial}{\partial z}\left[\bar{\rho}\bar{w}\right]+$$
$$+\frac{\partial}{\partial t}\left[\rho'\right]+\frac{\partial}{\partial x}\left[\rho'\bar{u}+\bar{\rho}u'+\rho'u'\right] \qquad \text{(A.3)}$$
$$+\frac{\partial}{\partial y}\left[\rho'\bar{v}+\bar{\rho}v'+\rho'v'\right]+\frac{\partial}{\partial z}\left[\rho'\bar{w}+\bar{\rho}w'+\rho'w'\right]=0$$

The first line of the Eq.(A.3) is the convective fluxes.

The following assumptions are made:

i. The magnitude of the time and spatial variations of the acoustic field do not affect the flow quantities appreciably, thus the mean convective fluxes can be set to zero.
ii. Equalling the perturbation part to zero also assumes that the flow variables do not affect the perturbation variables, which means that flow generated sound is ignored.

It is:

$$\frac{\partial}{\partial t}[\rho'] + \frac{\partial}{\partial x}[\rho'\bar{u} + \bar{\rho}u'] + \frac{\partial}{\partial y}[\rho'\bar{v} + \bar{\rho}v'] + \frac{\partial}{\partial z}[\rho'\bar{w} + \bar{\rho}w'] + \\ + \frac{\partial}{\partial x}[\rho'u'] + \frac{\partial}{\partial y}[\rho'v'] + \frac{\partial}{\partial z}[\rho'w'] = 0 \tag{A.4}$$

The first line of Eq.(A.4) is the linear flux terms and the second line is the nonlinear flux terms.

- ***X-momentum equation***

$$\frac{\partial}{\partial t}\left[(\bar{\rho}+\rho')(\bar{u}+u')\right] + \frac{\partial}{\partial x}\left[(\bar{\rho}+\rho')(\bar{u}+u')^2 + (\bar{p}+p')\right] + \\ + \frac{\partial}{\partial y}\left[(\bar{\rho}+\rho')(\bar{v}+v')(\bar{u}+u')\right] + \frac{\partial}{\partial z}\left[(\bar{\rho}+\rho')(\bar{w}+w')(\bar{u}+u')\right] = 0 \Rightarrow$$

$$\frac{\partial}{\partial t}\left[\bar{\rho}\bar{u} + \rho'\bar{u} + \bar{\rho}u' + \rho'u'\right] + \\ + \frac{\partial}{\partial x}\left[\left(\bar{\rho}\bar{u}^2 + \rho'\bar{u}^2 + \bar{\rho}u'^2 + \rho'u'^2 + 2\bar{u}u'\bar{\rho} + 2\bar{u}u'\rho'\right) + (\bar{p}+p')\right] + \\ + \frac{\partial}{\partial y}\left[(\bar{\rho}\bar{v}\bar{u} + \rho'\bar{v}\bar{u} + \bar{\rho}v'\bar{u} + \rho'v'\bar{u}) + (\bar{\rho}\bar{v}u' + \rho'\bar{v}u' + \bar{\rho}v'u' + \rho'v'u')\right] + \\ + \frac{\partial}{\partial z}\left[(\bar{\rho}\bar{w}\bar{u} + \rho'\bar{w}\bar{u} + \bar{\rho}w'\bar{u} + \rho'w'\bar{u}) + (\bar{\rho}\bar{w}u' + \rho'\bar{w}u' + \bar{\rho}w'u' + \rho'w'u')\right] = 0$$

Making the same assumption as for the density equation, it is:

$$\frac{\partial}{\partial t}\left[\rho'\bar{u} + \bar{\rho}u' + \rho'u'\right] + \\ + \frac{\partial}{\partial x}\left[\rho'\bar{u}^2 + 2\bar{u}u'\bar{\rho} + p'\right] + \frac{\partial}{\partial y}\left[\rho'\bar{v}\bar{u} + \bar{\rho}v'\bar{u} + \bar{\rho}\bar{v}u'\right] + \frac{\partial}{\partial z}\left[\rho'\bar{w}\bar{u} + \bar{\rho}w'\bar{u} + \bar{\rho}\bar{w}u'\right] + \\ + \frac{\partial}{\partial x}\left[2\rho'u'\bar{u} + \bar{\rho}u'^2 + \rho'u'^2\right] + \frac{\partial}{\partial y}\left[\bar{\rho}u'v' + \rho'v'\bar{u} + \rho'u'\bar{v} + \rho'u'v'\right] + \\ + \frac{\partial}{\partial z}\left[\bar{\rho}u'w' + \rho'w'\bar{u} + \rho'u'\bar{w} + \rho'u'w'\right] = 0 \tag{A.5}$$

The third and fourth lines of Eq.(A.5) are the nonlinear flux terms. The rest equations are derived in a similar manner.

- ***Y-momentum equation***

$$\frac{\partial}{\partial t}\left[(\bar{\rho}+\rho')(\bar{v}+v')\right]+\frac{\partial}{\partial x}\left[(\bar{\rho}+\rho')(\bar{u}+u')(\bar{v}+v')\right]+$$
$$+\frac{\partial}{\partial y}\left[(\bar{\rho}+\rho')(\bar{v}+v')^2+(\bar{p}+p')\right]+\frac{\partial}{\partial z}\left[(\bar{\rho}+\rho')(\bar{w}+w')(\bar{v}+v')\right]=0\Rightarrow$$

$$\frac{\partial}{\partial t}\left[\bar{\rho}\bar{v}+\rho'\bar{v}+\bar{\rho}v'+\rho'v'\right]+$$
$$+\frac{\partial}{\partial x}\left[(\bar{\rho}\bar{u}\bar{v}+\rho'\bar{u}\bar{v}+\bar{\rho}u'\bar{v}+\rho'u'\bar{v})+(\bar{\rho}\bar{u}v'+\rho'\bar{u}v'+\bar{\rho}u'v'+\rho'u'v')\right]+$$
$$+\frac{\partial}{\partial y}\left[\left(\bar{\rho}\bar{v}^2+\rho'\bar{v}^2+\bar{\rho}v'^2+\rho'v'^2+\bar{\rho}2\bar{v}v'+\rho'2\bar{v}v'\right)+(\bar{p}+p')\right]+$$
$$+\frac{\partial}{\partial z}\left[(\bar{\rho}\bar{w}\bar{v}+\rho'\bar{w}\bar{v}+\bar{\rho}w'\bar{v}+\rho'w'\bar{v})+(\bar{\rho}\bar{w}v'+\rho'\bar{w}v'+\bar{\rho}w'v'+\rho'w'v')\right]=0\Rightarrow$$

$$\frac{\partial}{\partial t}\left[\rho'\bar{v}+\bar{\rho}v'+\rho'v'\right]+$$
$$+\frac{\partial}{\partial x}\left[\bar{\rho}\bar{u}v'+\bar{\rho}\bar{v}u'+\rho'\bar{u}\bar{v}\right]+\frac{\partial}{\partial y}\left[\rho'\bar{v}^2+2\bar{\rho}\bar{v}v'+p'\right]+\frac{\partial}{\partial z}\left[\rho'\bar{w}\bar{v}+\bar{\rho}w'\bar{v}+\bar{\rho}\bar{w}v'\right]+$$
$$+\frac{\partial}{\partial x}\left[\bar{\rho}u'v'+\rho'v'\bar{u}+\rho'u'\bar{v}+\rho'u'v'\right]+\frac{\partial}{\partial y}\left[2\rho'\bar{v}v'+\bar{\rho}v'^2+\rho'v'^2\right]+$$
$$+\frac{\partial}{\partial z}\left[\bar{\rho}v'w'+\rho'w'\bar{v}+\rho'v'\bar{w}+\rho'v'w'\right]=0 \tag{A.6}$$

- ***Z-momentum equation***

$$\frac{\partial}{\partial t}\left[(\bar{\rho}+\rho')(\bar{w}+w')\right]+\frac{\partial}{\partial x}\left[(\bar{\rho}+\rho')(\bar{u}+u')(\bar{w}+w')\right]+$$
$$+\frac{\partial}{\partial y}\left[(\bar{\rho}+\rho')(\bar{v}+v')(\bar{w}+w')\right]+\frac{\partial}{\partial z}\left[(\bar{\rho}+\rho')(\bar{w}+w')^2+(\bar{p}+p')\right]=0\Rightarrow$$

$$\frac{\partial}{\partial t}\left[\bar{\rho}\bar{w}+\rho'\bar{w}+\bar{\rho}w'+\rho'w'\right]+$$
$$+\frac{\partial}{\partial x}\left[(\bar{\rho}\bar{u}\bar{w}+\rho'\bar{u}\bar{w}+\bar{\rho}u'\bar{w}+\rho'u'\bar{w})+(\bar{\rho}\bar{u}w'+\rho'\bar{u}w'+\bar{\rho}u'w'+\rho'u'w')\right]+$$
$$+\frac{\partial}{\partial y}\left[(\bar{\rho}\bar{v}\bar{w}+\rho'\bar{v}\bar{w}+\bar{\rho}v'\bar{w}+\rho'v'\bar{w})+(\bar{\rho}\bar{v}w'+\rho'\bar{v}w'+\bar{\rho}v'w'+\rho'v'w')\right]+$$
$$+\frac{\partial}{\partial z}\left[\left(\bar{\rho}\bar{w}^2+\rho'\bar{w}^2+\bar{\rho}w'^2+\rho'w'^2+\bar{\rho}2\bar{w}w'+\rho'2\bar{w}w'\right)+(\bar{p}+p')\right]=0\Rightarrow$$

$$\frac{\partial}{\partial t}\left[\rho'\bar{w}+\bar{\rho}w'+\rho'w'\right]+$$
$$+\frac{\partial}{\partial x}\left[\bar{\rho}\bar{u}w'+\bar{\rho}\bar{w}u'+\rho'\bar{u}\bar{w}\right]+\frac{\partial}{\partial y}\left[\bar{\rho}\bar{v}w'+\bar{\rho}\bar{w}v'+\rho'\bar{v}\bar{w}\right]+\frac{\partial}{\partial z}\left[\rho'\bar{w}^2+2\bar{\rho}\bar{w}w'+p'\right]+$$
$$+\frac{\partial}{\partial x}\left[\bar{\rho}u'w'+\rho'w'\bar{u}+\rho'u'\bar{w}+\rho'u'w'\right]+\frac{\partial}{\partial y}\left[\bar{\rho}v'w'+\rho'w'\bar{v}+\rho'v'\bar{w}+\rho'v'w'\right]+$$
$$+\frac{\partial}{\partial z}\left[2\rho'\bar{w}w'+\bar{\rho}w'^2+\rho'w'^2\right]=0$$

(A.7)

- ***Energy equation***

$$\frac{\partial}{\partial t}\left[\bar{e}+e'\right]+\frac{\partial}{\partial x}\left[(\bar{e}+e'+\bar{p}+p')(\bar{u}+u')\right]+\frac{\partial}{\partial y}\left[(\bar{e}+e'+\bar{p}+p')(\bar{v}+v')\right]+$$
$$+\frac{\partial}{\partial z}\left[(\bar{e}+e'+\bar{p}+p')(\bar{w}+w')\right]=0\Rightarrow$$

$$\frac{\partial}{\partial t}\left[\bar{e}+e'\right]+\frac{\partial}{\partial x}\left[\overline{eu}+e'\bar{u}+\bar{p}\bar{u}+p'\bar{u}+\bar{e}u'+e'u'+\bar{p}u'+p'u'\right]+$$
$$\frac{\partial}{\partial y}\left[\overline{ev}+e'\bar{v}+\bar{p}\bar{v}+p'\bar{v}+\bar{e}v'+e'v'+\bar{p}v'+p'v'\right]+$$
$$+\frac{\partial}{\partial z}\left[\overline{ew}+e'\bar{w}+\bar{p}\bar{w}+p'\bar{w}+\bar{e}w'+e'w'+\bar{p}w'+p'w'\right]=0\Rightarrow$$

$$\frac{\partial}{\partial t}\left[e'\right]+$$
$$+\frac{\partial}{\partial x}\left[e'\bar{u}+p'\bar{u}+\bar{e}u'+\bar{p}u'\right]+\frac{\partial}{\partial y}\left[e'\bar{v}+p'\bar{v}+\bar{e}v'+\bar{p}v'\right]+\frac{\partial}{\partial z}\left[e'\bar{w}+p'\bar{w}+\bar{e}w'+\bar{p}w'\right]+$$
$$+\frac{\partial}{\partial x}\left[u'e'+u'p'\right]+\frac{\partial}{\partial y}\left[v'e'+v'p'\right]+\frac{\partial}{\partial z}\left[w'e'+w'p'\right]=0 \tag{A.8}$$

- ***3D Nonlinear perturbation Equations (NPE)***

From Eqs. (A.4) - (A.8), the conservation form of 3D NPE is derived:

$$\boxed{\frac{\partial q'}{\partial t}+\frac{\partial F'}{\partial x}+\frac{\partial G'}{\partial y}+\frac{\partial H'}{\partial z}+\frac{\partial F'_n}{\partial x}+\frac{\partial G'_n}{\partial y}+\frac{\partial H'_n}{\partial z}=0} \tag{A.9}$$

where:

$$q'=\begin{bmatrix}\rho'\\ \bar{\rho}u'+\rho'\bar{u}+\rho'u'\\ \bar{\rho}v'+\rho'\bar{v}+\rho'v'\\ \bar{\rho}w'+\rho'\bar{w}+\rho'w'\\ e'\end{bmatrix}$$

$$F'=\begin{bmatrix}\bar{\rho}u'+\rho'\bar{u}\\ \rho'\bar{u}^2+2\bar{\rho}\bar{u}u'+p'\\ \bar{\rho}\bar{u}v'+\bar{\rho}u'\bar{v}+\rho'\overline{uv}\\ \bar{\rho}\bar{u}w'+\bar{\rho}u'\bar{w}+\rho'\overline{uw}\\ \left(\bar{e}+\bar{p}\right)u'+\left(e'+p'\right)\bar{u}\end{bmatrix},$$

$$G' = \begin{bmatrix} \bar{\rho}v' + \rho'\bar{v} \\ \bar{\rho}\bar{v}u' + \bar{\rho}v'\bar{u} + \rho'\bar{v}\bar{u} \\ \rho'\bar{v}^2 + 2\bar{\rho}\bar{v}v' + p' \\ \bar{\rho}\bar{v}w' + \bar{\rho}v'\bar{w} + \rho'\bar{v}\bar{w} \\ \left(\bar{e} + \bar{p}\right)v' + \left(e' + p'\right)\bar{v} \end{bmatrix},$$

$$H' = \begin{bmatrix} \bar{\rho}w' + \rho'\bar{w} \\ \bar{\rho}\bar{w}u' + \bar{\rho}w'\bar{u} + \rho'\bar{w}\bar{u} \\ \bar{\rho}\bar{w}v' + \bar{\rho}w'\bar{v} + \rho'\bar{w}\bar{v} \\ \rho'\bar{w}^2 + 2\bar{\rho}\bar{w}w' + p' \\ \left(\bar{e} + \bar{p}\right)w' + \left(e' + p'\right)\bar{w} \end{bmatrix},$$

$$F_n' = \begin{bmatrix} \rho'u' \\ 2\rho'u'\bar{u} + \bar{\rho}u'^2 + \rho'u'^2 \\ \bar{\rho}u'v' + \rho'v'\bar{u} + \rho'u'\bar{v} + \rho'u'v' \\ \bar{\rho}u'w' + \rho'w'\bar{u} + \rho'u'\bar{w} + \rho'u'w' \\ u'\left(e' + p'\right) \end{bmatrix},$$

$$G_n' = \begin{bmatrix} \rho'v' \\ \bar{\rho}u'v' + \rho'v'\bar{u} + \rho'u'\bar{v} + \rho'u'v' \\ 2\rho'\bar{v}v' + \bar{\rho}v'^2 + \rho'v'^2 \\ \bar{\rho}v'w' + \rho'w'\bar{v} + \rho'v'\bar{w} + \rho'v'w' \\ v'\left(e' + p'\right) \end{bmatrix},$$

$$H_n' = \begin{bmatrix} \rho'w' \\ \bar{\rho}u'w' + \rho'w'\bar{u} + \rho'u'\bar{w} + \rho'u'w' \\ \bar{\rho}v'w' + \rho'w'\bar{v} + \rho'v'\bar{w} + \rho'v'w' \\ 2\rho'\bar{w}w' + \bar{\rho}w'^2 + \rho'w'^2 \\ w'\left(e' + p'\right) \end{bmatrix},$$

where:

$$e' = \frac{p'}{\gamma - 1} + \left(\bar{\rho} + \rho'\right)\left(u'\bar{u} + v'\bar{v} + w'\bar{w}\right) + \frac{1}{2}\left(\bar{\rho} + \rho'\right)\left(u'^2 + v'^2 + w'^2\right) + \frac{1}{2}\rho'\left(\bar{u}^2 + \bar{v}^2 + \bar{w}^2\right)$$

B. Derivation of Riemann Invariants for Perturbation Equations

Starting from the 3D Nonlinear Perturbation Equations (NPE) it is assumed that at locally boundary:

- 1-D propagation
- Uniform flow
- Linear propagation

The 3D NPE then simplify to:

Continuity Eq.: $$\frac{1}{\bar{\rho}}\frac{\partial \rho'}{\partial t}+\bar{u}\frac{1}{\bar{\rho}}\frac{\partial \rho'}{\partial x}+\frac{\partial u'}{\partial x}=0$$

X-momentum Eq.: $$\frac{\partial u'}{\partial t}+\bar{u}\frac{\partial u'}{\partial x}+\frac{1}{\bar{\rho}}\frac{\partial p'}{\partial x}=0$$

Y-momentum Eq.: $$\frac{\partial v'}{\partial t}+\bar{u}\frac{\partial v'}{\partial x}=0$$

Z-momentum Eq.: $$\frac{\partial w'}{\partial t}+\bar{u}\frac{\partial w'}{\partial x}=0$$

Energy Eq. (entropy form): $$\frac{\partial s'}{\partial t}+\bar{u}\frac{\partial s'}{\partial x}=0$$

- *Relate* ρ' *to* c *and* s'

$$c^2=\frac{\gamma p}{\rho}=\gamma\rho^{\gamma-1}e^{(s+s')}$$

Substitute: $\rho=\bar{\rho}+\rho'$

$$c^2=\gamma\left(\bar{\rho}+\rho'\right)^{\gamma-1}e^{(s+s')}\Rightarrow$$

$$2c\,dc=\gamma\left(\gamma-1\right)\left(\bar{\rho}+\rho'\right)^{\gamma-2}e^{(s+s')}\,d\rho'+\gamma\left(\bar{\rho}+\rho'\right)^{\gamma-1}e^{(s+s')}\,ds'\Rightarrow$$

$$2c\,dc=\gamma\left(\gamma-1\right)\left(\bar{\rho}+\rho'\right)^{\gamma-2}e^{(s+s')}\,d\rho'+\gamma\left(\bar{\rho}+\rho'\right)^{\gamma-1}e^{(s+s')}\,ds'\Rightarrow$$

$$\frac{2\,dc}{c} = \frac{(\gamma-1)}{\bar{\rho}+\rho'} d\rho' + ds' \Rightarrow$$

$$\frac{1}{\bar{\rho}+\rho'} d\rho' = \frac{2}{(\gamma-1)}\frac{dc}{c} - \frac{ds'}{(\gamma-1)} \Rightarrow \text{ using: } \bar{\rho}+\rho' \simeq \bar{\rho}$$

$$\frac{1}{\bar{\rho}} d\rho' = \frac{2}{(\gamma-1)}\frac{dc}{c} - \frac{ds'}{(\gamma-1)} \qquad \text{(B.1)}$$

- *Relate* p' *to* c *and* s

$$c^2 = \frac{\gamma p}{\rho} \Rightarrow$$

$$c^2 = \frac{\gamma(\bar{p}+p')}{(\bar{\rho}+\rho')} \Rightarrow$$

$$c^2 dp' = \frac{\gamma(\bar{p}+p')}{(\bar{\rho}+\rho')} dp' \text{ using: } \bar{\rho}+\rho' \simeq \bar{\rho} \text{ and } \bar{p}+p' \simeq \bar{p}$$

$$c^2 dp' = \frac{\gamma \bar{p}}{\bar{\rho}} dp' \qquad \text{(B.2)}$$

$$(\bar{p}+p') = (\bar{\rho}+\rho')^{\gamma} e^{(s+s')} \Rightarrow$$

$$dp' = \gamma(\bar{\rho}+\rho')^{\gamma-1} e^{(s+s')} d\rho' + (\bar{\rho}+\rho')^{\gamma} e^{(s+s')} ds' \Rightarrow$$

$$\frac{dp'}{\bar{p}+p'} = \gamma \frac{1}{(\bar{\rho}+\rho')} d\rho' + ds' \Rightarrow$$

$$\frac{dp'}{\bar{p}} = \gamma \frac{1}{\bar{\rho}} d\rho' + ds' \qquad \text{(B.3)}$$

(B.2), (B.3) => $\frac{dp'}{\bar{\rho}} = \frac{c^2}{\gamma}\left(\gamma \frac{d\rho'}{\bar{\rho}} + ds'\right) \Rightarrow$ using (B.1)

$$\frac{dp'}{\bar{\rho}} = \frac{c^2}{\gamma}\left(\gamma\left(\frac{2}{(\gamma-1)}\frac{dc}{c} - \frac{ds'}{(\gamma-1)}\right) + ds'\right) \Rightarrow$$

$$\frac{dp'}{\bar{\rho}} = \frac{c^2}{\gamma}\left(\frac{2\gamma}{(\gamma-1)}\frac{dc}{c} - \gamma\frac{ds'}{(\gamma-1)} + ds'\right) = \frac{2c}{(\gamma-1)}dc - \frac{c^2 ds'}{(\gamma-1)} + \frac{c^2}{\gamma}ds' \Rightarrow$$

$$\frac{dp'}{\bar{\rho}} = \frac{2c}{(\gamma-1)}dc - \frac{c^2}{\gamma(\gamma-1)}ds' \qquad \text{(B.4)}$$

- *X-momentum:*

$$\frac{\partial u'}{\partial t} + \bar{u}\frac{\partial u'}{\partial x} + \frac{1}{\bar{\rho}}\frac{\partial p'}{\partial x} = 0 \Rightarrow + \text{(B.4)}$$

$$\frac{\partial u'}{\partial t} + \bar{u}\frac{\partial u'}{\partial x} + \frac{2c}{(\gamma-1)}\frac{\partial c}{\partial x} - \frac{c^2}{\gamma(\gamma-1)}\frac{\partial s'}{\partial x} = 0 \qquad \text{(B.5)}$$

- *Continuity*

$$\frac{1}{\bar{\rho}}\frac{\partial \rho'}{\partial t} + \bar{u}\frac{1}{\bar{\rho}}\frac{\partial \rho'}{\partial x} + \frac{\partial u'}{\partial x} = 0 \Rightarrow \text{ using (B.1)}$$

$$\frac{2}{(\gamma-1)c}\frac{\partial c}{\partial t} - \frac{1}{(\gamma-1)}\frac{\partial s'}{\partial t} + \bar{u}\left(\frac{2}{(\gamma-1)c}\frac{\partial c}{\partial x} - \frac{1}{(\gamma-1)}\frac{\partial s'}{\partial x}\right) + \frac{\partial u'}{\partial x} = 0 \Rightarrow$$

Using energy equation (entropy form):

$$\frac{2}{(\gamma-1)}\frac{\partial c}{\partial t} + \bar{u}\frac{2}{(\gamma-1)}\frac{\partial c}{\partial x} + c\frac{\partial u'}{\partial x} = 0 \qquad \text{(B.6)}$$

$\text{(B.5)} \pm \text{(B.6)} \Rightarrow$

$$\frac{\partial}{\partial t}\left(u' \pm \frac{2}{(\gamma-1)}c\right) + \bar{u}\frac{\partial}{\partial x}\left(u' \pm \frac{2}{(\gamma-1)}c\right) + c\frac{\partial}{\partial x}\left(\frac{2c}{\gamma-1} \pm u'\right) - \frac{c^2}{\gamma(\gamma-1)}\frac{\partial s'}{\partial x} = 0 \Rightarrow$$

$$\frac{\partial}{\partial t}\left(u' \pm \frac{2}{(\gamma-1)}c\right) + \bar{u}\frac{\partial}{\partial x}\left(u' \pm \frac{2}{(\gamma-1)}c\right) + c\frac{\partial}{\partial x}\left(\frac{2c}{\gamma-1} \pm u'\right) - \frac{c^2}{\gamma(\gamma-1)}\frac{\partial s'}{\partial x} = 0 \Rightarrow$$

$$\frac{\partial}{\partial t}\left(u' \pm \frac{2}{(\gamma-1)}c\right) + (\bar{u} \pm c)\frac{\partial}{\partial x}\left(u' \pm \frac{2}{(\gamma-1)}c\right) - \frac{c^2}{\gamma(\gamma-1)}\frac{\partial s'}{\partial x} = 0 \qquad \text{(B.7)}$$

Assuming that $\frac{\partial s'}{\partial x} = 0$ at the boundary, Eq.(B.7) gives:

$$\frac{\partial}{\partial t}\left(u' \pm \frac{2}{(\gamma - 1)} c \right) + (\bar{u} \pm c) \frac{\partial}{\partial x}\left(u' \pm \frac{2}{(\gamma - 1)} c \right) = 0 \qquad \text{(B.8)}$$

According to Eq.(B.8) the Riemann invariants are defined as:

$$\boxed{J^{+} = u' + \frac{2}{(\gamma - 1)} c} \qquad \text{and} \qquad \boxed{J^{-} = u' - \frac{2}{(\gamma - 1)} c}$$

C. Monopole Orientation in Computational Grid and Analytic Solution

The first step of introducing a monopole in computational space is to orientate its boundaries in an arbitrary mesh. The required monopole dimensions are its center coordinates and its radius. The algorithm that is used for the monopole orientation selects the grid points being closer to the ideal monopole sphere in order to form the polyhedral surface where the monopole analytic solution will be applied.

Figure C-1 shows the monopole orientation for 3 different density hexahedral grids. For all cases the monopole center is positioned at the center of the axis (0, 0, 0) and its radius is 0.05 units.

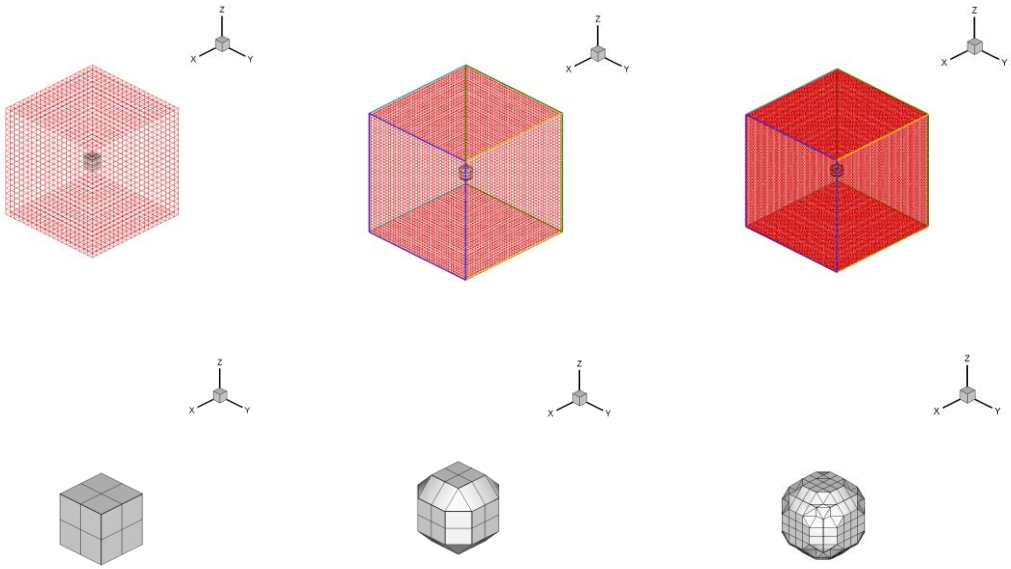

Figure C-1: Monopole orientation in hexahedral grids of various densities.

It can be seen that for the coarse grid case, where the monopole radius equals grid's discretization, the monopole is approximated with a hexahedral. From the above results it can be seen that as the grid gets denser, the surface approximates a sphere and thus the modelling would get more and more accurate compared to an ideal monopole. Figure C-2 shows the monopole surface in an arbitrary hybrid grid.

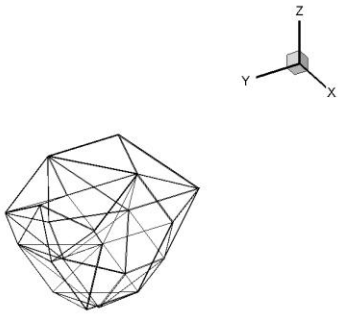

Figure C-2: Monopole orientation in an arbitrary hybrid grid.

Point Monopole Analytic Solution:

For a point at distance R from the center of an acoustic monopole, it is:

$$p'(R,\tau) = p_0 \frac{r}{R}\cos(\omega\tau)$$

$$U'(R,\tau) = \frac{p_0}{\rho c}\frac{r}{R}\left(\cos(\omega\tau) + \frac{1}{kR}\sin(\omega\tau)\right)$$

$$\rho'(R,\tau) = \frac{p_0}{c^2}\frac{r}{R}\cos(\omega\tau) \Rightarrow \ \rho'(R,\tau) = \frac{p'(R,\tau)}{c^2}$$

where:

$U'(R,\tau)$: The measure of the total velocity vector connecting the monopole center with the desired point

$k = \frac{\omega}{c}$: Wavenumber

p_0: Monopole acoustic pressure amplitude at the vibrating surface

ρ: Density of the medium

c: Speed of sound of the medium

r: Monopole spherical surface radius

$\tau = t - \frac{R}{c + U_{flow}}$: Retarded time

U_{flow}: Relative flow velocity to propagation path

D. Friedlander Analytic Solution

Friedlander in 1958 obtained the solution for a plane unit step function incident on a rigid barrier modelled as a half plane.

- If the angle between an incident sound pulse and the vertical barrier is ϕ_0 then, according to Friedlander, the space around the barrier is divided into three regions which are shown in Figure D-1.
- Region 1 for $0 < \phi < \pi - \phi_0$
- Region 2 for $\pi - \phi_0 < \phi < \pi + \phi_0$
- Region 3 for $\pi + \phi_0 < \phi < 2\pi$

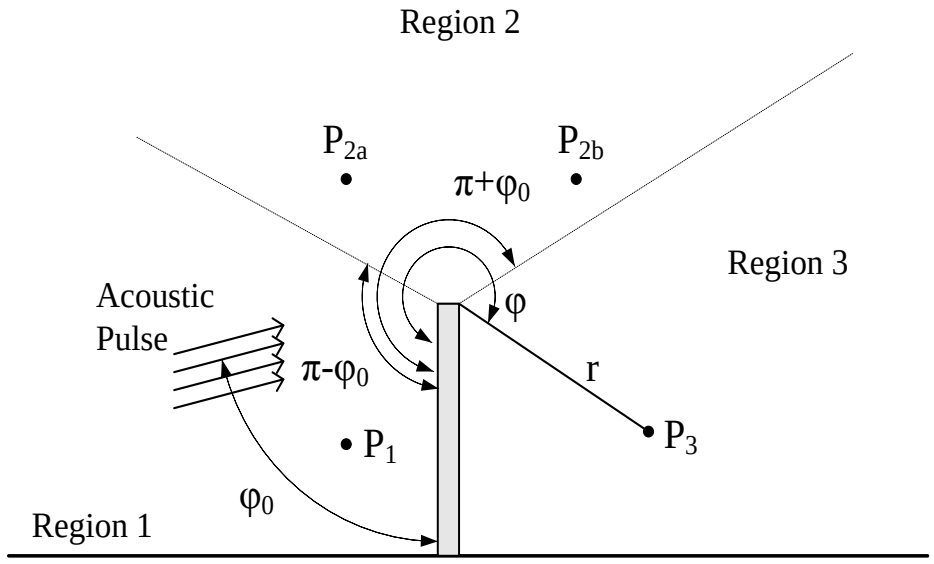

Figure D-1: Diffraction of a sound pulse by a rigid barrier. Test case geometry. Plane incident wave diffracted by a rigid obstacle.

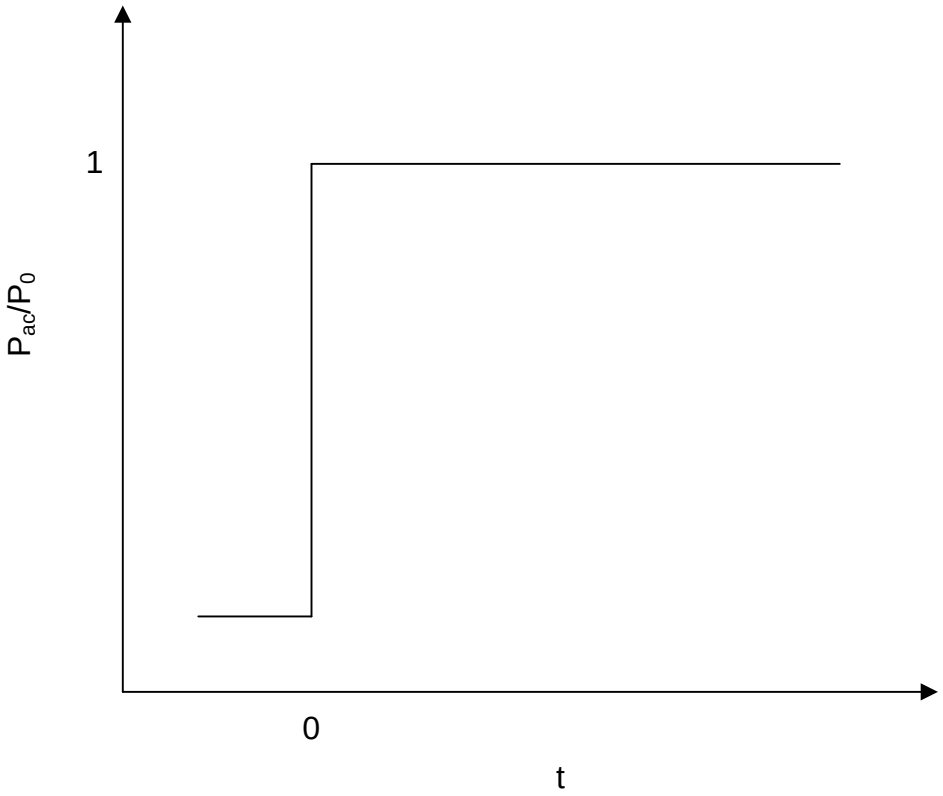

Figure D-2: Diffraction of a sound pulse by a rigid barrier. Plane incident wave at the inflow boundary of the computational domain.

In the case of a plane unit step function $P_{inc} = H\left(t + \frac{r}{c}\cos\left(\varphi - \varphi_0\right)\right)$ (see Figure D-2), where H is the Heaviside function, the linear analytical solution for the acoustic pressure at any point P (φ, r) has the following form. Until the arrival of the sound pulse to the barrier $\left(ct < r\right)$, the acoustic pressure is:

$$P_1(r,\phi,t) = \begin{cases} 0, & ct < -r\cos(\phi - \phi_0) \\ 1, & -r\cos(\phi - \phi_0) < ct < -r\cos(\phi + \phi_0) \\ 2, & -r\cos(\phi + \phi_0) < ct < r \end{cases}$$

$$P_2(r,\phi,t) = \begin{cases} 0, & ct < -r\cos(\phi - \phi_0) \\ 1, & -r\cos(\phi - \phi_0) < ct < -r \end{cases}$$

$$P_3(r,\phi,t) = 0$$

where the subscripts 1, 2, 3 indicate the region where the solution is valid.

After the arrival of the diffracted pulse $(ct > r)$ the sound pressure is given by:

$$P_1(r,\phi,t) = 2 - \frac{1}{\pi}\tan^{-1}\left(\sec\frac{\phi-\phi_0}{2}\sqrt{\frac{ct-r}{2r}}\right) - \frac{1}{\pi}\tan^{-1}\left(\sec\frac{\phi+\phi_0}{2}\sqrt{\frac{ct-r}{2r}}\right)$$

$$P_2(r,\phi,t) = 1 - \frac{1}{\pi}\tan^{-1}\left(\sec\frac{\phi-\phi_0}{2}\sqrt{\frac{ct-r}{2r}}\right) + \frac{1}{\pi}\tan^{-1}\left(\left|\sec\frac{\phi+\phi_0}{2}\right|\sqrt{\frac{ct-r}{2r}}\right)$$

$$P_3(r,\phi,t) = \frac{1}{\pi}\tan^{-1}\left(\left|\sec\frac{\phi-\phi_0}{2}\right|\sqrt{\frac{ct-r}{2r}}\right) + \frac{1}{\pi}\tan^{-1}\left(\left|\sec\frac{\phi+\phi_0}{2}\right|\sqrt{\frac{ct-r}{2r}}\right)$$

As $ct \to \infty$ the term $\frac{1}{\pi}\tan^{-1}\left(\sec\frac{\phi-\phi_0}{2}\sqrt{\frac{ct-r}{2r}}\right)$ goes to 1/2. The diffraction contribution in Region 1 becomes -1, while in Region 2 it becomes zero and 1 in Region 3. The total pressure field in all three regions approaches unity, as *ct* becomes infinite. The physical interpretation is that a long time after the diffraction the presence of the barrier is not felt. This analytical solution is of course a product of approximations but still a good way to evaluate the new method's results.